THE UNIVERSITY OF CALGARY

Stress States in Cartilage During Joint Loading and Indentation

by

Lara Lisa Malmqvist

A THESIS
SUBMITTED TO THE FACULTY OF GRADUATE STUDIES
IN PARTIAL FULFILLMENT OF THE REQUIREMENTS FOR THE
DEGREE OF MASTER OF SCIENCE
DEPARTMENT OF CIVIL ENGINEERING

CALGARY, ALBERTA
AUGUST, 1996

The University of Calgary

Faculty of Graduate Studies

The undersigned certified that they have read, and recommend to the Faculty of Graduate Studies for the acceptance, a thesis entitled, "Stress States in Cartilage During Joint Loading and Indentation" submitted by Lara Malmqvist in partial fulfillment of the requirements for the degree of Master of Science.

Dr. Cy Frank
Department of Surgery

Dr. John Matyas
Department of Anatomy

Dr. Janet Ronsky
Department of Mechanical Engineering

Dr. Nigel Shrive
Department of Civil Engineering

August 20, 1996
Date

ABSTRACT

Mechanical factors are thought to be implicated with joint disease, such as osteoarthritis, thus knowledge of the mechanical behaviour and properties of articular cartilage is essential for the prevention and treatment of joint diseases.

To test a hypothesis concerning the correlation of an unconfined, time-dependent indentation model, with a diarthrodial joint relaxation test model. Numerical finite element models revealed that indentation model pore pressure location within the joint model depended on the degree of congruity between the apposing surfaces in the joint.

An axisymmetric indentation model tested the hypothesis concerning the aspect ratio limit of indentation models. Results showed that $r/h \geq 1.60$ is necessary for physiologically relevant results.

This study produced mechanical data for correlation with metabolic response of cartilage to load, in order to develop a hypothesis determining which mechanical parameter(s) is of potential relevance.

TABLE OF CONTENTS

LIST OF TABLES

LIST OF FIGURES

1.0 Overview

1.1 Introduction

Many types of joints exist within the musculoskeletal system of mammals, in particular humans. The ankle, knee, hip, and knuckle of the fingers are examples of free-moving joints referred to as synovial or diarthrodial joints (Mow et al., 1992). Articular cartilage, a thin layer of hydrated soft tissue, covers the ends of the apposing bones in the synovial joints. The cartilage functions to transfer forces between the two apposing bones when the joint is loaded; to distribute the force within the joint; to allow nearly frictionless joint movement (Shrive, & Frank, 1994).

Articular cartilage has no blood, nerve, or lymph supply (Mankin et al., 1994).

Normally, articular cartilage provides a lifetime of competent function despite the rigorous mechanical loading to which it is subjected. Paul (1976) determined that the human knee joint is subjected to loads of nearly three times a person's body weight at a normal walking speed of 1.5 m/s, or a loading frequency between 0.5 and 1.0 Hertz. At the same walking speed, Paul determined that the human hip joint was exposed to loads as high as 7.6 times the person's body weight. Mow et al. (1992) estimated that a knee or hip joint in a normally active human may be subjected to one million cycles of loading, over the span of one year.

The health of articular cartilage is dependent on the loading and unloading of the tissue for the exchange of nutrients and waste. Atrophy of articular cartilage has been associated with the lack of use of joints (Shrive & Frank, 1994). Results (Mow et al., 1992) have shown that overloading of a knee due to an injury, such as a damaged ligament, may lead to degeneration and eventual failure of the articular cartilage. Conversely, mechanical destabilization of the joint, chronic failure, and fatigue problems may also lead to eventual failure of the joint, and osteoarthritis. (Mow et al., 1992).

Mechanical overloading of the joint occurs when a large external load is applied to the joint and transferred through a small contact area between the two articular surfaces. The external load includes active loading such as the forces resulting from heavy lifting, or impact loading, such as the forces arising from a collision.

Chronic failure of the articular cartilage results from interfacial and/or fatigue problems, potentially arising when the bearing surface of the joint is insufficiently lubricated (Shrive & Frank, 1992).

Fatigue failure of the articular cartilage may also may be caused by cyclical loading, when a joint is loaded with large active, or impact loads over extended periods of time (eg. running) (Shrive & Frank, 1992).

Mechanical overloading, chronic failure, and fatigue failure result in structural changes in the joint, affecting its ability to transfer loads without mechanical wear on the articular cartilage (Shrive & Frank, 1992).

1.2 Osteoarthritis

Osteoarthritis is a common crippling disease characterized by pain and degeneration of cartilage in the joint. Cartilage loss is believed to result from excessive 'wear and tear' on the cartilage coupled with the inability of the cartilage to repair itself.

Although the actual cause(s) of osteoarthritis is unknown, it is believed that a number of factors may play a role in either the initiation or the progression of the disease (Mankin et al. , 1994):

1. Aging
2. Alterations in the matrix structure of the articular cartilage tissue
3. Alterations in the cellular activity of tissue
4. Alterations in mediators
5. Trauma
6. Immune responses.

In "Western" society, arthritis has become one of the most prevalent diseases common to the population 65 years and older. An estimated 40 million Americans are currently known to suffer from this debilitating disease. This number is projected to rise to 59 million, or 18% of the American population, by the year 2020 (Dunkin & Morrow, 1994).

The cost to the United States economy in 1988 for the treatment of this disease was estimated at $54.6 billion. This total included the direct costs of treatment, and the costs resulting from a loss of productivity.

1.3 Project Rationale

Experimental studies of osteoarthritis have revealed that articular cartilage has a potential for repair. With proper treatment, it is believed that the progression of the disease may be delayed, or prevented. Currently, patients suffering from osteoarthritic joints frequently undergo prosthetic replacement of the afflicted joint. Unfortunately, problems are often encountered in the fixation of the prosthesis to bone, and in the wear resistance of the implant joint components. Thus, an alternative to the current method of treatment of the disease seems favourable. However, in order to develop new treatment regimes, knowledge of the mechanical function and properties of articular cartilage is essential.

Numerical models have been developed by researchers to simulate confined and unconfined indentation tests of cartilage performed in the laboratory in attempts to determine the mechanical properties of the cartilage. However, a disparity exists between the results obtained through laboratory testing and the results calculated in numerical models.

In this study, the finite element method will be used to model an unconfined indentation of an articular cartilage plug. The model will then be altered such that the height of the cartilage plug is varied, keeping the indentor and cartilage plug radius constant. Various parameters, including pore pressure, matrix stress, and fluid flow conditions will be estimated at different locations within the tissue under the indentor.

The next step in this analysis will be to develop a model of a generic diarthrodial joint consisting of two incongruent apposing cartilage surfaces undergoing a stress relaxation test. The contact zone between the two surfaces will be noted in order to determine the magnitudes of parameters, similar to those measured in the indentor model, at similar locations in this full joint model. The geometry of the upper joint surface will then be varied, keeping the lower joint geometry constant, and the parameters will be estimated.

This study will compare the results of indentation models with generic diarthrodial joint models in order to determine the locations and conditions necessary for the indentation model to simulate the stresses, pore pressures, fluid flow conditions present in a diarthrodial joint.

The experimental limits for indentation tests to produce stress states similar to those in a diarthrodial joint will thus be delineated. Indentation tests intended to examine biological effects of loading as in a diarthrodial joint will then be possible.

2.0 Articular Cartilage

2.1 Introduction

Articular cartilage is a soft connective tissue covering the surface of bones in synovial joints. Synovial, or diarthrodial joints, are freely moving joints such as in the ankle, knee, hip, and knuckles of the fingers as opposed to the joints of the spine which are not freely moving, or diarthrodial joints (Mow et al., 1992).

Diarthrodial joints within the body are structurally similar in several ways. All diarthrodial joints limited by a joint capsule, see Figure 1. The inner lining of the capsule is called the synovium. This lining is a metabolically active tissue which secretes synovial fluid, which in turn supplies the nutrients to the cartilage within the joint. The ends of the joint bones are covered with a thin layer of tissue called articular cartilage. The space between the bones, the articular cartilage (a hydrated soft tissue) along with the synovium, form the joint cavity, in which the synovial fluid is found (Mow et al., 1992).

Articular cartilage, normally provides a lifetime of use with little wear and tear under typical activity levels. Articular cartilage acts with the synovial fluid to provide a nearly frictionless articulating surface (Swanson, 1979). The coefficient of friction of articular cartilage is approximately = 0.0025, (Shrive & Frank, 1994) roughly 1/8 the coefficient of friction of a person gliding on ice (Mankin et al., 1994).

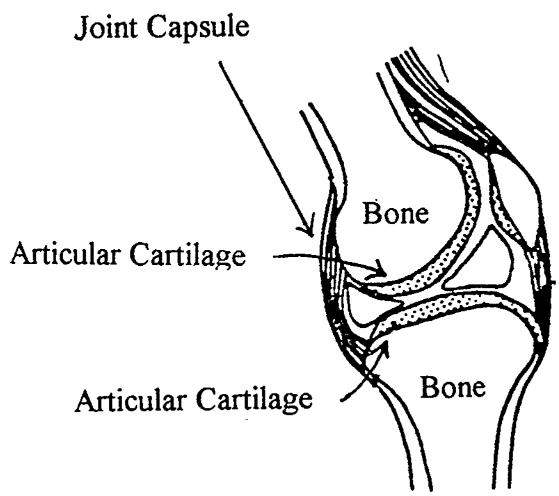

Figure 1
Diarthrodial Joint
(Mow et al., 1992)

Articular cartilage is unique from other tissues within the body in that it is avascular, aneural, and alymphatic (Shrive & Frank, 1994; Mankin et al., 1994). The cartilage is uniquely designed to maintain a significant stiffness and resilience despite of a high water content; the combination of type II collagen fibres and proteoglycans and the way they interact with water are primarily responsible for the functional properties of cartilage (Mankin et al., 1994).

Articular cartilage forms self-lubricating, low-friction gliding, and load-distributing surfaces of the synovial joints (Mankin et al., 1994).

2.2 Articular Cartilage : Composition

Articular cartilage is a tissue composed of a composite matrix (≈95%) which is saturated with water, and randomly dispersed cells (≈5%) (Shrive & Frank, 1994).

2.2.1 Chondrocytes

The cells of the articular cartilage, or chondrocytes, vary in shape and concentration, with depth. These cells are responsible for the maintenance and function of the cartilage matrix and produce type II collagen and proteoglycan (Shrive & Frank, 1994).

2.2.2 Extracellular Matrix

The matrix of articular cartilage consists of a network of structural macromolecules including collagen fibrils interspersed with proteoglycans, glycoproteins, and a small number of lipid materials; and tissue fluid (Meachim & Stockwell, 1973). The tissue fluid, consisting of water and electrolytes, occupies 65-80% of the matrix's composition (Muir, 1979; Shrive & Frank, 1994).

2.2.2.1 Collagen

The solid component of normal adult articular cartilage is 60-70% of collagen by dry weight (Maroudas, 1973; Meachim et al., 1973; Muir, 1973).

Investigators have found the collagen fibrils in tendons, another self connective tissue, to have low torsional and flexural stiffness, and buckle under compressive loading (Hukins, 1982). Under tensile loading, however, the fibrils were found to be stiff and strong (Hooley & Cohen, 1979). Thus, collagen fibrils are thought to contribute to the tensile stiffness and strength of articular cartilage during joint motion.

Collagen fibrils reinforce the articular cartilage in much the same way that steel wire is used to reinforce concrete. Concrete is a composite material strong in compression and weak in tension. In reinforced concrete, the reinforcing steel, a material strong in tension, is embedded within the concrete at locations where tensile resistance is required to resist tensile stresses (Pillai & Kirk, 1988), see Figure 2. Collagen fibrils play a role in articular cartilage similar to that of steel in reinforced concrete: the fibrils are oriented in a manner which loads them in tension (Hukins, 1984).

Steel reinforcement in concrete is designed to be of a length adequate enough to introduce, or develop, a given stress into the bar through the bond between the concrete

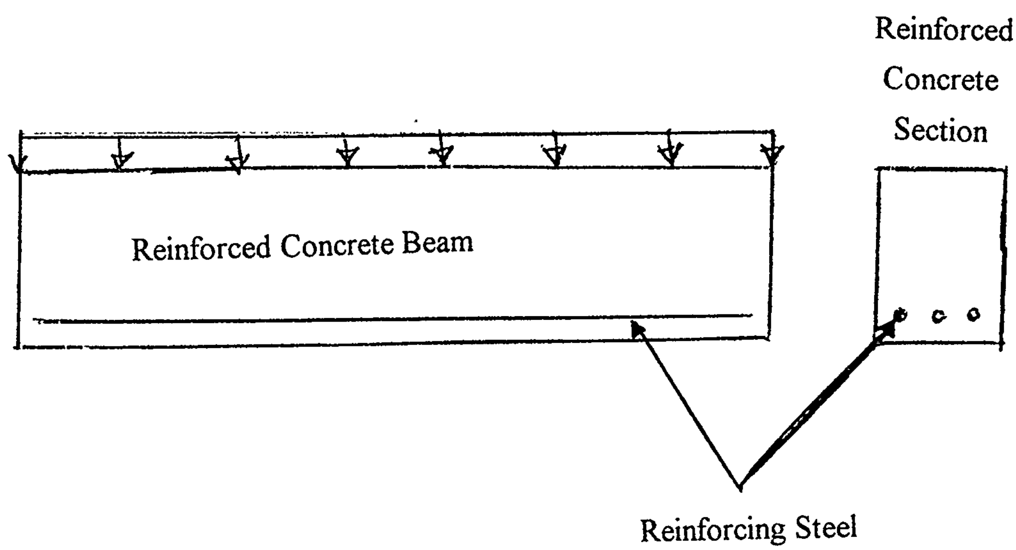

Figure 2
Reinforced Concrete Section

and bar, or conversely, the length is sufficient enough to take the maximum stress out of the bar (Pillai & Kirk, 1988). This length is referred to as 'development length' in concrete design.

Likewise, in order for collagen fibrils to provide effective tensile strength to the tissue, their lengths must also be greater than a 'critical length'.

When a collagen fibre within the articular cartilage is loaded in tension along it's length, matrix viscous forces resist the pull-out force applied to the collagen fibril. These resistant forces are proportional to the surface area of the fibril. Thus, an increase in the length of the fibril concurrently increases the magnitude of the resistant viscous forces. When the length of the fibril exceeds a 'critical length', and the matrix is sufficiently viscous, the resistant matrix viscous forces balance the applied tensile load, and the articular cartilage is in equilibrium (Hukins & Aspden, 1989).

At least 18+ types of collagen which differ in structure and function (Mow et al., 1992), have been identified by researchers (Mayne, 1989). The major collagen type found in articular cartilage is Type II collagen (Mankin et al., 1994; Mayne, 1989; Shrive & Frank, 1994). Type II collagen is similar to Type I collagen found in bones, in that both types contain a stiff helical structure. However, the triple helix of Type II collagen contains 3 identical alpha chains, unlike the 2 identical and 1 different alpha chains in Type I collagen. Each of the alpha chains in articular cartilage has a high hydroxylysine and content and abundant covalently attached to carbohydrates. These contribute to

Type II collagen's adherence to proteoglycans within the cartilage tissue (Shrive & Frank, 1994).

Collagen types V, VI, X are also present in articular cartilage in varying concentrations. These minor collagens are thought to play an important role in the structure of the cartilage (Eyre et al., 1987; Eyre et al., 1991; Mankin et al., 1994).

Type II collagen in articular cartilage has a greater number of intermolecular and intramolecular covalent cross-linkages between the alpha chains and collagen molecules than Type II collagen found in the other parts of the body. These cross-links are thought to maintain the cohesiveness of the collagen network; to provide high tensile strength and stiffness for the tissue; and to provide greater availability for proteoglycan linkage (Mow et al., 1992; Shrive & Frank, 1994).

2.2.2.2 Proteoglycans

Normal adult articular cartilage contains an average of 5-15% of proteoglycans by dry weight, (Maroudas, 1973; Meachim et al., 1973; Muir, 1973; Shrive & Frank, 1994) which makes these molecules the second largest organic material component in articular cartilage. Proteoglycans provide the following properties to the cartilage: (Mow et al., 1992)

1. compressive stiffness,
2. Donnan osmotic pressure (in combination with water)
3. control of pore size and hydraulic permeability,

4. regulation of tissue hydration.

Proteoglycans are complex macromolecules composed of a linear protein core to which many glycosaminoglycans, consisting of chains of repeating disaccharides, are covalently bound (Mow et al., 1980; Shrive & Frank, 1994), see Figure 3(a). Aggrecan is the largest, most osmotically active, and most abundant proteoglycan, though there are others. These disaccharides include chondroitin sulphate and keratin sulphate. These molecules provide physicochemical properties to the cartilage. (Mow et al., 1992) For instance, the chondroitin sulphate chains provide frictional resistance against interstitial fluid flow (Comper et al., 1990).

The chondroitin and keratin sulphate chains consist of repeating disaccharide units which become ionized. Due to the close proximity of the disaccharide units, 1.0 to 1.5 nm (Mow et al., 1992), a "bottle brush" effect is created as the groups exert repulsive forces on each other, see Figure 3(b). These repulsive forces are thought to be the primary cause of cartilage swelling pressure (Maroudas, 1973; Mow et al., 1992).

The anions on the disaccharide units attract cations into the cartilage resulting in a build-up of ions within the tissue. This build up results in an increase in a Donnan osmotic pressure within the tissue, and an attraction of water into the tissue through osmosis (Hukins et al., 1984). This Donnan osmotic pressure is thought to range from 0.1 to 0.2 MPa in articular cartilage, (Maroudas, 1973) and is thought to provide up to 50% of the articular cartilage's compressive stiffness (Mow et al., 1990; Lai et al., 1981).

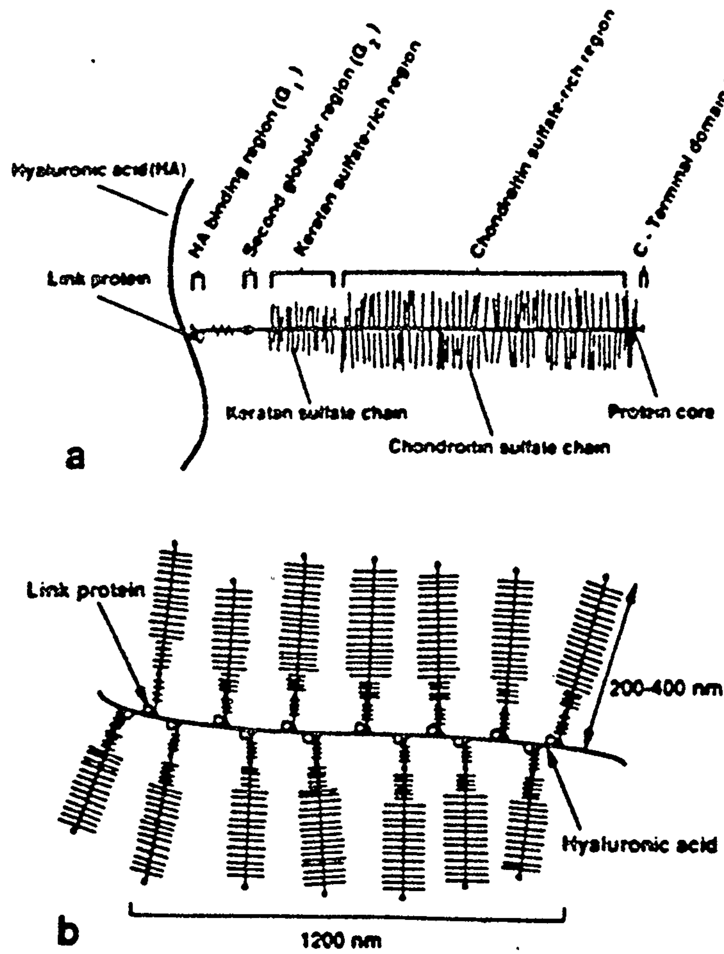

Figure 3
Organization of (a) the Aggrecan, (b) an Aggrecan-Hyaluronan Aggregate (Mow et al., 1992)

2.2.2.3 Collagen - Proteoglycan Interaction

Within the extracellular matrix of the cartilage, the collagen network and proteoglycans interact to form a fibre-reinforced composite tissue, see Figure 4. The collagen fibres provide tensile stiffness and strength to the tissue, whereas the proteoglycans, through Donnan osmotic pressure, are thought to provide compressive stiffness. The water trapped in the matrix by the proteoglycans does not contributes to the compressive stiffness of the tissue due to it's incompressible nature unless it flows.

Interaction between collagen fibrils and proteoglycans within cartilage develop through either electrostatic forces or mechanical loading. These interactions have been found to occur between the negative charges on the proteoglycans and the positive charges on the collagen fibrils (Muir, 1983). Similarly, physical interactions have been found which result from friction occurring between the collagen fibres and proteoglycans (Schmidt et al., 1990).

2.2.2.4 Other Proteins

Other proteins found in articular cartilage also play important roles within the tissue. For instance, chondronectin, an 'adhesive' protein in articular cartilage is thought to be responsible for establishing a relationship between the collagen fibres and the chondrocytes. Two other proteins believed to play a role in articular cartilage are fibronectin and anchorin

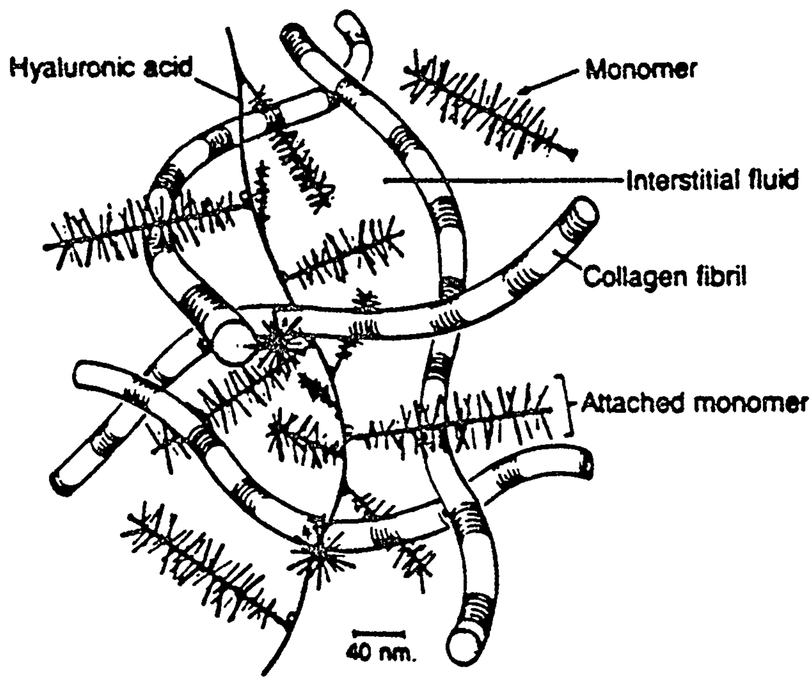

Figure 4
The Collagen Network Interacting with the Proteoglycan Network in the Extracellular Matrix Forming a Fibre-Reinforced Composite (Mow et al., 1989)

2.2.2.5 Tissue Fluid

Tissue fluid, the major constituent of articular cartilage (60 - 85% by wet weight), is composed primarily of water (Mow et al., 1992). The fluid is present in the tissue in the form of a viscous gel interspersed with the structural macromolecules. The majority of tissue fluid (≈95%) is free to move inside and outside of the cartilage. Within the cartilage, the only restraint acting on the fluid arises from the presence of proteoglycans. The amount of water present in the cartilage is dependent on the following factors:

1. swelling pressure,
2. organization and integrity of the collagen network,
3. material properties of the collagen - proteoglycan solid matrix (Mow et al., 1992).

2.3 Articular Cartilage: Morphology/Histology

The structure of articular cartilage varies with depth from the surface of the joint to the subchondral bone. Researchers have used light electron microscopy to map the spatial distribution and orientation of structural components within the tissue.

The surface of the cartilage consist of undulations and irregularities. Rather than being smooth, the surface is made up of ridges and valleys which are 2-6 μm deep (Mankin et al., 1994; Shrive & Frank, 1994).

The surface of the cartilage is composed of a thin layer termed the lamina splendens, a plane of interwoven collagen fibres, which functions to resist the lateral contact tension generated by joint surface, and the tension resulting from tissue matrix swelling. The depth of the tissue is normally divided into four distinct histologic zones (Mankin et al., 1994; Shrive & Frank, 1994; Woo et al., 1976):

a) Superficial tangential (or gliding) zone (STZ)

b) Tangential (or middle) zone

c) Deep (or radial) zone

d) Calcified zone

2.3.1 Superficial Tangential Zone

The most superficial zone in the tissue is the Superficial Tangential zone (STZ), see Figure 5. This zone occupies approximately 10-20% of the total tissue thickness. The STZ contains the highest collagen fibril concentration, highest water concentration (≈80%) (Mow et al., 1992), and lowest proteoglycan concentration of the four zones within the tissue (Mow et al., 1980; Mow et al., 1992; Shrive & Frank, 1994).

The STZ is further divided into 2 layers:

i) surface layer
ii) deep layer (Shrive & Frank, 1994).

The surface layer of the STZ is composed of collagen fibril bundle networks randomly-distributed below the surface of the cartilage (Shrive & Frank, 1994).

The collagen fibrils within the deep layer of the STZ, however, are oriented parallel to the surface of the tissue (Aspden & Hukins, 1981 a,b; Hukins, 1984; Shrive & Frank, 1994), see Figure 6.

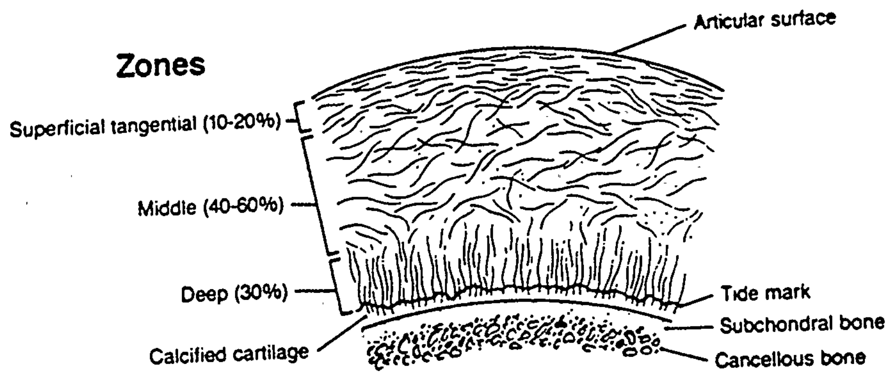

Figure 5
The Organization of the Dense Collagen Network throughout the Three Major Zones of Cartilage
(Mow et al., 1992)

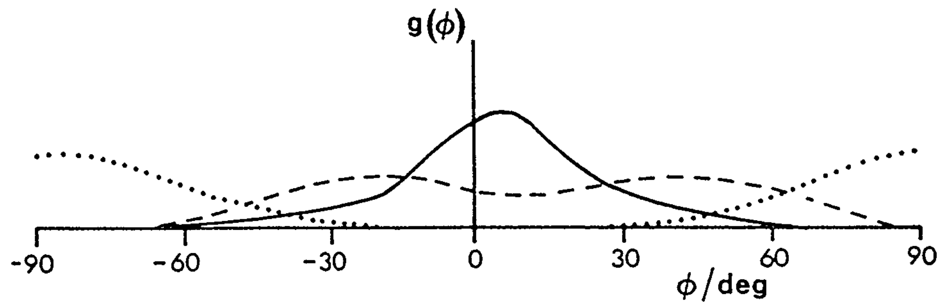

Figure 6
Orientation Distribution function, g(ϕ), for the Collagen Fibrils in the Surface (_), Intermediate (--), and Deep (...) zones of Articular Cartilage; the Zero Value of ϕ is Defined by the Normal to the Surface
(Hukins & Aspden, 1989)

The deep layer also consists of elongated chondrocytes which lie with their long-axis parallel to the articular surface (Shrive & Frank, 1994), see Figure 7.

2.3.2 Transitional Zone

The Transitional zone (40-60% of total thickness) (Mow et al., 1992), is subjacent to the STZ. The collagen content of this zone is approximately 15% lower than the concentration in the STZ. Similarly, the water content of this zone is lower than in the STZ, whereas the proteoglycan concentration is approximately 15% higher than in the STZ (Mow et al., 1992).

The collagen fibrils within the Transitional zone are randomly oriented and homogeneously distributed (Mow et al., 1980), see Figure 6.

Unlike the chondrocytes found in the STZ, the chondrocytes in the Transitional zone, see Figure 7, are spheroidal and contain abundant endoplasmic reticulum (an extensive network of membrane-enclosed tubules in the cytoplasm of cells which synthesize proteins), golgi bodies (which add sugars including GAGs, sort, and secrete proteins to the matrix), and mitochondria (which generate energy) (Anderson & Anderson, 1990). The presence of endoplasmic reticulum, gogli bodies, and mitochondria within the Transitional zone suggests that the cells in this zone play a more active role in the matrix synthesis and degradation, thus metabolism, than the cells in the STZ (Shrive & Frank, 1994).

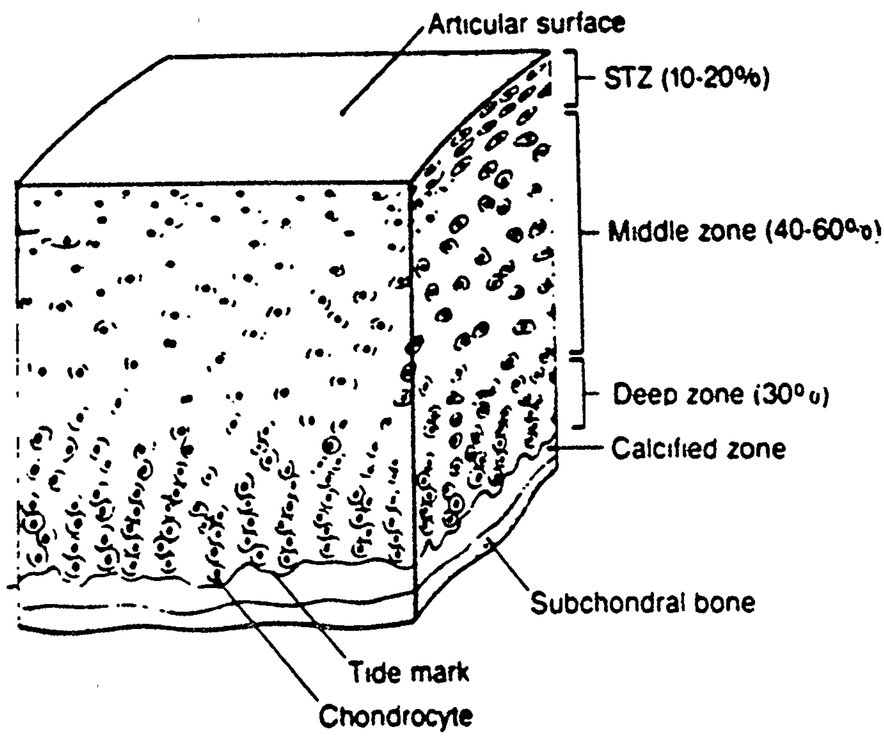

Figure 7
The arrangement of Chondrocytes throughout the Surface, Middle, and Deep Zones of Cartilage
(Mow et al., 1992)

2.3.3 Deep Zone

The third zone encountered in the articular cartilage's depth from the surface is the Deep zone (~ 30% of total thickness, Mow et al., 1992). The percentage of collagen by weight remains constant throughout the Transitional and Deep zones of the articular cartilage. The water content in the Deep zone is approximately 65% and the proteoglycan content is highest in this zone (Mow et al., 1980; 1992).

The randomly-oriented collagen fibrils of the Transitional zone join together into larger collagen fibrils, oriented perpendicular to the articular surface, when the Deep zone is reached in the tissue (Mow et al., 1980), see Figure 6.

The chondrocytes in the Deep zone are round and are arranged in columns which lie perpendicular to the articular surface, see Figure 7. These cells contain an even greater number of endoplasmic reticula, golgi bodies, cytoskeletal intracytoplasmic filaments (which support the cell structurally), and glycogen granules (which store sugar) (Anderson & Anderson, 1990). Thus, it is thought that much of the protein and proteoclycan synthesis within the articular cartilage occurs in the Deep zone (Shrive & Frank, 1994).

2.3.4 Calcified Cartilage Zone

The Calcified zone lies between the Deep zone and the subchondral bone. A 'tidemark' exists between the non-calcified Deep zone and the Calcified zone. The 'tidemark' is generally believed to be associated with a 'twist' in the collagen bundles of the Deep zone as they descend into the Calcified zone and become embedded into the subchondral bone. The 'tidemark' is approximately 2-5μm thick (Mankin et al., 1994).

The larger collagen bundles, of the Deep zone, are embedded in mineral to form an interlocking mesh which in turn undergoes endochondral ossification to anchor the articular cartilage to the subchrondral bone (Mow et al., 1980).

2.4 Articular Cartilage Properties

2.4.1 Tensile Properties

The tensile properties of articular cartilage vary with depth within the tissue (Shrive & Frank, 1992). These property differences are attributed to the zonal morphology of the collagen network and the orientation of the collagen fibrils within the zones.

Additionally, the tensile strength of articular cartilage varies depending on whether the tissue is loaded parallel or perpendicular to the orientation of the collagen fibrils. The tensile strength of the tissue has been found to be greater parallel to the 'split-line'- 'Hultkrantz Lines: (Mow et al., 1992). A 'split-line' pattern is observed in articular cartilage when the surface of the cartilage is penetrated with a needle dipped in Indian ink. The ink ends up lying in a line whose length is parallel to the primary orientation of the collagen fibres.

Stress-strain curves of cartilage in tension indicate that there is a transition from non-linear to linear stress-strain behaviour of the tissue over the range of strain, see Figure 8. The non-linear 'toe' region of the curve for tissue tested parallel to the split-line is thought to result from a realignment of collagen fibrils. As the strain increases, more and more collagen fibrils are required to resist the load, and the fibrils' crimp is straightened out as the fibrils support the increasing load (Mow et al., 1992; Shrive & Frank, 1994).

At higher strains, the stress-strain curve is linear. This linear region is thought to represent the actual behaviour of the collagen fibril network once the fibrils have been straightened (Roth & Mow, 1980; Woo et al., 1987).

For a given orientation, the tensile modulus of articular cartilage is greatest at the surface of the tissue, and decreases with depth from the surface. This characteristic is thought to be related to the orientation of the collagen fibres. The majority of the fibrils at the surface of the tissue are oriented parallel to the articular surface, whereas the fibrils in deeper layers tend to be more vertically randomly-orientation. Thus, the surface fibrils are thought to be more suitably oriented to resist tensile stress applied along their length (Shrive & Frank, 1994).

2.4.2 Compressive Properties

Compressive properties of articular cartilage, similar to the tensile properties, vary with depth within the articular cartilage (Shrive & Frank, 1992). However, compressive property variations are associated with concomitant in parallel with the zonal differences

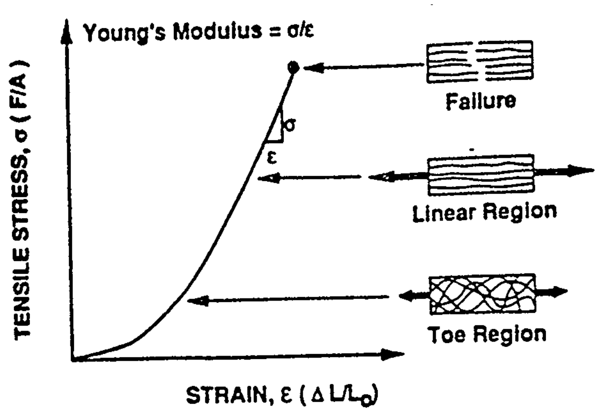

Figure 8
The Fibre-Recruitment Model for the Non-Linear Tensile Behaviour of Cartilage (Mow et al., 1992)

in concentration (biochemistry) of the proteoglycans.

Accompanying an increase in proteoglycan concentration, cartilage compressive stiffness increases with increasing depth from the surface The negative electrostatic charge on the proteoglycans increases as the concentration of the proteoglycans increases, resulting in an increase in the net negative charge in the tissue. The overall effect of increasing proteoglycans is that the tissue is able to resist larger externally-applied loads (Shrive & Frank, 1994).

2.4.3 Shear Properties

The shear properties of articular cartilage have not yet been measured as a function of depth, though the interaction between collagen fibrils and proteoglycans are thought to be primarily responsible for resisting the shear in articular cartilage. When cartilage is subjected to shear deformation, it is thought that the fluid remains within the tissue possibly loading the collagen fibrils in tension. The overall resistance to shear deformation may increase due to movement of the proteoglycans within the tissue (Shrive & Frank, 1994).

2.4.4 Viscoelastic Properties

Articular cartilage is primarily loaded in compression *in vivo*. Flow-dependent viscoelastic behaviour of cartilage loaded in compression is illustrated by the creep and stress-relaxation behaviour of the tissue. Frictional drag, resulting from interstitial fluid flow, is the primary mechanism which leads to the viscoelastic behaviour of cartilage (Mow, Holmes, & Lai, 1984).

Creep is defined as the change in strain over time under constant stress, see Figure 9. The total strain is composed of initial strain and the creep strain. Removal of the applied stress results in the strain diminishing over time, which is referred to as the 'recoverable' strain. At time infinity, t_∞ , any residual strain is called 'irrecoverable' strain (Shrive & Frank, 1994). The rate of creep is dependent on the hydraulic permeability of the tissue.

Stress-relaxation, on the other hand, occurs under constant strain, see Figure 10. Upon the application of a strain, an initial stress is induced which diminishes over time. Stress-relaxation is a measure of the reduction in stress diminishes. Removal of the applied strain results in a stress reversal that decays with time.

Due to its viscoelasticity, the properties of articular cartilage are time-dependent, by definition, (ie) loading rate dependent (Shrive & Frank, 1994).

2.5 Mechanics of Articular Cartilage

2.5.1 Joint Loading

It is estimated that the knee or hip joint of the human body may experience as many as one million cycles of loading per year. Daily activities such as walking and stair climbing may

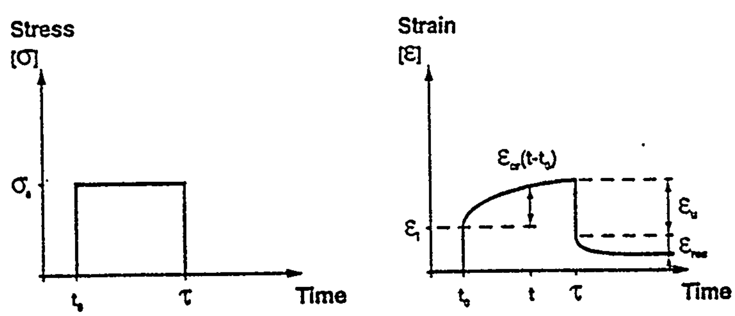

Figure 9
Schematic of stress application (left) and removal in time and resulting strains for a viscoelastic material (right)
(Shrive & Frank, 1994)

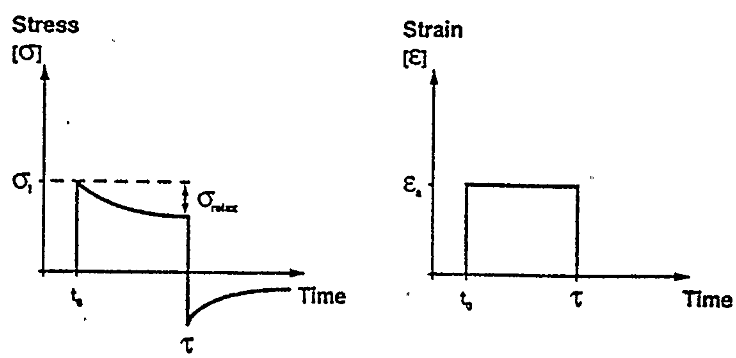

Figure 10
Schematic of the phenomenon of stress-relaxation (left), and for an applied constant strain (right)
(Shrive et al., 1994)

exert loads on the human knee or hip joint of up to 10 times the body's weight. Standing in one position, or if a joint remains in a static position for an extended period of time may result in loads on the joints of several times the body's weight. Thus, human joints have to be capable of withstanding very high loads and stresses at normal operating speeds. This amount/frequency of loading requires an efficient lubrication system within the joint to minimize friction and wear of cartilage in the joint (Mow et al., 1992).

The type and magnitude of the applied load, joint motion, and joint anatomy play a role in determining the type and magnitude of the contact stresses of a loaded joint and the manner in which these stresses will be distributed through the joint.

2.5.1.1 Compressive Loading

As a joint is loaded, the two apposing layers of articular cartilage contact each other. Load is transferred from one cartilage layer to the other either through direct contact and/or through a thin film of pressurized fluid which may exist between the two layers (Shrive & Frank, 1994).

Compression loads force proteoglycans beneath the contact zone to move closer together over time, resulting in an increase in the net negative electrostatic charge. This consolidation phenomenon reduces the permeability of the surface layer, restricting fluid flow under the contact zone to lateral flow primarily. At the edges of the contact zone, however, the fluid is permitted to flow up and out of the cartilage layer (Shrive & Frank, 1994).

The upward movement of fluid at the edge of the contact zone creates a frictional drag in the matrix, which results in vertical tension in the matrix. This tension is resisted by the collagen fibres oriented vertically, and at angles in the Deep and Tangential zones of the articular cartilage (Shrive & Frank, 1994). The collagen fibres in the Deep zone are oriented such that upward movement of fluid is resisted by the fibres. The random orientation of fibres in the Transition zone provides a smooth transition between the collagen fibrils of the STZ, which are oriented parallel to the surface, and the collagen fibrils of the Deep zone, which are oriented perpendicular to the articular surface (Hukins et al., 1984).

Compressive loading of articular cartilage is initially resisted by the tissue fluid. The fluid becomes pressurized and transmits the load through the tissue down to the subchondral bone. Over time, the matrix fluid flows laterally away from the contact zone; creep occurs in the cartilage matrix; the contact area increases and then decreases in size. This contact zone size fluctuation results from the matrix fluid flowing laterally away from the contact zone and the matrix becoming more stressed (Shrive & Frank, 1994).

Lateral fluid flow away from the contact zone creates a drag on the tissue, by pulling the matrix along with fluid, thus creating a lateral tension in the matrix. This tension is resisted by the collagen fibres of the STZ, which are oriented parallel to the articular surface. A bulge appears on the surface of the cartilage just outside of the contact area, see Figure 11. This results from the straightening of collagen fibres due to the contact area load; and from the fluid moving up and out of the cartilage into this volume created

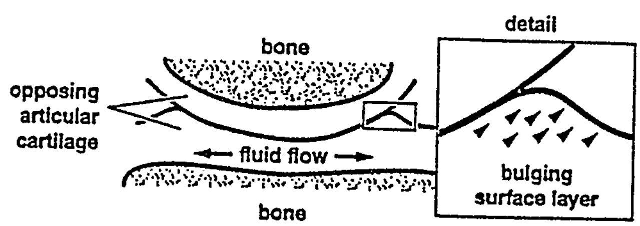

Figure 11
Schematic diagram of fluid flow in the superficial layer of articular cartilage under a compressive load
(Shrive & Frank, 1994)

by the bulge, from a pressurized area to an unpressurized area. This movement of fluid increases the surface area of the cartilage causing tension parallel to the surface of the cartilage. This tension is resisted by the collagen fibres of the cartilage oriented parallel to the tissue surface (Shrive & Frank, 1994).

2.5.1.2 Shear Loading

Frictional shear stress resulting from the motion of one bone relative to another in a joint is usually ignored by researchers, because of the small coefficient of friction. However, if considered, a joint loaded in shear initially compresses the matrix which induces a tensile stress in the STZ. This load is transmitted through the joint as a tensile load which is resisted by the randomly-distributed collagen fibres in the Transitional zone, and by the perpendicularly-oriented fibrils in the Deep zone.

2.5.3 Joint Failure

The health of articular cartilage is dependent on fluid exchange which is achieved through cyclic loading to exchange nutrients and metabolic waste. Atrophy has been associated with non-use of a joint which results in insufficient nourishment of the articulating surfaces (Greenwald & O'Connor, 1971).

Failure of articular cartilage may result from acute and/or chronic loading. Acute failure occurs when local stresses on the cartilage exceed the ultimate strength of the matrix in the particular stress state. This usually occurs when high external forces are exerted on articular cartilage and transferred through a relatively small contact area between the two articular surfaces. This external force could be either an active or impact force. Active forces could result from heavy lifting, whereas, impaction forces include forces resulting from collisions (eg. a car accident) (Mow et al., 1992; Shrive & Frank, 1994).

Chronic failure occurs as a result of interfacial problems and/or fatigue phenomena (Shrive & Frank, 1992). Interfacial problems occur when the bearing surface of the joint is insufficiently lubricated. This can result in the particles from the cartilage of the two bearing surfaces adhering to one another and tearing away; or softer tissues from one surface being scraped and damaged by the harder apposing surface (Mow et al., 1992; Shrive & Frank, 1994). Fatigue problems occur in articular cartilage when the matrix is damaged by cyclic loading. Damage can occur when high active or impact forces are exerted on the joint over extended lengths of time, (eg. running). Structural changes in the properties of normal cartilage may arise affecting its ability to transfer loads without mechanical wear on the articular cartilage (Mow et al., 1992; Shrive & Frank, 1994).

2.5.3 Osteoarthritis

Chondrocytes, as mentioned, are primarily responsible for synthesis and degradation, the homeostasis of the cartilage matrix. Researchers have found that the metabolic activity of the chondrocytes in articular cartilage is affected by changes in the mechanical environment of the chondrocytes (Mow et al., 1992). It is thought that parameters such as load, stress, strain, load history, strain energy, and density play a role in controlling the maintenance of the articular cartilage, and that some mechanical events may result in alterations in chondrocyte activity, which could lead to degradation of the tissue. Destabilization of the knee by cutting ligaments ultimately leads to cartilage degeneration and osteoarthritis (Mow et al., 1992).

At the onset of osteoarthritis, degradation of type II collagen appears near the surface of articular cartilage (Dodge & Poole, 1989). This degradation is thought to lead to changes in aggrecan related to stromelysin and perhaps Type III collagenase. The proteoglycan molecules are larger (less mature) in the earlier stages of osteoarthritis than those in healthy tissue (Adams, 1994)

In endstage osteoarthritis, damage extends down through the cartilage matrix until the fibrillation reaches the calcified cartilage. The proteoglycan molecules found in tissue at a more advanced stage of osteoarthritis appear larger than at the onset of the disease. This size discrepancy is thought to result from the tissue's attempt to repair itself through the replacement of newly synthesized, larger proteoglycan molecules (Adams, 1994). The weakened collagen network is associated with a reduction in the stiffness and strength of the tissue. The damaged tissue swells and interferes with the tissue's ability to sustain loading. Thus, cartilage material properties, and cartilage function within diarthrodial joint can be profoundly affected by the degradative processes of osteoarthritis (Mow et al., 1992).

2.6 Models of Cartilage Mechanical Behaviour

Numerical models have been developed and used by researchers to complement the *in vivo* and *in vitro* biomechanical testing in the laboratories. These models are useful for estimating material parameters, such as matrix stresses and strains, pore pressures, and fluid flow, of the articular cartilage under varying model geometries, and loading rates, for which are impractical or impossible to measure directly. The development of a numerical model to simulates the behaviour of a joint has great potential to refine biological experiments and to minimize the number of animals needed for laboratory testing.

2.6.1 Single - Phase Models of Articular Cartilage

2.6.1.1 Single - Phase - Elastic Models

The first numerical models developed were based on single-phase elastic material properties. These models considered the elastic nature of the articular cartilage matrix, but neglected the fluid effects of the tissue.

Indentation testing was a common mechanical loading technique used by researchers to determine the deformational characteristics of the tissue. This type of testing has been the primary choice for cartilage loading because cartilage acts 1° in compression.

Hirsch (1944), was among one of the first researchers to develop a numerical model of cartilage validating his starting assumptions with indentation tests. He applied the Hertz contact stress theory (which deals with the contact between two elastic bodies of infinite depth) to the observed behaviour of the human patellae articular cartilage.

Later, Zarek and Edwards (1963) modelled cartilage using the elasticity theory to analyze the structure-function relationship of collagen in compression. The Hertz contact stress theory was used to determine the magnitude of which stresses which result from indenting a rigid sphere into an elastic half-space, or a spherically concave body. Once the Principal stresses were determined, stress trajectories were plotted and compared to the known collagen arrangement in cartilage. This analysis/model showed poor correlation between collagen orientation and tensile stress in the Middle and Deep zones, whereas the Surface zone showed greater agreement between orientation and tensile stress of collagen.

Waters (1965) examined the indentation of thin sheets of vulcanized natural rubber using a rigid plane-ended cylindrical indentor. The author found that for a range of rubber thicknesses (1.5 to 18.5 mm) and indentor diameters (0.793 to 12.7 mm), in order to account for a finite depth, the classical Hertzian solution for a semi-infinite elastic layer should be multiplied by a dimensionless scaling factor.

$$E = \frac{P\,(1-\nu^2)}{2w_\circ\, a}\,\varphi\,(h/a) \qquad \text{Eq. 2.1}$$

where:

E = Young's modulus

P = load

ν = Poisson's ratio

$w_\circ$ = depth of penetration into the cartilage

a = radius of plane-ended cylindrical indentor

φ = scaling factor determined experimentally

It turns out that φ is sensitive to the type of interface which exists between the rubber and underlying glass during the indentation testing. Non-lubricated interfaces generally produced φ values of lower magnitude than the φ values determined for lubricated interfaces, for a given aspect ratio (ratio of rubber sheet thickness to width).

A possible drawback to this model is that the author did not account for possible friction that exists between the rigid indentor and rubber sheet. Such an omission of friction in the model may have had an effect on the results, particularly in tests involving larger indentors.

Sokoloff (1966) modelled cartilage as an incompressible elastic medium in order to determine the 'instantaneous Young's modulus'. The author assumed that the mechanical response of cartilage was comparable to medium-hard rubber. Previous investigators found that the mean instantaneous deformation of medium-hard rubber was not sensitive to its thickness provided that its thickness was greater than 2 mm, about the thickness of human cartilage on the distal femur.

Therefore, using 3 mm thick cartilage, the author assumed that Young's modulus could be determined using the equation,

$$E = \frac{P}{2.67 w_o a} \qquad \text{Eq. 2.2}$$

Equation 2.2 was derived from the solution of an elastic punch problem for an incompressible, linearly elastic medium of infinite depth, at equilibrium with a shear modulus of,

$$\mu = \frac{P(1 - \nu)}{4w_{\circ}a} \qquad \text{Eq. 2.3}$$

where: μ = shear modulus

Substituting Poisson's ratio, $\nu = 1/2$, and Young's modulus, $E = 3\ \mu$, into Eq. 2.3 results in the development of Eq. 2.2.

Using Eq. 2.2, the author determined the 'instantaneous Young's modulus' for human patella (using w @ t=0.8s) = 2.28 MPa, and the 'equilibrium Young's modulus' (using w @ t=1hr) = 0.69 MPa.

A drawback of the model is the non-linearity of deformation of linearly elastic medium. This behaviour contradicts the assumption used in the derivation of the expressions for E and μ.

Hayes et al (1972) developed a mathematical model for the behaviour of an elastic layer backed by a rigid half-space (representing subchondral bone) indented by a rigid, spherical flat-ended indentor. These authors developed a model to determine scale coefficients for plane and spherically-ended indentors. The model assumed a linearly elastic, homogeneous and isotropic layer of infinite width (to avoid edge effects) attached to a rigid foundation. The displacement for the elastic layer at equilibrium was determined. An expression for Young's modulus for a plane-ended indentor was determined to be,

$$E = \frac{P(1 - \nu^2)}{2w_\circ a\kappa(a/h,\nu)} \qquad \text{Eq. 2.4}$$

where: κ is derived from the solution of the integral equation

The authors concluded that the depth of indentation, $w_\circ$, was very sensitive to the aspect ratio, a/h, since the magnitude of 'a' was generally less than 'h'.

A limitation of this Eq. 2.4 is that it is applicable at only two times during the loading cycle. At $t=0+$, at the initial instant of loading, when Poisson's ratio is assumed to be $\nu=0.50$, and at equilibrium, after load relaxation. Although the value for Poisson's ratio at equilibrium is not known, it is taken to be less than 0.5, account for compressibility of the matrix.

Similar results were obtained for a spherical-ended indentor. However, the change in size of the contact area with changing magnitude of load further complicated this model.

Hori and Mockros (1976) also modelled a layer of linearly elastic material attached to a rigid foundation indented with a flat-ended and spherical-ended indentor. The 'short-term' shear modulus, μ, and Poisson's ratio, ν, were determined for healthy and degenerated osteoarthritic cartilage. Measurements were taken at $t=1$s, after application of the load, and a range of values for the short-term shear modulus of 0.46 Mpa $\leq \mu \leq 3.47$ Mpa, and for Poisson's ratio of $0.42 \leq \nu \leq 0.49$, were determined for healthy and degenerated cartilage.

Askew and Mow (1978) developed a model of cartilage and bone in which cartilage was modelled as an elastic, non-homogeneous, anisotropic, layered continuum. The aspect ratio (loaded area to cartilage layer thickness), and the material constants of the layers were varied in the model.

When the aspect ratio was large, the authors stated that tensile stresses were not likely to occur at the surfaceand that large tensile radial strains would develop in the region of cartilage under the load. They concluded that a large aspect ratio does not allow cartilage to spread the load through the thickness of the layer to the subchondral bone.

An assumption of this model is that the elastic modulus in each of the layers was assumed to be equal for both tension and compression. However, tension in cartilage is resisted primarily by collagen, whereas compression is resisted by proteoglycans and water and the compressive modulus of the proteoglycans and water has a magnitude which is significantly larger than that for collagen.

In addition to modelling cartilage tissue, elastic models have also been used to model joints. Greenwald, & O'Connor (1971) developed a model to determine the transmission of load through the human hip joint. Due to the incongruity between apposing joint surfaces, the location and magnitude of the contact area between the surfaces depends on the magnitude and direction of the applied load. These authors estimated the contact areas for various loads approximating those encountered at a normal walking gait, see Figure 12. The analysis demonstrated the dependence of the contact area on the applied load.

The authors concluded that the function of joint incongruity was to allow the articular cartilage surfaces to remain separated at lower loads in order that the cartilage could be

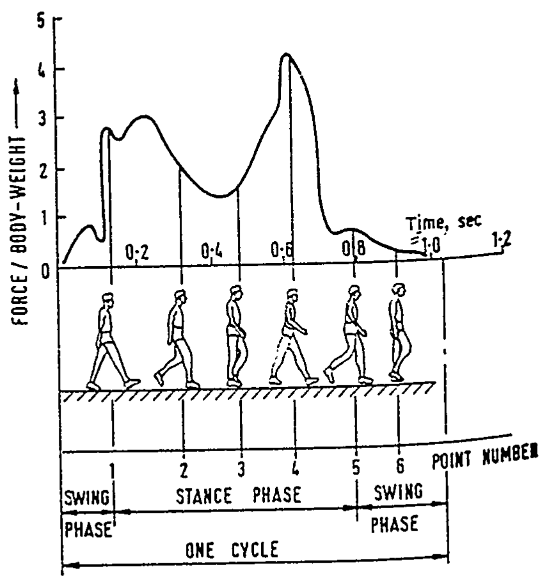

Figure 12
Magnitude of the resultant force transmitted through the hip during walking (Greenwald et al., 1971)

exposed to synovial fluids for lubrication and nutritional purposes. At heavier loads, the cartilage thickness resisted large pressures through hydrostatic pressure, without fluid flow.

Eberhardt et al (1990) developed an elastic analytical model which simulated an articulating joint in order to determine the stress distribution in the cartilage layer and bony substrate, see Figure 13(a). Stresses at the interface between layer and substrate, were estimated and the effects of varying layer thickness, layer and substrate stiffness, and contact radii were studied.

The model consisted of a cylindrical elastic disk within an elastic cylindrically concave half-space representing two bones. An elastic layer lining both disk and half-space simulated the articular cartilage at the end of the bones in the joint. The contact between the two surfaces in this model was assumed frictionless.

The authors found that the stress distribution in a tissue was proportional to the aspect ratio (ratio of contact radius to layer thickness), a/h. Tensile stresses were observed only when the aspect ratio was small, a/h=1

Tensile strains, however, were present for all three aspect ratios tested, (a/h=1,3,5). Significant shear stresses were observed at the cartilage-bone interface, suggesting that shear-induced horizontal cracking may occur at this location.

Eberhardt et al (1991a) incorporated the effect of tangential load and friction into their analytical model of an articulating joint. Their model consisted of two identical elastic

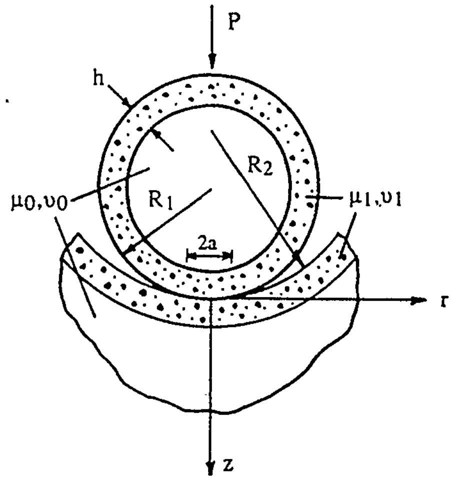

(a) 1990

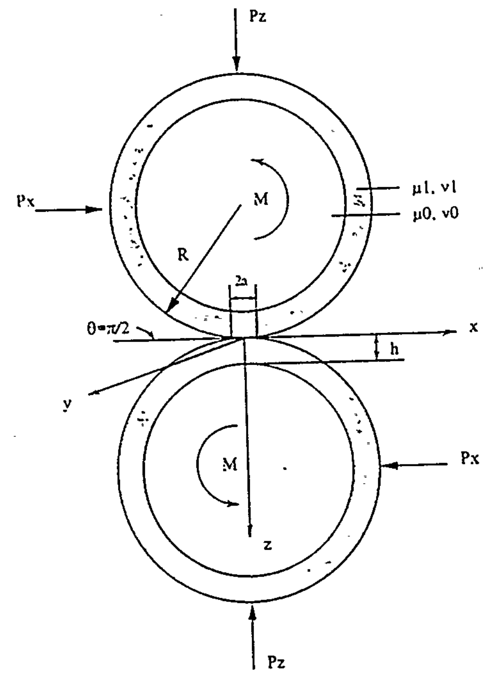

(b) 1991 (a)

(c) 1991b)

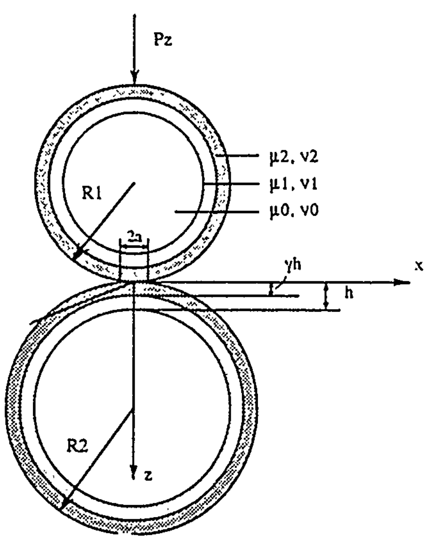

Figure 13
Analytical Model of Joint Contact
(Eberhardt et al., 1990; 1991a; 1991b)

spheres, with identical elastic layers (radius 'R', layer thickness 'h') loaded with compressive force 'P' see Figure 13(b).

The authors found significant surface tension in the model only when the friction coefficients were exceptionally high, or (similar to the frictionless model) when l/h small. The authors concluded that surface cracks observed after joint impact result from tensile failure due to an unusually high coefficient of friction (f=0.1), small contact areas, or factors not accounted for in the study.

A possible drawback of this model arises from the use of a static model to describe impact loading on cartilage. As a result, dynamic factors accompanying the effects of impact loading such as apparent changes in cartilage stiffness were not considered in this analysis.

Eberhardt et al (1991b) further modified their analytical model by adding a second elastic layer to each contacting sphere, see Figure 13(c). Three layer-layer-substrate combinations were analyzed:

1) cartilage/zone of calcified cartilage (ZCC)/bone
2) cartilage/subchondral bone/cancellous bone
3) STZ/cartilage/bone

A stress analysis was performed to determine which two-layer system combination produced tensile stresses induced by normal, frictionless loading.

The STZ cartilage was modelled four times stiffer than the underlying cartilage and the ZCC was modelled either 1/2 or 4 times stiffer than the underlying bone.

The authors determined that the current model, which incorporated a surface tangential zone, indicated that cartilage stresses were a function of the aspect ratio, a/h. Vertical tensile stresses were shown to develop when the middle layer was stiffer than the surrounding layers, suggesting that the ZCC or subchondral bone plays a role in impact load-induced osteoarthritis.

2.6.1.2 Single - Phase - Viscoelastic Models

Elastic models have been successfully used by many researchers to determine the structure-function relationship of cartilage in compression; the sensitivity of an indented specimen to the aspect ratio; Young's modulus; shear modulus; Poisson's ratio, to mention a few. Unfortunately, the results are applicable only at equilibrium, when the movement of interstitial fluid has ceased, and the resulting dissipative forces have balanced.

Elmore et al (1963) were among the first investigators to look at the role of fluid flow in functioning cartilage. The authors used an indentor model of cartilage and showed that the creep response observed in the cartilage could be explained from the outflow of interstitial fluid from the cartilage. The authors also observed that removal of the load led to complete recovery only when the exuded fluid was present outside the tissue to re-enter the cartilage.

Kempson et al. (1971) developed a "two-second creep modulus:" which included the initial elastic response as well as a small portion of the creep response of cartilage subjected to compression.

Intact cartilage was indented in different locations, keeping the applied load (22.2N), and the testing conditions constant. Deformation-Time curves were recorded which showed an initial instantaneous deformation followed by creep. Complete recovery occurred upon removal of the load only when the testing environment was kept constant.

Hayes and Mockros (1971) developed a viscoelastic model of articular cartilage which took into account the elastic and viscous behaviours of the tissue. The authors modelled the creep response of the cartilage as a series of springs and dashpots known as Kelvin solids, see Figure 14. This model was used to describe the mechanical behaviour of the cartilage. The creep compliance was expressed mathematically as:

$$F(t) = F_{o} + \sum_{i=1}^{k} F_i(1-e^{-\lambda_i t}) \qquad \text{Eq. 2.5}$$

Two equations were developed to represent the bulk and shear compressive viscoelastic behaviours of the tissue. A time-dependent strain curve was then fitted to each equation.

In a similar manner, Coletti et al. (1972) modelled cartilage as a single spring, or Hookean body in series with a dashpot, or Newtonian body to form a Kelvin-Voigt body, in order to describee the physical behaviours of these tissues.

Parsons and Black (1977; 1979) studied the *in vitro* viscoelastic mechanical response of normal articular cartilage of the distal femur of rabbit indenting the tissue with an

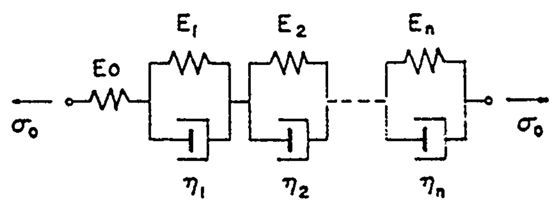

Figure 14
Spring and dashpot representation of a generalized Kelvin solid
(Hayes et al., 1971)

axisymmetric plane-ended indentor. These authors quantified shear moduli and retardation-time spectra that characterized time-dependent viscoelastic behaviour of intact cartilage. Also, numerical correlations between shear moduli, retardation-time spectra, and ionic concentration were correlated and found to be consistent with the structure and physio-chemical composition of cartilage.

Woo et al. (1979) studied the tensile properties of articular cartilage and developed a quasi-linear viscoelastic model, which assumed that the kernel of the stress-strain history integral was a function of strain and time.

2.6.2 Two-Phase Theories

Viscoelastic models of cartilage have been used to determine the influence of fluid flow, two-second creep modulus, and *in vitro* mechanical response of indented articular cartilage. These models successfully illustrated the time-dependent mechanical behaviour of articular cartilage.

Cartilage indentation tests have documented the importance of interstital fluid movement in cartilage creep. Thus, to develop a realistic model of articular cartilage, the tissue would be better approximated if the interstitial fluid wereas a distinct phase. Such biphasic models, were developed where one phase represents the interstital fluid, and the other phase represents the solid matrix and cells.

Historically, two somewhat different approaches have been used to develop biphasic models of cartilage: (a) Consolidation Theory, which has its roots in soil mechanics, and

(b) Biphasic Mixture Theory, which was developed by biomechanical engineers. Fortunately, comparison of the two theories indicates that both theory formulations solve the same set of equations written for each of the solid and fluid phases.

2.6.2.1 Consolidation Theory

Soil under load does not deflect instantaneously under load, but settles gradually at a variable rate. Such settlement is particularly noticeable in clays and sands saturated with water. The settlement is caused by a gradual adaptation of the soil to the load variation. This process is known as soil consolidation.

2.6.2.1.1 Terzaghi Model

In analyzing and designing foundations for structures, engineers are interested in the rate and magnitude of settlement which can be described bye Eq. 2.6.

$$S_t = S_i + S_c + S_s \qquad \text{Eq. 2.6}$$

where: S_t = the total settlement

S_i = the immediate settlement, although not actually elastic; is usually estimated by using elastic theory

S_c = the consolidation (time-dependent) settlement

S_s = the secondary compression (time dependent)

Consolidation settlement is a time-dependent process that occurs in saturated fine-grained soils that have a low coefficient of permeability.

The following summarize the assumptions used by Terzaghi (Holtz & Kovacs, 1981) in his one-dimensional consolidation theory analysis for a compressible soil layer:

- homogeneous
- completely saturated with water
- mineral grains in the soil and water in the pores are completely incompressible
- Darcy's law governs egress of water from soil pores. Darcy's law states that the rate of flow in clean sand is proportional to the hydraulic gradient (Holtz & Kovacs, 1981)
- drainage and compression are one-dimensional
- applied load increments produce only small strains in the soil, thus the coefficient of compressibility and the Darcy coefficient of permeability are essentially constant
- no secondary compression occurs

The derivation of the Terzaghi model considers the volume of water flowing out of a differential compressible soil element.

Assuming an infinitesimally small cube of soil with dimensions dx, dy, dz at a depth z below the top of the compressible layer, see Figure 15, the Hydraulic gradient, i_z, at the top of the element is:

$$i_z = \frac{\text{head loss}}{\text{distance}} = \frac{\delta}{\delta z}\frac{u}{\rho_w g} = \frac{1}{\rho_w g}\frac{\delta u}{\delta z} \qquad \text{Eq. 2.7}$$

where: u = the pore water pressure

ρ_w = the density of water

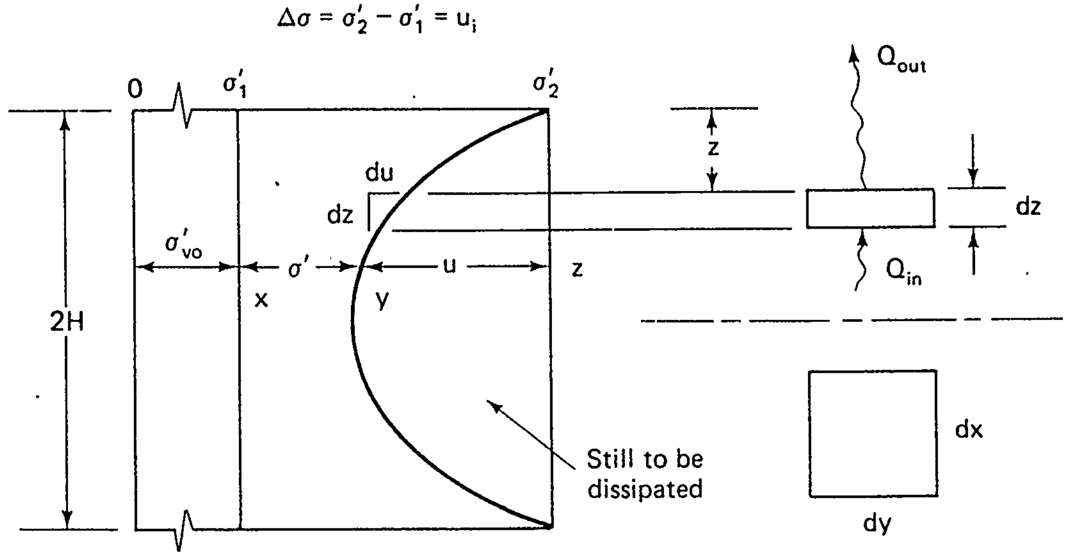

Figure 15
Soil Undergoing Compression
(Holtz et al., 1981)

dz = the height of the cube

g = gravity

The Hydraulic gradient, i_{z+dz}, at the bottom of the element is given by

$$i_{z+dz} = \frac{1}{\rho_w g}\frac{\delta u}{\delta z} + \frac{1}{\rho_w g}\frac{\delta^2 u}{\delta z^2}dz \qquad \text{Eq. 2.8}$$

From Darcy's Law,

$$dQ = kiadt \qquad \text{Eq. 2.9}$$

where: dQ = the quantity of fluid flow in the element

k = Darcy coefficient of permeability

i = the hydraulic gradient

a = the area of the element

dt = time

The quantity of flow dQ in time dt out of the top of the element is

$$dQ_{out} = k\frac{1}{\rho_w g}\frac{\delta u}{\delta z} dz\ dx\ dy\ dt \qquad \text{Eq. 2.10}$$

The quantity of flow in time dt at the bottom into the element is:

$$dQ_{in} = k\frac{1}{\rho_w g}\left(\frac{\delta u}{\delta z} + \frac{\delta^2 u}{\delta z^2}\right) dz\ dx\ dy\ dt \qquad \text{Eq. 2.11}$$

Therefore,

Volume change/unit cross-sectional area = $dQ_{out} - dQ_{in}$

$$= \frac{-k}{\rho_w g}\frac{\delta^2 u}{\delta z^2} dz\ dt \qquad \text{Eq. 2.12}$$

The coefficient of compressibility, a_v is:

$$a_v = \frac{-de}{d\sigma'} = \frac{e_1 - e_2}{\sigma_2' - \sigma_1'} \qquad \text{Eq. 2.13}$$

where: e_1-e_2 = the change in the void ratio. Void ratio $= \dfrac{\text{Vol. of voids}}{\text{Vol. of solids}}$

σ_2', σ_1' = the change in the effective stress.

σ' = $\sigma - u$

σ = the total normal stress

u = the pore water pressure

and the settlement of the element, s is:

$$s = \Delta\, dz = \frac{-de}{1 + e_1}\, dz \qquad \text{Eq. 2.14}$$

where e_1 corresponds to the initial void ratio

From Eq. 2.13,

$$-de = a_v\, d\sigma' \qquad \text{Eq. 2.15}$$

Therefore,

$$\Delta\, dz = \frac{a_v\, d\sigma'}{1 + e_1}\, dz \qquad \text{Eq. 2.16}$$

Any change in effective stress is numerically equal to the negative of the change in excess pore water pressure.

$$\Delta\sigma' = -\Delta u \qquad \text{Eq. 2.17}$$

Therefore,

$$\Delta dz = \frac{-a_v\, du}{1 + e(1)} dz \qquad \text{Eq. 2.18}$$

Since $du = (\frac{\delta u}{\delta t})\, dt$

$$\Delta dz = \frac{-a_v}{1 + e_1} \frac{\delta u}{\delta t} dt\, dz \qquad \text{Eq. 2.19}$$

Equating Eq. 2.12 with Eq. 2.19:

$$\frac{-k}{\rho_w g} \frac{\delta^2 u}{\delta z^2} dz\, dt = \frac{-a_v}{1 + e_1} \frac{\delta u}{\delta t} dt\, dz \qquad \text{Eq. 2.20}$$

$$c_v \frac{\delta^2 u}{\delta z^2} = \frac{\delta u}{\delta t} \qquad \text{Eq. 2.21}$$

$$\therefore \qquad c_v = \frac{k}{\rho_w g} \frac{1+e_1}{a_v} \qquad \text{Eq. 2.22}$$

where: c_v = coefficient of consolidation

Solution of this partial differential equation gives the distribution of pore pressures as a function of time and depth in the soil layer.

The boundary conditions for the case of one-dimensional consolidation are as follows:

$z = 0$, $\frac{\delta u}{\delta z} = 0$ for $0 \leq t$ Impermeable boundary at base

$z = H$, $u = 0$ for $0 \leq t$ Free-draining surface

$0 \leq z \leq H$, $u = p$ for $t = 0^+$ This implies that the fluid phase in the layer resists the applied load but at the surface, pressure = 0 since water is free to exude.

$$\therefore \qquad u(z,t) = \frac{4}{\pi} p_1 \sum_{n=0}^{\infty} \frac{1}{2n+1} \sin\left(\frac{(2n+1)\pi z}{2H}\right) \exp\left[\frac{-n(2n+1)^2\pi^2 c_v t}{4H^2}\right] \qquad \text{Eq. 2.23}$$

Since vertical settlement, δz, is due to the reduction in void spaces within the soil, for a layer of soil

$$\frac{d\delta z}{dz} = \Delta h \qquad \text{Eq. 2.24}$$

where Δh = decrease in porosity due to an increase in effective stress on the solid matrix

$= m_v (p_1 - u)$

p_1 = applied total stress

m_v = coefficient of volume

$$\frac{d\delta}{dz} = m_v(p_1 - u) \qquad \text{Eq. 2.25}$$

Substituting Eq. 2.25 into Eq. 2.23 for the variable, u, and integrating over the thickness, H, the displacement at the top of the soil layer is,

$$\delta(H,t) = m_v p_1 H \left[1 - \frac{2}{\pi^2} \sum_{n=0}^{\infty} \frac{1}{(n+\frac{1}{2})^2} \exp\left[\frac{-(n\,\frac{1}{2})^2\pi^2 c_v t}{H^2}\right]\right] \qquad \text{Eq. 2.26}$$

2.6.2.1.2 Biot Model

Terzaghi's treatment is restricted to the one-dimensional problem of a column under a constant load. Biot (1955) extended Terzaghi's treatment to the three-dimensional case, and established equations valid for any arbitrary load variable with time.

Similar to Terzaghi's assumptions, the following basic properties of the soil are assumed:

1. soil is isotropic
2. reversibility of stress-strain relations under final equilibrium conditions
3. linearity of stress-strain relations
4. small strains
5. water in pores is incompressible
6. water may contain air bubbles
7. water flows through porous skeleton according to Darcy's Law.

The model considers a small cubic element of consolidating soil. This element is assumed to be large enough compared to the size of the pores so as to be treated as homogeneous. The average stress condition in the soil, represented by forces uniformly distributed on the cube element faces must satisfy the equilibrium conditions of a stress field:

$$\frac{\delta\sigma_x}{\delta x}+\frac{\delta\tau_z}{\delta y}+\frac{\delta\tau_y}{\delta z}=0$$

$$\frac{\delta\tau_z}{\delta x}+\frac{\delta\sigma_y}{\delta y}+\frac{\delta\tau_x}{\delta z}=0$$

$$\frac{\delta\tau_y}{\delta x} + \frac{\delta\tau_x}{\delta y} + \frac{\delta\sigma_z}{\delta z} = 0 \qquad \text{Eq. 2.27}$$

where: τ,σ = the stress components acting on the element faces, dx, dy, and dz

In order to describe completely the macroscopic condition of the soil we must consider the average stress in the skeleton of the soil, and the stress caused by the hydrostatic pressure of the water filling the pores.

$$\sigma_x = 2G(e_x + \frac{\nu\varepsilon}{1 - 2\nu}) - \alpha\sigma$$

$$\sigma_y = 2G(e_y + \frac{\nu\varepsilon}{1 - 2\nu}) - \alpha\sigma$$

$$\sigma_z = 2G(e_z + \frac{\nu\varepsilon}{1 - 2\nu}) - \alpha\sigma \qquad \text{Eq. 2.28}$$

$$\tau_x = G\Upsilon_x$$

$$\tau_y = G\Upsilon_y$$

$$\tau_z = G\Upsilon_z \qquad \text{Eq. 2.29}$$

with $$\alpha = \frac{2(1 + \nu)G}{3(1 - 2\nu)H} \qquad \text{Eq. 2.30}$$

where: G = shear modulus

ν = Poisson's ratio

σ = pore pressure

e = strain

$\frac{1}{H}$ = coefficient (a measure of the compressibility of the soil for a change in water pressure)

α = the ratio of the water volume squeezed out to the volume change of the soil if the latter were compressed while allowing the water to escape

$$\varepsilon = e_x + e_y + e_z$$

Substituting Eq. 2.28 into Eq. 2.27, stresses into the equilibrium conditions, result in

$$G\nabla^2 u + \frac{G\delta\varepsilon}{1-2\nu\delta x} - \alpha\frac{\delta\sigma}{\delta x} = 0$$

$$G\nabla^2 v + \frac{G\delta\varepsilon}{1-2\nu\delta y} - \alpha\frac{\delta\sigma}{\delta y} = 0$$

$$G\nabla^2 w + \frac{G\delta\varepsilon}{1-2\nu\delta z} - \alpha\frac{\delta\sigma}{\delta z} = 0 \qquad \text{Eq. 2.31}$$

$$\nabla^2 = \frac{\delta^2}{\delta x^2} + \frac{\delta^2}{\delta y^2} + \frac{\delta^2}{\delta z^2} \qquad \text{Eq. 2.32}$$

This gives three equations with four unknowns, displacements, u, v, w, and water pressure, σ. Biot introduced Darcy's Law governing the flow of water in a porous medium to develop the equation for excess pore pressure and volumetric strain

$$k\nabla^2 p = \alpha\frac{\delta\varepsilon}{\delta t} + \frac{1\delta\sigma}{Q\delta t} \qquad \text{Eq. 2.33}$$

where: k = the coefficient of permeability of the soil

$\frac{1}{Q}$ = a coefficient which is a measure of the amount of water which can be forced into the soil under pressure while the volume is kept constant

2.6.2.2 Biphasic Mixture Theory

Torzilli and Mow (1976) developed a biphasic model for articular cartilage which was continued by Mow and Lai (1979) and Mow et al (1980). This model assumed cartilage to be a soft, porous, and permeable, elastic solid that is saturated with fluid. The model assumes that both phases of cartilage are intrinsically incompressible. The continuity equation specified for this binary mixture is:

$$\mathrm{div}\ v^f + \alpha\ \mathrm{div}\ v^s + \alpha(v^s - v^f)\mathrm{grad}\ \ln\rho^s = 0 \qquad \text{Eq. 2.34}$$

where: v^f = velocity of the fluid phase

v^s = velocity of the solid phase

ρ^s = apparent density of the solid

α = solid content

$= \dfrac{\text{solidity of tissue}}{\text{porosity of tissue}} = \dfrac{V_s/V_t}{V_f/V_t}$

V_s = tissue solid volume

V_t = Total volume of tissue

V_f = Fluid volume of tissue

Momentum-balancing equations for the two components of the mixture omitting inertial forces are:

$$\mathrm{div}\ \sigma^s - K(v^s - v^f) = 0 \qquad \text{Eq. 2.35}$$

and

$$\mathrm{div}\ \sigma^f + K(v^s - v^f) = 0 \qquad \text{Eq. 2.36}$$

where: σ^s = apparent stress tensor for solid phase

σ^f = apparent stress tensor for fluid phase

$d(v^s - v^f)$ = diffusive drag arising from the relative velocities between fluid and solid components

K = diffusive coefficient

Mow and Lai (1980) found that under slow flow conditions, the diffusive coefficient was related to the permeability, k, of the tissue

$$k = \frac{1}{(1+\alpha)^2 K} \qquad \text{Eq. 2.37}$$

These authors developed a theory to model the biphasic nature of cartilage, known as the KLM biphasic theory for cartilage which assumes the solid phase to be isotropic and linearly elastic, and the interstitial fluid to be inviscid. Assuming small strains, the isotropic stress - strain relationship for the solid phase is:

$$\sigma^s = -\alpha p I + \lambda_s e I + 2\mu_s e \qquad \text{Eq. 2.38}$$

and for the fluid phase

$$\sigma^f = -pI \qquad \text{Eq. 2.39}$$

where: p = apparent fluid pressure

λ_s, μ_s = the intrinsic elastic moduli of the solid matrix in the mixture

e = infinitesimal strain tensor describing the deformation of the solid matrix

The tissue is assumed to be partially homogeneous, thus λ_s and μ_s are constants.

Mansour and Mow (1976) showed that permeability was dependent upon the strain present in the tissue.

Mak, Lai, & Mow (1987) developed a mathematical solution for the indentation creep and stress relaxation behaviour of articular cartilage. The cartilage was modelled as a layer of KLM biphasic material of thickness, h, bonded to an impervious, rigid bony substrate. The circular, plane-ended indentor was assumed to be rigid, porous, free draining and frictionless. When indented under these conditions, cartilage behaves like an incompressible, single-phase elastic solid at $t = 0$ where the instantaneous response of the material being governed by the shear modulus, μ_s, of the solid matrix.

As $t \rightarrow \infty$, the tissue behaves like a compressible elastic solid, with material properties defined by those of the solid matrix: λ_s, μ_s or μ_s, λ_s .

At $0 < t < \infty$, the transient viscoeleastic creep and stress-relaxation behaviour of the material is controlled by the functional drag of fluid through the solid matrix.

The indentation stress-relaxation behaviour of the layer is governed by the rate of compression parameter, $R_\circ = \frac{H_A k}{V_\circ h}$;

where: H_A = aggregate modulus of solid matrix

k = permeability coefficient

$V_\circ$ = rate of compression imposed on indentor

h = thickness of biphasic medium;

the intrinsic Poisson's ratio of the solid matrix, ν_s ; the aspect ratio $A = a/h$; and the magnitude of the compressive strain.

When $\nu_s = 0.5$, no stress relaxation is possible since the solid matrix is intrinsically incompressible and no mechanism exists to generate the pressure necessary for intrinsic fluid flow.

Mow et al. (1989) used the indentation analysis of Mak et al. (1987) to describe the time-dependent indentation creep behaviour of cartilage in situ. Mow et al. (1989)developed a method to calculate H_A, ν_s, k , and found the following for bovine knee joints, see Table 2.1:

Table2.1

Intrinsic Properties of Bovine Knee Joint Cartilage

Site	**No. Tested**	**H_A** (MPa)	**k** $\frac{m^4}{Ns} \times 10^{15}$	**ν_s**	**h** (mm)
Lateral Condyle	10	0.89±0.29	0.43±0.20	0.40±0.02	0.94±0.17
Medial Condyle	10	0.90±0.43	0.46±0.33	0.38±0.05	1.19±0.24
Patellar Groove	10	0.47±0.15	1.42±0.58	0.25±0.07	1.38±0.19

The authors noted that the permeability of the patellar groove cartilage was several times higher than that of the femoral condyle. They interpreted the results to indicate that material property variations are likely due to tissue composition and layer thickness variations within any articular cartilage surface, as previously demonstrated by Kempson et al., (1971). Brown & Singerman (1986) loaded human fetal proximal femoral chondroepiphyses cartilage in uniaxial peripherally-unconfined indentation tests, using a ramp/plateau input strain history. The authors analyzed the corresponding load vs time curves in terms of the KLM model, allowing calculation of permeability, equilibrium modulus and solid-phase Poisson ratio for the material. The authors found that their algorithm to evaluate the biphasic solution yielded a close fit to the KLM parametric plots. However, substantial underestimation of the transient response component related to fluid transport resulted in a poor approximation between the specimen behaviour and KLM theory.

The authors suggested that experimental results derived from theoretical predictions often indicate the shortcomings in the KLM theory to account for factors such as nonlinear behaviour and platen constraints.

Mansour et al. (1976) determined the permeability of articular cartilage under conditions approximating those found in normally functioning synovial joints, see Figure 16.

The authors found that an increase in compressive strain of the tissue caused an increase in compaction of the collagen network and an increase in frictional resistance to interstitial fluid flow. In cartilage, compressive strain also causes compaction of proteoglycans effectively increasing tissue fixed charge density, causing a lowering in tissue permeability.

2.6.2.3 Comparison of Consolidation Theory and Biphasic Mixture Theory

Van der Voet (1992 PhD dissertation) compared the Biot poroelasticity theory with a linearized version of Mow's biphasic mixture theory and found that the poroelastic and

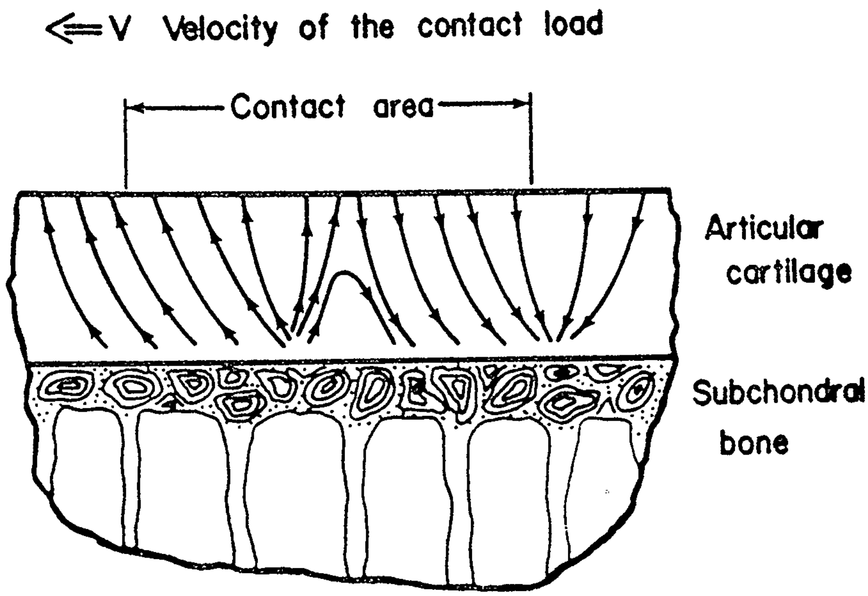

Figure 16
Schematic representation of the fluid flow through articular cartilage as it is subjected to a sliding load during joint function. The arrows within the cartilage indicate the direction of fluid flow
(Mansour et al., 1976)

mixture theory formulations solve the same set of equations for each of the solid and fluid phases:

$$\nabla \cdot (\mathbf{T}^s) + \pi^s = 0 \qquad \text{Eq. 2.41}$$

$$\nabla \cdot (\mathbf{T}^f) - \pi^f = 0 \qquad \text{Eq. 2.42}$$

Whereas Mow and Lai (1980) derived a continuity equation for the fluid and solid phases of the mixture, Biot (1955) did not propose an equation of this type.

Van der Voet et al. (1992) applied the poroelasticity theory to models of articular cartilage. Four tests were performed:

- confined compression test
- unconfined compression test
- unconfined indentation test
- test to determine effect of indentor loading rate on measured reaction force

Numerical elements based on poroelasticity were compared to published values of models assuming the Biphasic Theory. The results of these tests verified that the use of poroelasticity theory was appropriate for modelling of articular cartilage.

2.6.3 Biphasic Models of Articular Cartilage

2.6.3.1 Biphasic Models - Application of the Consolidation Theory

Zarek and Edwards (1965) applied the Consolidation Theory to statically and dynamically loaded cartilage in order to explain the tissue's behaviour qualitatively. These authors suggested that as the joint is loaded, a non-uniform contact occurs between the two apposing joint surfaces. This non-uniform contact was assumed to result from the incongruity of the upper and lower joint surfaces. Contact produces stresses in the cartilage layers causing excess pore pressure to build up in the tissue under the area of contact. Pressure gradients within the tissue force the free pore fluid into regions of low pore pressure, namely regions of unloaded tissue, where pore pressures are considered effectively zero.

At $t = 0+$, a condition of incompressibility exists in the loaded tissue. The authors explained that the fluid is prevented from flowing immediately upon loading due to entrapment by the solid matrix. As a result, the volume of the cartilage is maintained by lateral dilation countering the initial compressive displacements.

However, once fluid flow begins within the tissue, the load is transferred from the fluid to the solid components. The authors also explain that the applied stress is reduced within the tissue through deformation of the matrix, causing an increase in the area over which the load acts. Over time, equilibrium is reached within the tissue.

Oloyede et al (1992), investigated the influence of loading velocity on the stiffness of the articular cartilage matrix. The authors conducted compression tests on cartilage alone, and cartilage on bone at strain rates ranging from 10^{-5} sec^{-1} to 10^{3} sec^{-1} . These authors found that two fundamentally different mechanisms of deformation control the development of cartilage matrix stiffness.

At low strain rates (of deformation), the stress-strain curves were sensitive to changes in the indentation rate of the indentor. On impact loading, the stress-strain curves showed little change from the stress-strain curve for cartilage loaded at a slower rate.

Thus, consolidation models successfully approximate the time-dependent behaviour of cartilage. These models assume that the applied loads are shared between the solid and fluid phases of the tissue; and that the material is homogeneous, isotropic, and linearly elastic.

2.6.3.2 FE Models - Application of Consolidation & Biphasic Mixture Theories

Spilker et al (1992) applied a finite element formulation of the linear biphasic theory to the stress-relaxation indentation problem. The indentation problem consisted of a layer of soft tissue of uniform thickness, h, attached to subchondral bone, an impermeable boundary, indented normal to the surface by a plane-ended cylindrical indentor of radius R_{ind}. The indentor was loaded at time t_o, by a compressive displacement of magnitude $u_o = h\varepsilon_o$. The indentor was modelled as a porous (free draining) or impermeable (solid), and the interface was assumed to be perfectly lubricated or perfectly adhesive.

The authors examined the effects of the stiffness of the subchondral bone on the response of the soft tissue and demonstrated that the subchondral bone substrate could be modelled as a rigid, impermeable boundary. The effects of a curved tissue-subchondral bone interface were also studied. Little difference in radial solid stresses and excess pore pressures were observed between models with parallel, convex, and concave bone interface shapes relative to the surface.

Wayne et al. (1989); Wayne et al. (1991) applied the finite element method, using the principle of virtual work, to the biphasic theory in order to develop a numerical method for articular cartilage behaviour analyses, see Figure 17. The unknown parameters were the solid displacements, u, and fluid pressures, p. The authors developed the algorithms and computer code for solving 2-D problems in plane stress, plane strain, and axial symmetry for both small and large strains. The model was validated with known analytical solutions. The model compared closely with analytical solutions for confined compression and unconfined compression under small strains, and for confined compression under large strains.

The model was also used to examine the mechanical properties of a repaired articular cartilage surface. The repaired cartilage had different material properties to normal cartilage($H_A^{repair} = 0.5H_A^{original}$; $k^{repair} = 2k^{original}$; $\nu_s^{repair} = 0$) .

The results indicated that in creep simulation, the softer, more permeable repair tissue had larger axial displacements and higher fluid flux directly under the applied load than that of normal cartilage. These results indicated the importance of the biomechanical properties of repair tissue used to repair diseased cartilage.

Spilker et al. (1988) developed a finite element model for hydrated soft tissues for confined and unconfined compression and indentation tests. Four-node axisymmetric elements were developed in which each node had 4 degrees of freedom; axial and radial

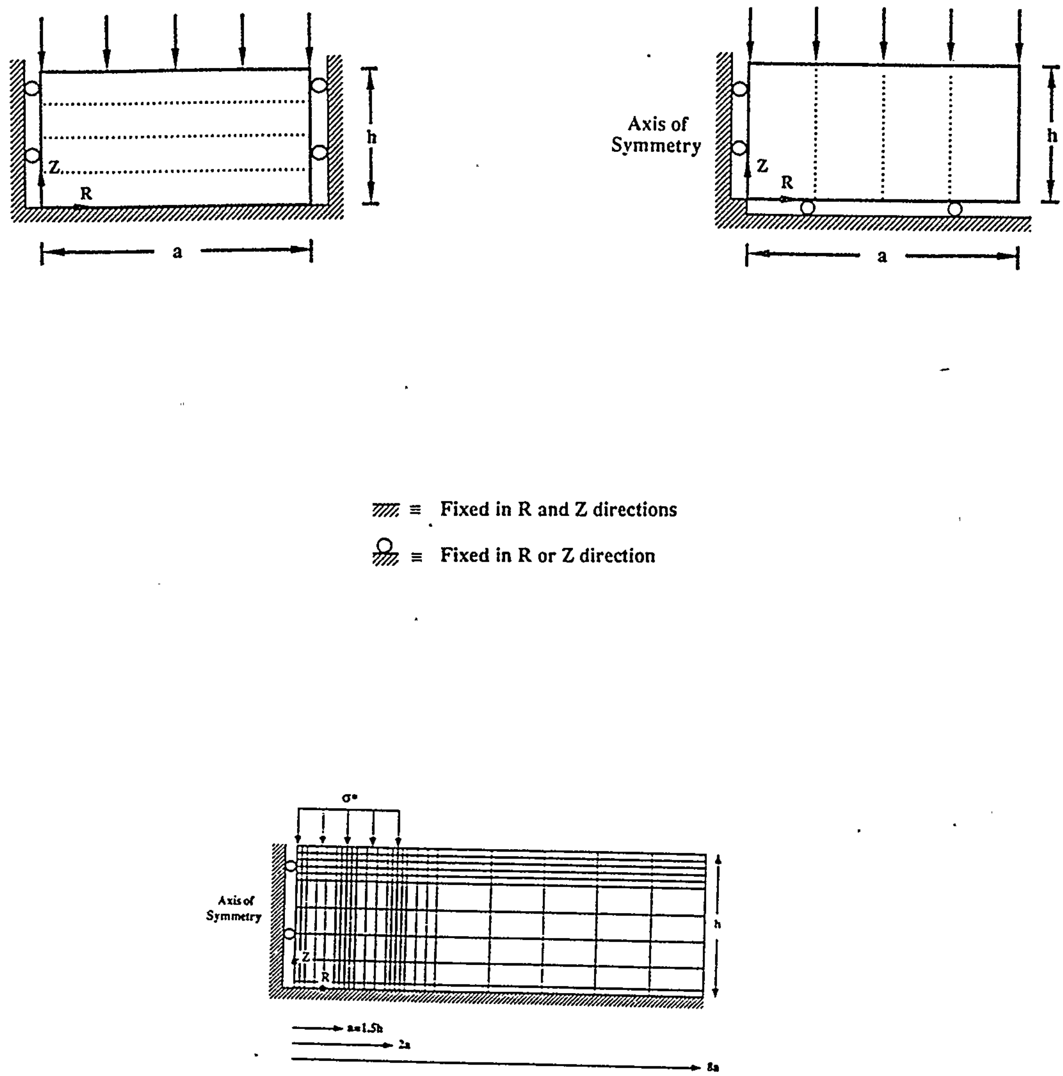

Figure 17
Finite element mesh and boundary conditions for a cartilage specimen of thickness 'h' and radius 'a'. (a) Confined compression (b) Unconfined compression (c) Repaired articular cartilage surface (Mow et al., 1992)

solid displacements; and axial and radial fluid velocities. A penalty formulation was used for the continuity statement to account for impermeability of the phases in order that continuity was achieved. The indentor model treated the indentor friction as an independent variable and allowed for nonlinear permeability of the cartilage.

The results of these models correlate well with previous solutions. For example, reaction forces were sensitive to nonlinear permeability only during the initial loading phase; adhesive or rough indentors affected the elastic solid of the tissue by providing confinement against lateral displacement; permeable or solid indentors were shown to influence the peak reaction force, but not the equilibrium reaction force. The peak reaction force was higher for solid indentors due to the presence of pore water under the indentor; frictional forces between fluid and solid prevent the fluid from flowing too rapidly, thus the presence of the water in the tissue increases the apparent stiffness of the tissue as the pore water under the indentor carries the load.

Vermilyea & Spilker (1992) used the finite element method to analyze a quarter plug model of articular cartilage in an unconfined compression test. The model used 10 node quadrahedral volume stress hybrid elements. Anisotropic material behaviour was simulated by directing the elastic moduli.

The authors plotted reaction force time histories and displacement histories along the axes of symmetry at mid-depth. The results suggested that the reaction forces were most sensitive to changes in stiffness in the depth of the section. For three other combinations of material constants, equilibrium, reaction forces differed little from the isotropic model, whereas displacements showed anisotropic behaviour, similar to results found by Mizrahi et al. (1986) in similar models.

Van der Voet (1992, PhD dissertation), applied the finite element method to develop a simulation of a displacement controlled indentation test, using the ABAQUS finite element code. Van der Voet's results were compared to those of Spilker et al. (1988). Results of the analysis were compared to Spilker et al. (1988), whose finite element model was based on the linear and non-linear KLM biphasic theory, with nodal displacements and nodal fluid velocities as unknown variables at each time step. Whereas the trends for both studies were similar, the peak reaction forces were somewhat higher using the ABAQUS model; centroidal strains were the same for both codes.

A 2-D axisymmetric model of a cartilage plug was developed using 8 noded axisymmetric, isoparametric elements for the tissue, and 8-noded axisymmetric, isoparametric continuum elements for the indentor, see Figure 18. Four models were developed: permeable/impermeable indentor and/or smooth/rough indentor surface. A permeable indentor was simulated by setting pore pressures under the indentor to '0', or rather by making the cartilage under the indentor free draining. For an impermeable indentor, the cartilage under the indentor was sealed. Slide line elements were used as interface elements between indentor and cartilage to permit frictionless sliding between indentor and cartilage in order to simulate a smooth indentor surface. A rough indentor surface was modelled by applying a constraint equation to the radial nodal displacements of the

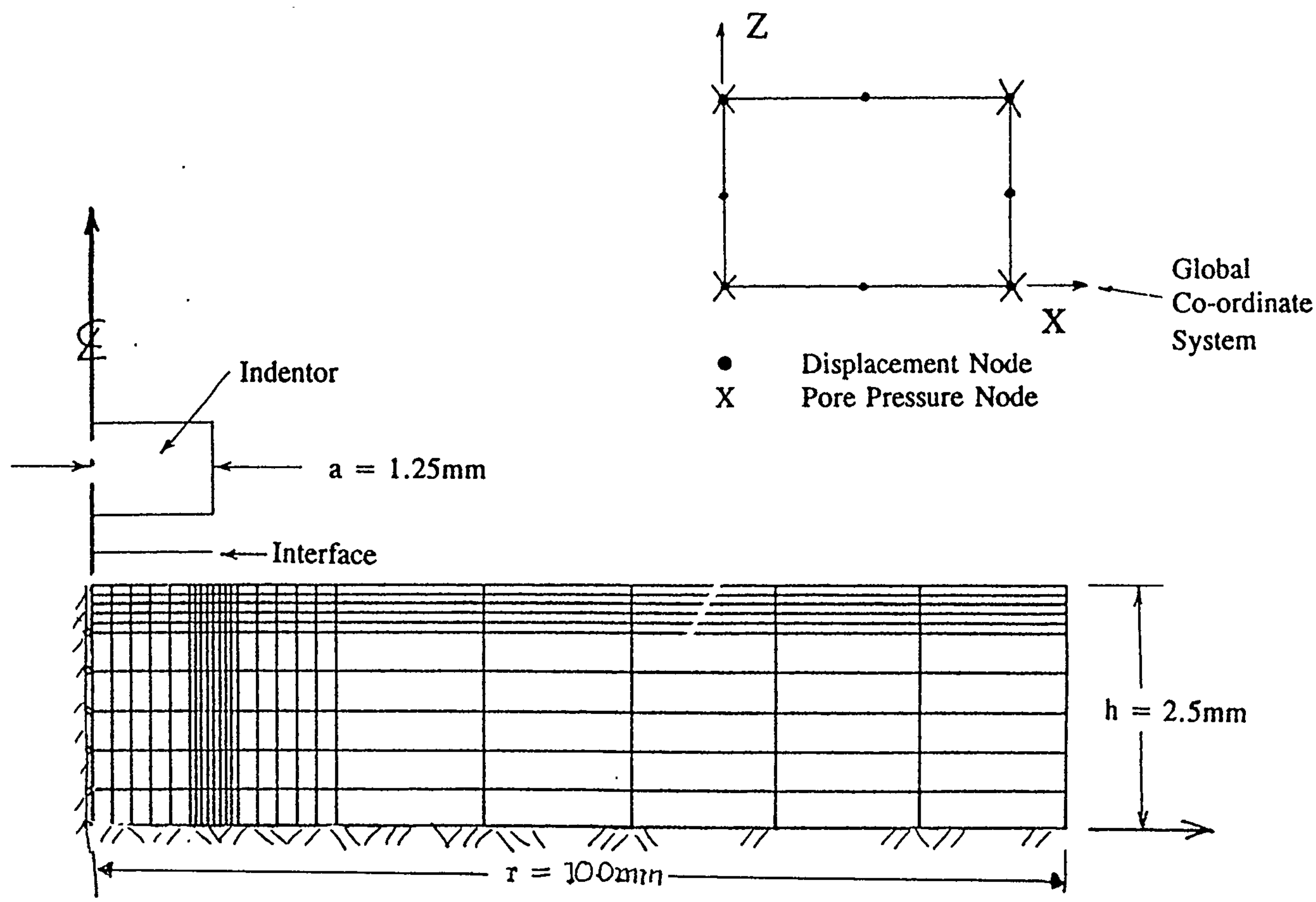

Figure 18
Finite Element Mesh to Model an Axisymmetric Indentation Test
(van der Voet, 1992)

indentor to those of the cartilage. A time-dependent displacement was applied to the top of the indentor.

The purpose of this analysis was to determine if indentation stiffness is affected by structural heterogeneity and mechanical anisotropy. The numerical indentation models revealed that indentation stiffness was insensitive to variations of anisotropy in the plane of the surface layer of articular cartilage. The author successfully replicated mechanical behaviours of cartilage in confined compression and indentation, and determined that indentation stiffness was sensitive to indentor roughness and permeability, cartilage layer geometry, and the displacement rate of the indentor.

Ateshian, & Wang (1994), investigated the role of interstitial fluid pressurization under the moving contact of joint articular surfaces. The analysis solved the problem of rolling and/or sliding frictionless cylindrical cartilage layers of arbitrary thickness and material properties, under steady state conditions. For small velocities, interstitial fluid pressurization is negligible, and the applied load is supported by the solid collagen - proteoglycan phase of the tissue, causing significant cartilage deformation. For physiologic surface velocities, matrix fluid pressurization supported 90% of the applied load. This resistance by the pressurizedfluid protects the solid matrix from high effective stress loading, and reduces matrix strains and deformations.

The shielding of matrix solids by the interstitial fluid increases as joint surfaces become more congruent, and with increasing magnitudes of compressive loads.

Conversely, fluid pressurization decreases when material properties characteristic of degenerative cartilage was used.

Wayne (1993), used the u-p finite element method to study the mechanical behaviour of articular cartilage modelled with joint geometry. A parabolically distributed stress was applied to the cartilage, and tissue response comparisons were made when 0%, 25%, or 50% of this stress was supported by the interstitial tissue fluid at the surface. These percentages represented the pressure buildup in the lubricating fluid of the joint. The study showed that, as a larger portion of the applied stress was taken up by the fluid:

1. the amount of fluid exuded axially from the tissue decreased,
2. the stress and strain generated in the solid matrix decreased,
3. the thickness reduction of the cartilage layer decreased.

These results suggest that generating intra-articular fluid pressure effects the mechanical behaviour of articular cartilage (and its function) *in situ*.

Another finite element analysis of articular cartilage was the development of a linear finite element model of articular cartilage, developed in order to map the temporal and spatial response of cartilage in the vicinity of a moderate size perforation in the subchondral bone (Bachrach et al., 1993). The mechanical effects of such a perforation are important for understanding how defects in the subchondral bone, such as those resulting from high impact loading, may affect the supported cartilage layer. The model is based on biphasic theory, and the perforation is assumed to be free-draining, thus allowing minute amounts of tissue fluid to escape the hydrostatic pressure.

The results of this study showed that, since the tissue fluid is free to flow out of the tissue, the solid matrix becomes the component, as opposed to the tissue fluid, which supports the load in the region of the hole. As the fluid begins to flow toward the hole, the hydrostatic pressure in its vicinity rapidly decreases. These results suggest that there is progressive tissue failure following a single impact load.

Van der Voet (1992 PhD dissertation) developed a plane strain finite element of a typical joint in order to estimate whether whole joints are affected by hydraulic boundary conditions. The author determined that hydraulically sealed boundaries at the surface of contacting nodes is a mechanically admissible condition for transmission of forces developed during stress relaxation.

With the growing interest in cell metabolism in tissues and its relation to mechanical loading, it is important to be able to perform tests wherein the mechanics are easily controlled. Indentation is the preferred test. The purpose here therefore is to use the finite element method to determine whether indentation can produce similar stress states to a normal joint, and if so, under what geometrical conditions.

2.6.4 Summary

Over the past three decades, researchers have developed numerous models of articular cartilage in attempts to understand its structural and functional behaviour. The advancements in the fundamental levels of theory applied to the behaviour of the tissue has produced more complex models of the articular cartilage layer.

The purpose of the present study is to compare the results obtained using the finite element method for time-dependent, unconfined indentation tests, with stress-relaxation tests of a diarthrodial joint to observe whether indentation can produce similar stress states to a normal joint, and if so, under what geometrical conditions. Estimates of the aspect ratio limit (r/h) for time-dependent indentation of cartilage will also be determined.

3.0 Finite Element Scheme - Poroelastic

ABAQUS (Hibbitt, Karlsson & Sorensen, Inc.,1994 (HKS)), is a commercial finite element code developed to solving complex finite element formulations such as those involving poroelastic materials in which elastic deformations and time-dependent creep deformations must be accounted for.

Using the Principle of Virtual Work, the following is obtained (HKS):

$$\begin{bmatrix} [K] & -[C] \\ -[C]^T & -\Delta t[H] \end{bmatrix} \begin{Bmatrix} \{u\} \\ \{p\} \end{Bmatrix} = \begin{Bmatrix} \{F\} \\ \{R\} \end{Bmatrix} \qquad \text{Eq. 3.1}$$

where: [K]= stiffness matrix of the structure

[C]= matrix which 'couples' fluid flow and equilibrium equations [mm^2]

[H]= permeability matrix.

{F}= known nodal forces

{R}= fluid flows

The upper row of the above equation represents the model's structural behaviour, whereas the lower row represents the hydraulic behaviour of the model.

This equation is iteratively solved for the unknown displacements, {u},and pore pressures, {p}.

3.1 Indentation Model

The purpose of this study is to compare the results of this study, where the indentor geometry is flat and indentor material properties are dissimilar to the articular cartilage with the results from a diarthrodial stress-relaxation model (to be developed later), where the indentor is another non-planar cartilage surface, to observe where within the contact zone of the joint model the results compare.

Estimation of the aspect ratio limit will also be determined.

3.2 Model Description - Indentor Model - Step 1

In the present study, the ABAQUS finite element code was used to model a simulation of a displacement-controlled indentation test. The results from the investigations of Spilker et al (1988) and Van der Voet (1992) were used for comparison.

3.2.1 Model Geometry

An axisymmetric model of cartilage was developed, see Figure 19. Axisymmetry was used in order to simplify the complexity of the model. The indentor is of radius, r=1.25mm, and the cartilage layer has a radius , R=10mm, and height, h=2.5mm.

The indentor edge was modelled with a rounded edge in order to avoid the development of a stress concentration in the tissue layer in the vicinity of the indentor edge, when indented. Appendix A contains an analysis comparing indentation models with varying radii of curvature for the indentor tip. Results of this comparison led to the conclusion that the radius of the corner of the indentor tip should be greater than zero in order to avoid stress concentrations in the tissue, and less than or equal to the width of the outer-most element under the indentor in efforts to keep the radius of the indentor tip that

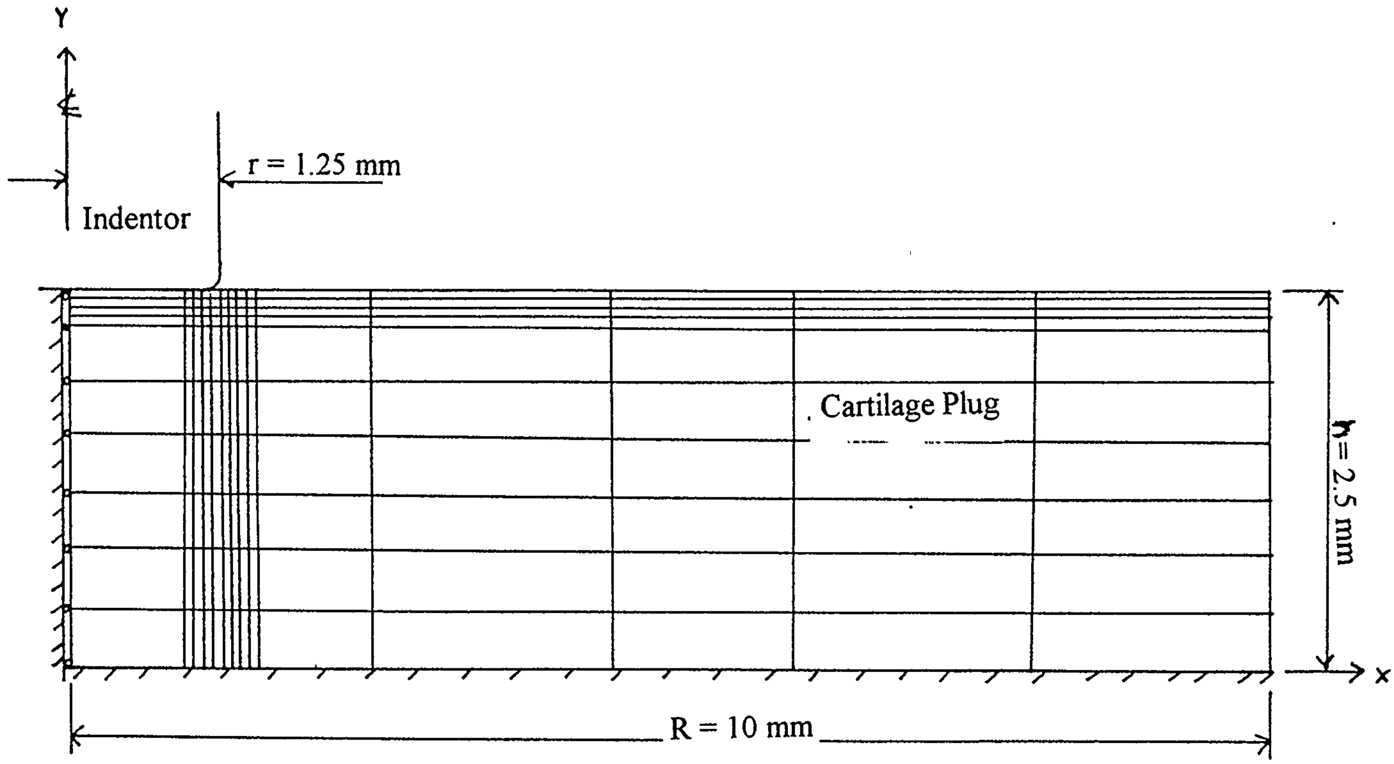

Figure 19
Finite Element Mesh for Axisymmetric Displacement-Controlled Indentation Test

indents the cartilage as close to the size of the indentor above the corner.The elements in the mesh were arranged similar to the models used by Spilker (1988) and Van der Voet (1992). The mesh was refined in the regions of the model where higher stresses were anticipated.

3.2.2 Elements

ABAQUS has several poroelastic elements available in its library. The element chosen to model the cartilage was an eight-node axisymmetric element, CAX8RP, with biquadratic displacement and bilinear pore pressure, meaning that displacements and pore pressures were active degrees of freedom at the corner nodes of the element, whereas, only the displacements were active degrees of freedom at the midside nodes of the elements.

The indentor was modelled using solid section elements and defined such that the normal to the section was pointing outward.

Interface elements, called slideline elements, INTER22A, were placed on the surface of the cartilage below the indentor in order to permit frictionless sliding between the indentor and cartilage surface, by setting the coefficient of sliding friction equal to zero.

3.2.3 Boundary Conditions

Rollers were used along the centreline of the model which allowed the cartilage to move freely in the global y-direction, but prevented radial displacements.

The base of the model was fixed in the global x and y directions to simulate the fixity of the cartilage to the underlying subchondral bone.

Two models were developed which had different boundary conditions at the indentor tip:

Model 1: sealed under the indentor, free-draining in unloaded region; simulating an impermeable indentor

Model 2: free-draining cartilage surface; simulating a permeable indentor.

The free-draining cartilage surface was modelled by setting the pore pressures on the surface of the cartilage to zero. These models were developed for comparison with Spilker et al. (1988).

3.2.4 Material Properties

The cartilage elastic and hydraulic material properties used by Spilker et al (1988) and equivalent ABAQUS input values are listed in Table 3.1. These material properties were chosen for comparison with Spilker et al. (1988). Isotropy was assumed for both the elastic and hydraulic properties.

3.2.5 Loading

A time-dependent displacement was applied to the top of the indentor, ramping linearly from u_y = 0mm at t = 0s, to u_y = −0.125mm at t=500s, and remaining constant at u_y = -125mm until t = 2000s, see Figure 20.

Table 3.1
Elastic and Hydraulic Properties

	Spilker et al (1988)	**Equivalent ABAQUS input values**
Elastic Properties	$\lambda_s = 0.1$ MPa $\mu_s = 0.2$ MPa	$E_s = 0.467$ MPa $\nu_s = 0.1667$
Hydraulic Properties	$k_\circ = 7.5 \times 10^{-15} \dfrac{mm^4}{Ns}$ $\gamma_w = 9.81 \times 10^{-6} \dfrac{N}{mm^3}$	$k = 7.358 \times 10^{-8} \dfrac{mm}{s}$
Void Ratio	$\dfrac{V_f}{V_s} = 4.0$	$\dfrac{V_f}{V_s} = 4.0$

where:

$k_\circ$ = permeability

γ_w = specific weight of pore fluid

E_s = Young's modulus

$$= \frac{\mu_s(3\lambda_s + 2\mu_s)}{\lambda_s + \mu_s}$$

μ_s = Lamé constant

ν_s = Poisson's ratio

$$= \frac{\lambda_s}{2(\lambda_s + \mu_s)}$$

k = permeability normalized by specific weight of the pore fluid (required for input into ABAQUS)

$$= \frac{k_\circ}{\gamma_w}$$

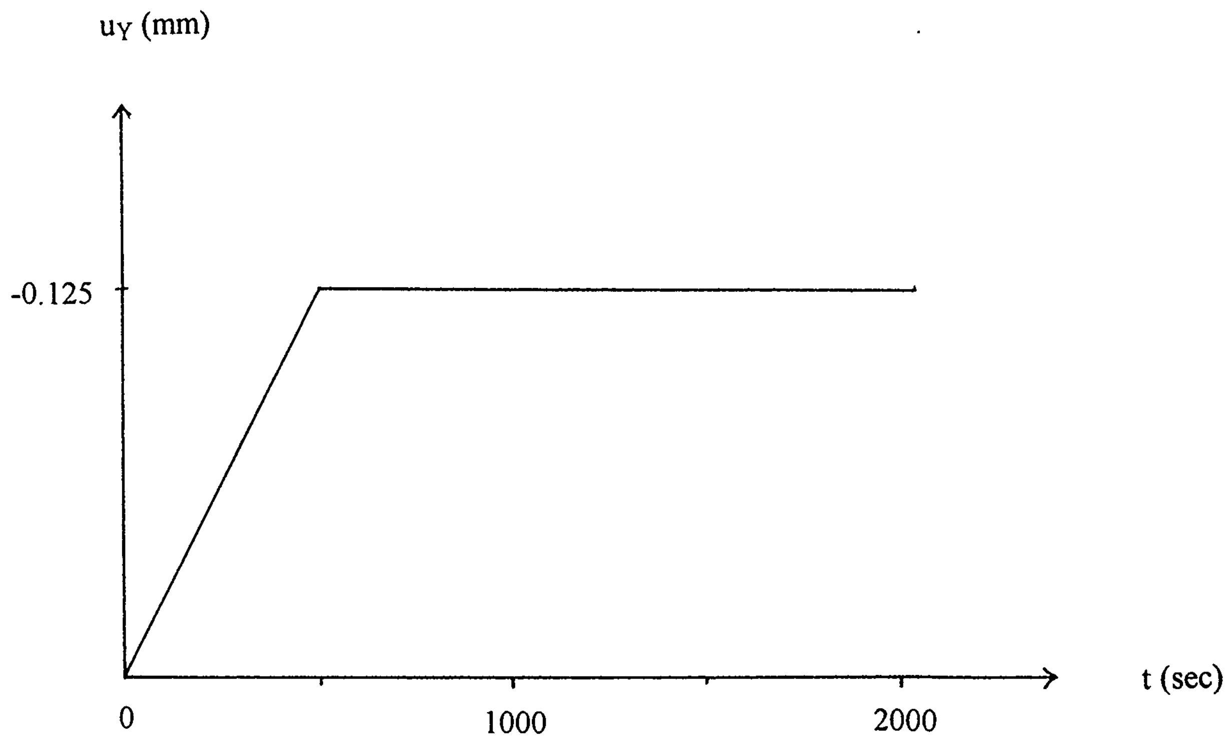

Figure 20
Time-Dependent Displacement Applied to Top of Indentor

The size of timestep to be used by ABAQUS for modelling the behaviour of cartilage was determined using Eq. 3.2 (HKS),

$$\Delta t \geq \frac{1}{6C} (\Delta h)^2 = 0.465\text{s} \qquad \text{Eq. 3.2}$$

where: $C = \frac{Ek}{\gamma_w}$

E = modulus of elasticity

k = permeability

Δh = value of smallest dimension of an element in the cartilage in the loaded region.

γ_w = specific weight of pore fluid

Time step sizes smaller than this critical value can result in instabilities within ABAQUS. The time step used in the analysis was 5s.

3.2.6 Results

The results for models 1 and 2 (Table 3.2) were compared to results from Spilker et al. (1988), and Van der Voet (1992). The results obtained using ABAQUS compared well with both researchers. The peak reaction forces are higher using ABAQUS: however, similar results were also found by Van der Voet using ABAQUS, version 4.8.5. The equilibrium reaction forces were close for the two codes. The equation derived by Hayes et al. (1972) which related the indentation force produced by an impermeable, smooth indentor to elastic properties for a thin elastic layer attached to a

Table 3.2
Reaction Force and Axial Strain Comparison to Spilker et al.(1988) and van der Voet (1992)

Model	Reaction Forces (N)						Axial Strain		
	Peak			Equilibrium					
	Present Study	Spilker	van der Voet	Present Study	Spilker	van der Voet	Present Study	Spilker	van der Voet
1	0.31	0.25	0.31	0.24	0.22	0.23	7.1E-2	7.1E-2	7.0E-2
2	0.30	n/a	0.29	0.25	n/a	0.25	6.4E-2	n/a	6.4E-2

Note:

Peak reaction forces and axial strains occur at t = 500s.

Equilibrium reaction forces are shown for t = 2000s.

Centroidal location for axial strain is at 0.08r and 0.02h below the tissue surface.

rigid backing was also used to check the solution. Substituting a dimensionless coefficient, κ, which relates the force to the layer geometry and properties, for materials with low Poisson's ratio (Jurvelin et al., 1990), into the equation derived by Hayes et al.(1972):

$$P = \frac{2aE_S w_\circ}{1 - \nu_S^2}\kappa = 0.225\text{N} \qquad \text{Eq. 3.3}$$

where: E_S = 0.467 MPa

ν_S = 0.167

$w_\circ$ = 0.125mm

κ = 1.3

The result for P of 0.225 N is very close to the solutions here and by Spilker (1989) and Van der Voet (1992) thus the solution does converge at equilibrium to the elastic solution. The centroidal strain values are the same for all three analyses, as are the trends for the stresses in each case, see Table 3.2.

3.3 Model Description - Indentor Model - Step 2

The model developed and verified in Step 1 of this analysis was modified using the preprocessor package Patran 2.5-3 (PDA Engineering). The height of the cartilage plug, h was varied, while the radius of the plug, R, the radius of the indentor, r, and the mesh were kept constant. The use of the same mesh for each model aided in the ease of use of the various models as the node and element numbering was the same from model to model.

3.3.1 Model Geometry

The height of the cartilage plug was varied from 0.75mm to 5mm, see Table 3.3, to simulate actual thicknesses of cartilage seen in the lab (rabbit cartilage ≈ 0.75mm, human cartilage ≈ 4.0mm). The radius chosen for the indentor was, r=2mm, which is a common size of indentor used in the lab. To avoid edge effects near the outer edge of the plug, the plug radius was defined as R = 20mm. Spilker et al (1992) determined that the larger of R > 4r or R > 4h was sufficient to simulate an infinite sheet of tissue in order to avoid edge effects. For simplicity, R=20mm was used for each model (models A through L). Figure 21.

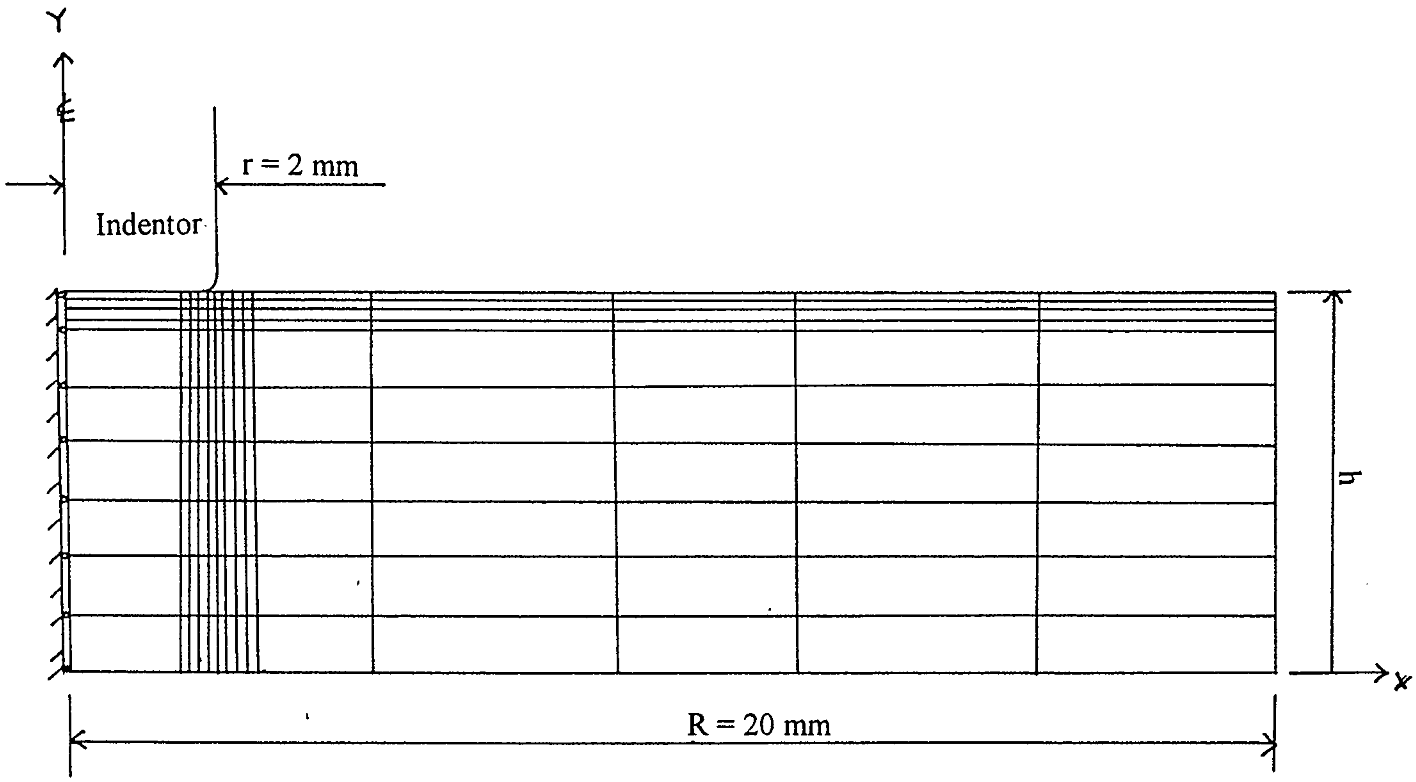

Figure 21
Finite Element Mesh For Axisymmetric Displacement - Controlled Indentation Test

Table 3.3
Height of Cartilage for Models A through L

Model	A	B	C	D	E
h(mm)	0.75	1.00	1.25	1.50	1.75
Model	F	G	H	I	J
h(mm)	2.00	2.25	2.50	2.75	3.00
Model	K	L			
h(mm)	4.00	5.00			

3.3.2 Elements

The elements used in the models were the same as those used in the original model. Eight-noded poroelastic axisymmetric elements, CAX8RP, were used to model the cartilage tissue; the indentor was modelled using a solid section; and the frictionless interface was modelled using slideline elements, INTER22A, with friction = 0.

3.3.3 Boundary Conditions

The boundary conditions used in the original model in Step 1 were used in the indentor models of the second step. The base was fixed, allowing no movement in either the global x or y-directions. Rollers were used along the centreline allowing movement in the global y-direction but preventing radial displacements.

3.3.4 Material Properties

The isotropic elastic and hydraulic material properties listed in Table 3.1 were used in each of the indentor models developed in Step 2 of the analysis.

3.3.5 Loading

A time-dependent displacement was applied to the top of the indentor ramping linearly from $u_y = 0$ at $t = 0$, to $u_y = -0.05h$ at t=500s, and remaining constant at $u_y = -0.05h$ until t=2000s, see Figure 22. This ratio was chosen in order to indent each cartilage plug to the same depth, relatively speaking.

Since the radius of the plug remained constant for each of the developed models, the critical time step was calculated, using Eq. 3.2, $\Delta t \geq 0.1190$s. However, the time step used in the analysis was the same as for step 1, $\Delta t = 5$s, for computational efficiency.

3.3.6 Results

Twelve nodes were chosen at various locations in the model and pore pressures, matrix stresses and strains, and void ratios were measured at t=500s . Table 3.4 lists the locations of the nodes which are shown on Figure 23. Three depths within the tissue were chosen within the STZ, at middepth, and deep within the tissue. Additionally, three radial locations were chosen: at the centreline of the model, mid-radius to the edge of the indentor, at the edge of the indentor, and just beyond this edge. These values were chosen for later comparison with the results from the diarthrodial joint model.

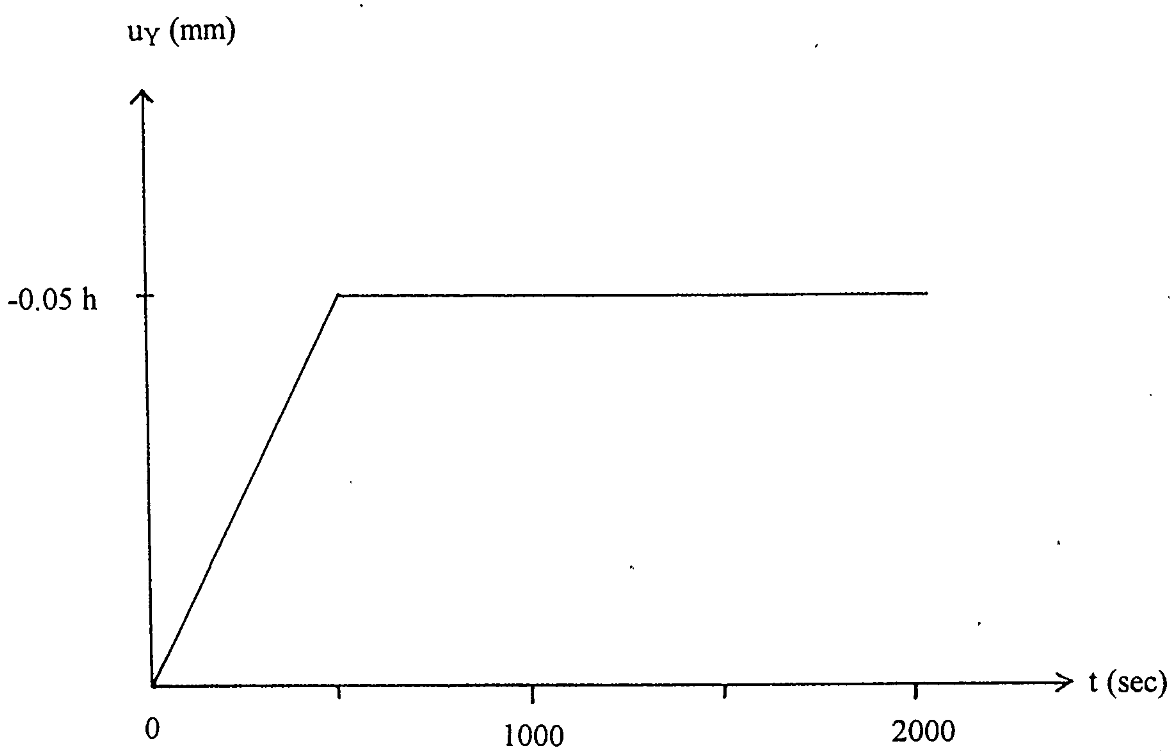

Figure 22
Time Dependent Displacement Applied to Top of Indentor

Table 3.4
Location of Nodes for Models A through L

Node	x - coordinate (measured radially outward from the centreline of the plug) (mm)	y - coordinate (measured upwards from the base of the plug) (mm)
1	0	0.2h
2	0	0.5h
3	0	0.95h
4	$\frac{r}{2}$	0.2h
5	$\frac{r}{2}$	0.5h
6	$\frac{r}{2}$	0.95h
7	r	0.2h
8	r	0.5h
9	r	0.95h
10	$\frac{5r}{4}$	0.2h
11	$\frac{5r}{4}$	0.5h
12	$\frac{5r}{4}$	0.95h

where: r = radius of indentor = 2mm

h = height of cartilage plug (varies in each model)

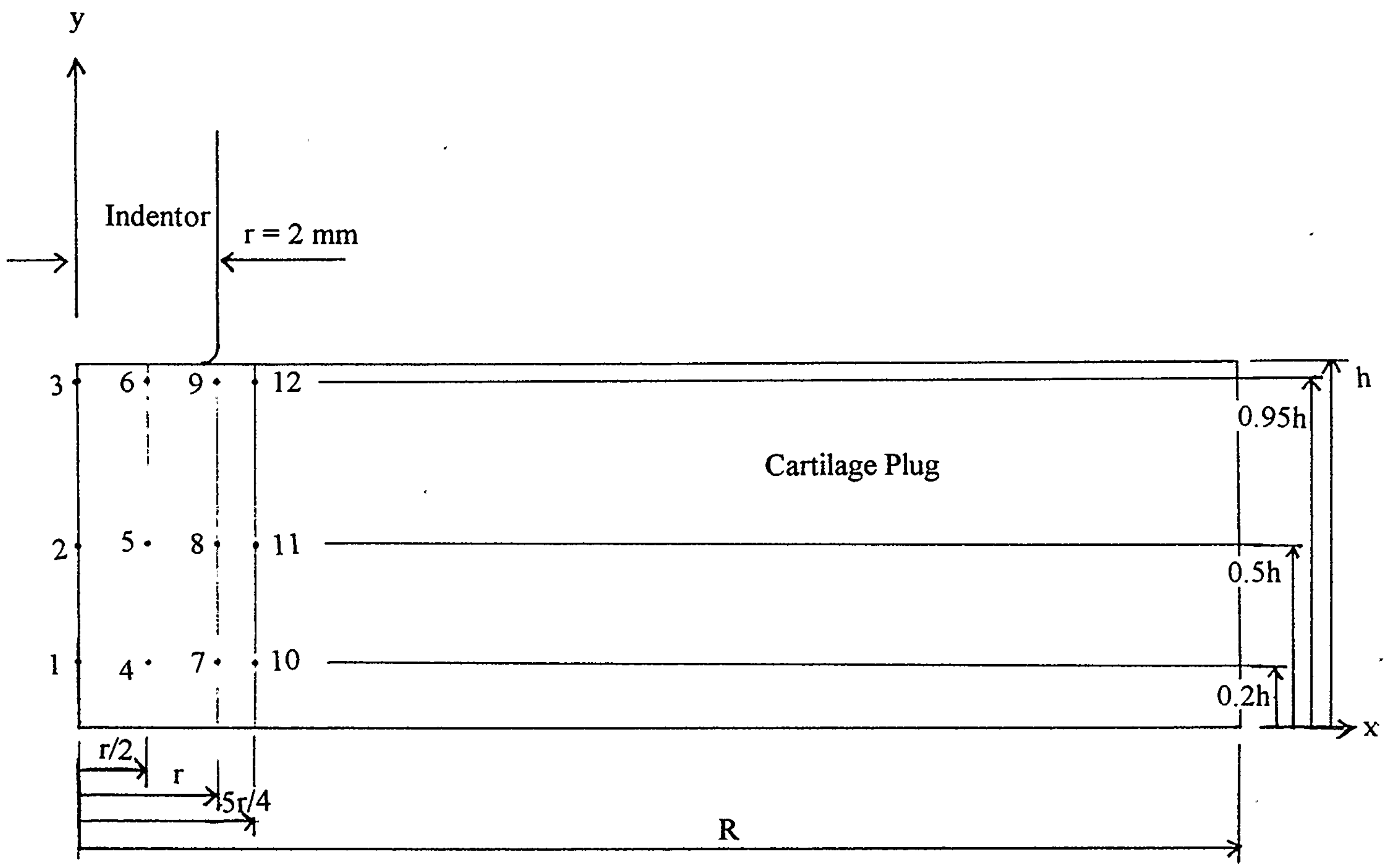

Figure 23
Location of Nodes 1 to 12 for Models A through L

The results for Models A through L, recorded in Tables B-1 through B-12, in Appendix B, were determined at t=500s. Any reference time could have been chosen at which to compare the models, however, t>500s would have resulted in comparison of the equilibrium results, with little or no pore pressure in the model. The results at t<500s would also have been sufficient, however, it was decided to make the comparison using the peak pore pressures and peak stresses i.e. at t = 500s. Results were also recorded at t = 20s. These results are found in Appendix C.

The recorded pore pressures for Models A, B, C, & D ($2.67 \geq \frac{r}{h} \geq 1.33$) were less than the vertical stresses in the loaded region of the cartilage, nodes 1 through 9. These results indicate that the tissue is loaded sufficiently slow enough that the water does not get trapped in the matrix, and is able to flow away from the loaded region of tissue under the indentor. As a consequence, the matrix of the tissue has to support the load, as is indicated by the large magnitude of vertical stress relative to pore pressure.

Models E through L ($1.14 \geq \frac{r}{h} \geq 0.4$) also display this behaviour of the tissue matrix supporting a greater load than the tissue fluid. However, these models differ from Models A to D in that the pore pressure for node 7 (and node 4 for model K) is greater than the vertical stress measured in the matrix.

The results for nodes 1 and 4, of Models E to L, in the deep region of the cartilage, under the indentor, indicate that the pore pressures and matrix stresses are closer in value than for the first four models. The water in the lower regions of the cartilage gets trapped and ends up carrying more load, and thus the magnitude of the pore pressure increases while the matrix stresses decrease as more of the load is shared between matrix and tissue fluid. The pore pressures were greater in the region just beyond the edge of the indentor nodes 10 to 12, than the matrix stresses for each of the models, as was expected. This region of tissue is not directly loaded, thus the tissue fluid is able to escape laterally as well as vertically up and out of the cartilage.

Pore pressures for Models A to L are plotted in Figures B-1 to B-12. The pressures vary laterally from smaller values in the outer radial regions of the cartilage plug to larger values at the centreline of the cartilage plug under the indentor.

Comparing the pore pressure plots for the cartilage plugs of varying heights indicates the columns of constant pore pressure under the indentor and steeper gradients towards the outer edge of the indentor for models with smaller values of h, or conversely, larger r/h values.

The results indicate that when the aspect ratio, r/h become less than r/h = 1.60, the pore pressures through the depth of the tissue are not uniform.

The results for the vertical stresses in the matrix indicate that all of the values are compressive except for the vertical stress at node 12, at the top of the cartilage, just beyond the edge of the indentor. This result was expected. As the water flows vertically in this region beyond the edge, it creates an upward drag on the matrix. The vertical stress recorded in the tissue illustrates the resistance by the matrix to the tension created by the upward drag.

The horizontal stresses recorded for nodes 1 to 12 of Model A were compressive. Similarly, the horizontal stresses for the nodes of Model B were also compressive except for node 3, which was in tension.

The horizontal stresses for the nodes of Models C and D were also compressive except for nodes 2,3,and 5.

Models E and F displayed compressive horizontal stresses at nodes 7 through 12.

Similarly, the horizontal stresses recorded for Models G and H were compressive horizontal stresses at all nodes excluding nodes 1 through 5.

Models I, J, K, L displayed compressive horizontal stresses at nodes 9 through 12.

Tensile horizontal stresses in the matrix indicate a lateral movement of fluid in the matrix as the water attempts to move away from the loaded region. The results seem to indicate that as the dimension 'h' becomes larger with respect to the indentor radius, or conversely, as the r/h ratio becomes smaller, more of the cartilage matrix experiences lateral fluid flow. Since the cartilage plugs are loaded to the same depth relatively (u_Z /h = -0.05), models with smaller aspect ratios, r/h, or conversely, larger h dimensions relative to the constant dimension of the radius, experience more tissue fluid lateral movement than larger r/h models.

The initial void ratio (volume of voids/volume of solids) input into the finite element model of cartilage was 4.00. The loaded region of cartilage (nodes 1 to 9) at t=500s, had void ratios<4.0 meaning that the volume of voids decreased and/or the volume of solids increased. When a soil layer is loaded, compression of the layer occurs because of:

1) deformation of soil grains

2) compression of air and water in the voids and/or

3) squeezing out of water and air from the voids.

Compression of the soils grains is usually small, therefore neglected. Similarly, the soil is usually assumed to be 100% saturated for settlement problems, thus compression of pore fluid is also neglected. Therefore, in soils, water and air squeezing out of the voids usually has the largest influence on the degree to which a soil layer compresses (Holtz and Kovacs, 1981). The void ratio results computed in the models illustrate that this type of behaviour is also present in the indentation tissue. The gradient of void ratios, laterally and vertically within the tissue varied with the r/h ratio of the model.

The void ratios recorded for Models A, B, and C decreased in value, vertically, from the superficial zone to the deeper regions at nodes 1,2,3 and nodes 4,5,6. This trend reversed at nodes 7,8,9, with the ratio increasing with depth.

Similar results were recorded in Models D, E, and F, however, for model D, nodes 4,5,6 under the indentor, the void ratio increased with depth until the middle zone, then decreased to the deeper zone. A similar trend occurred in Models E and F, however, at the centreline (nodes 1,2,3).

The results for Models G through L indicate that the void ratios increased with depth from the superficial zone of the cartilage for the nodes under the indentor (nodes 1 through 9).

The results for nodes 10,11,12 for models A through L indicate that the void ratio decreased from the superficial zone of the cartilage to the middle depth, then increased to the deeper zone. The values of the ratios were all less than 4.0 for these nodes, except for node 12 of Models F through I, which were greater than 4.0, indicating an increase in the volume of the voids and/or decrease in the volume of the solids from the original unloaded model. Since the volume of the solid, or the matrix, did not decrease, this result indicates an increase in volume of voids, or fluid moving into the voids of this region of the cartilage plug. The magnitude of the void ratio for node 12, in the remaining models (Models J through L) was, although less than 4.0, close in magnitude to 4.0.

These void ratios, indicate that fluid escapes from the voids as the tissue is indented. The magnitude, or rate at which the fluid flowed varied with the models as explained above. The amount of fluid flowing from the pores from the models with larger r/h ratios seemed to generally increase with depth from the surface, thus more fluid flow occurred deeper in the tissue beneath the indentor. Conversely, with smaller r/h ratios, more fluid flow occurred in the superficial region of the cartilage relative to the deeper regions.

The use of a sealed hydraulic boundary condition is validated by these results. The decrease in void ratio under the indentor indicates a decrease in permeability in the tissue in this region, thus, no fluid flow in this region. This behaviour coupled with the columns of pore pressure through the depth of the tisse, indicating no vertical movement of fluid, validates the use of a sealed boundary condition since the tissue essentially seals itself.

3.4 Model Description - Indentor Model - Step Three

Model B from step two was used in this analysis to determine the sensitivity of the model to the rate at which the tissue was indented. All dimensions, boundary conditions, material properties were kept constant while two additional indentor displacement rates were tested:

2.5E-04mm/s equivalent to linear ramping to $u_y = -0.125$mm at t=500s

5.0E-04mm/s equivalent to linear ramping to $u_y = -0.125$mm at t=250s

2.5E-02mm/s equivalent to linear ramping to $u_y = -0.125$mm at t=5s

3.4.1 Results

The results for the pore pressures, Figures D-1 to D-3 found in Appendix D, indicate the substantial effect that loading rate has on the reaction force . The stresses, recorded in the matrix of the tissue are higher for models loaded at a slower rate. Conversely, the pore pressures for the faster loading rate were found to be higher than the more slowly loaded case. The water which is trapped in the tissue, under rapid loading, is unable to flow away from the loaded region because of the low permeability. The majority of the load is therefore resisted by this water and as a result, the tissue takes on the characteristics of water under compression.

The pore pressures for the first two models, t=250s and t=500s, are fairly uniform throughout the depth of the tissue until the edge of the indentor, where the gradient steepens, whereas the pore pressures are not uniform for the fastest loading case. Thus, care must be taken to ensure that the tissue is not loaded too quickly, in order to prevent behaviour in the tissue which is uncertain numerically.

4.0 Finite Element Model of a Diarthrodial Joint

A finite element model of a diarthrodial joint was developed using ABAQUS to simulate a stress-relaxation test. The cartilage layers were modelled as a poroelastic material using soil consolidation (Biot) theory. The purpose of this study is to compare the results of this model, where the indentor is another non-planar surface, with the results from the unconfined time-dependent model, in which the indentor geometry was flat and indentor material properties were dissimilar to the articular cartilage, to observe where within the contact zone of the joint model the results compare.

4.1 Joint Model Description

4.1.1 Joint Model Geometry

A plane-strain finite element model was developed which consisted of two apposing incongruous cartilage layers rigidly attached to underlying bone. The two cartilage layers were modelled with differing radii of curvature, forming an incongruous fitting joint. The geometric parameters used in this model closely resemble those by Van der Voet (1992) and are not necessarily representative of a specific joint within the body. Symmetry of the joint was used to simplify the model: the joint was subjected to concentric axial compressive loading and only half of the joint was modelled (Figure 24). The upper surface was modelled with a slightly convex geometry with a half-width of 12.275mm, see Figure 24. The cartilage layer was 1mm thick across the joint surface except towards the

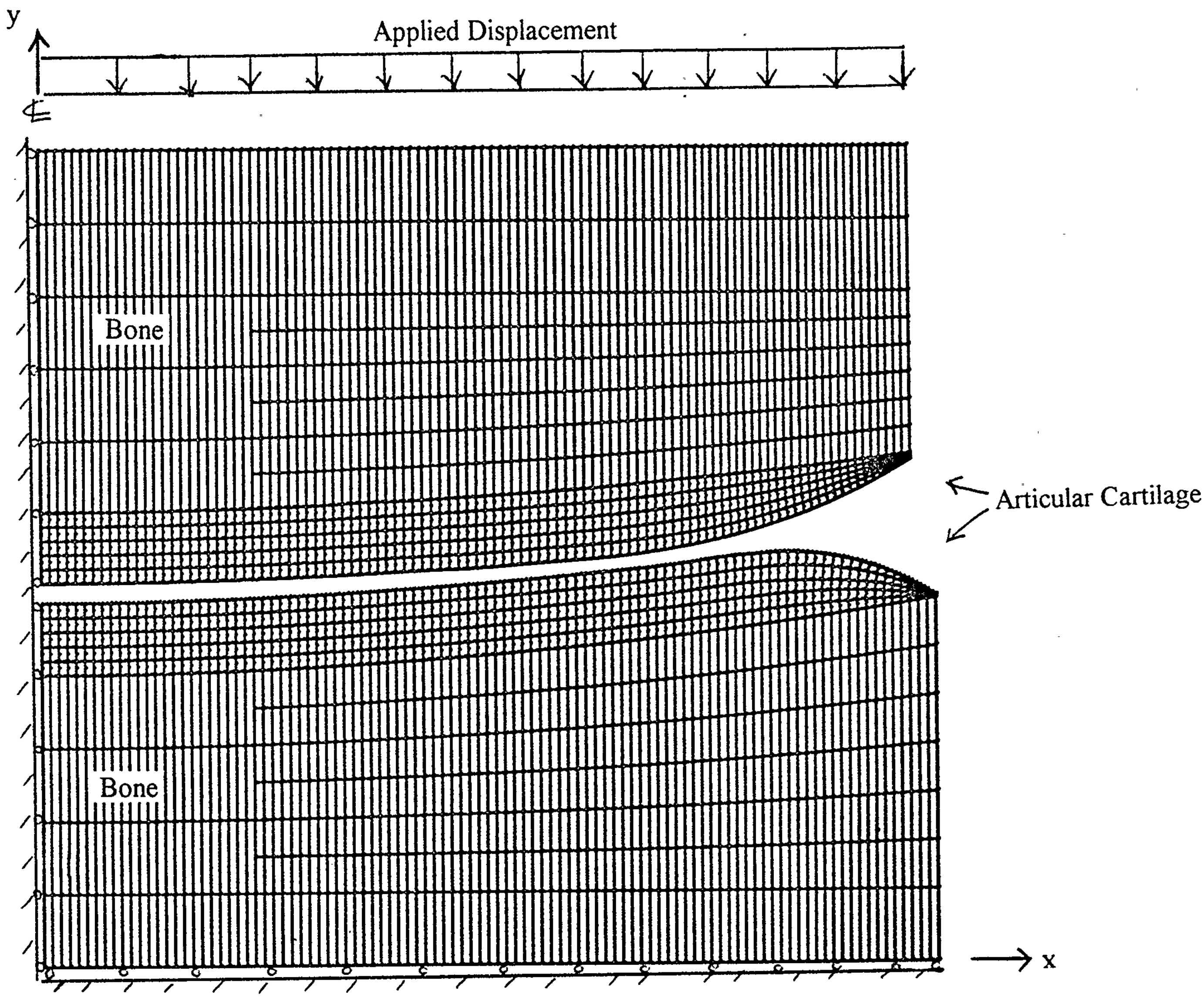

Figure 24
Finite Element Mesh used to Model the Stress Relaxation Test on a Diarthrodial Joint

outer regions of the joint where the layer tapered toward the underlying bone. The depth of the bone at the centreline was 4mm.

The lower joint was modelled with a slightly concave curvature and a half-width of 12.625mm. Similarly, the cartilage layer was 1 mm thick across the joint until near the outer region of the cartilage where it also tapered toward the underlying bone. The depth of the bone at the centreline was 4 mm.

The models were developed using the pre/post-processor package PATRAN. Five models were developed with the radius of upper surface varied, see Table 4.1.

Table 4.1
Radii of Curvature for Upper and Lower Cartilage Surfaces for Models M through Q

Model	Upper Radius (mm)	Lower Radius (mm)
M	100	80
N	110	80
O	125	80
P	90	80
Q*	100	80

* Note: Model Q differs from Model M in permeability

4.1.2 Elements

The cartilage was modelled using eight-node poroelastic elements (CPE8RP). The bone was modelled using four-node isoparametric displacement elements (CPE4).

The cartilage/cartilage interface was modelled using slideline elements which allowed for the contacting surfaces to slide past each other. Slidelines are composed of a 'slave' and a 'master' surface. In the model, the upper surface was modelled as the 'slave' surface and defined by slide line elements. The lower surface then became the 'master' surface defined by the nodes along the lower surface of the lower cartilage layer.

A smoothing option is available in ABAQUS which is used to smooth the slope at common nodes on adjacent elements to define a smooth surface and prevent oscillating, non-convergent solutions. ABAQUS does this by determining constraint equations for each node of the slideline element and then adding these equations to the global stiffness matrix of the structure. The programme estimates the state of contact and then iterates the initial attempt at solving the system of equations, and compares the solution to the initial estimate. Iterations are performed until the specified force residual for equilibrium is achieved (in this case parabolic type contact was chosen for the nodes along the surfaces of the cartilage).

The coefficient of friction was set to zero, simulating a frictionless interface between the two apposing cartilage surfaces.

4.1.3 Boundary Conditions

4.1.3.1 Kinematic Boundary Conditions

Rollers were used along the centreline of the model allowing movement in the global y-direction but preventing movement in the radial-direction. The base and the top of the bone on the upper joint were also modelled using rollers. However, the model was free to move in the radial-direction and prevented from moving in the global y-direction.

Multi-point constraints were used in the model allowing mesh refinement between adjacent quadratic elements in the bone mesh.

4.1.3.2 Hydraulic Boundary

The surface of the cartilage was modelled as sealed in the contact zone and free-draining in the non-contacting zone. Prior to the first iteration, an estimate was made as to which nodes along the cartilage surface would be in contact. The pore pressures of the remaining nodes were set to zero, to simulate a free-draining surface, where pore pressure does not build up. The iteration was then performed and the contacting nodes were compared to the initial estimate and then the hydraulic conditions were adjusted as necessary. Iterations were performed until the estimate coincided with the results of the step. This procedure was performed during the loading phase of the model. Once the relaxation phase was reached, the hydraulic boundary conditions were no longer altered, but rather, the conditions for the current step were based on the previous iteration

4.1.4 Material Properties

The material properties used in this analysis were the same as those used by Van der Voet (1992) and are similar to those used by Spilker et al. (1988).

The articular cartilage layer was modelled as a poroelastic material with isotropic elastic and hydraulic properties.

Table 4.2
Cartilage Material Properties for Models M through Q

Elastic Properties	$E_s = 0.467$ MPa $\nu_s = 0.1667$
Hydraulic Permeability	$k = 7.358\text{x}10^{-8} \dfrac{mm}{s}$ $\gamma_w = 9.81 \dfrac{kN}{m^3}$
Void Ratio	$\dfrac{V_f}{V_s} = 4.0$

Note: Model Q was modelled with k=7.358E-9mm/s

The bone was modelled as a homogeneous isotropic linear elastic solid.

Table 4.3
Bone Material Properties for Models M through Q

Elastic Properties	$E_s = 500$ MPa $\nu_s = 0.30$

4.1.5 Loading

A ramp displacement was applied to the top of the upper joint until only a small gap (0.02mm) existed between the two apposing layers at the joint centreline. The displacement rate used in this model was the same as that used by van der Voet (1992), 1.333 x 10^{-2}mm/s . The displacement then remained constant until static equilibrium was reached between the pore fluid and matrix solid, approximately t=2000s.

In order to avoid numerical instabilities and the program stopping, a small gap was necessary between the two apposing surfaces at the centreline. This gap was obtained by controlling the displacemen of the upper surface relative to the lower surface. The need for this gap may arise from pore fluid initially flowing toward the gap opening, away from the contacting surface and no longer having an outlet at the centreline, leaving only one outlet on the other side of the contacting zone.

Convergence of the solution during the consolidation process was checked using an elastic model. The same model was used, but continuum elastic solid elements (CPE8R) were used in place of poroelastic elements to represent the cartilage layer.

4.1.6 Results

Fifteen nodes provided in Table 4.4, and Figure 25. were chosen at various locations in the tissue and a number of parameters were measured at the onset of stress relaxation. These locations were chosen to correspond with the locations of the nodes in Step 2 of the indentor model analysis (found in Table 3.4). Due to changing geometry, the contact zone width differed for each model, thus the node locations changed in each model.

The results for Models M through Q are recorded in Tables 4.5 to 4.9 and Figures 26 to 29 at the end of this section.

Table 4.4
Location of Nodes for Models M through Q

Node	x-coordinate (measured outward from the centreline of the contact zone)	y-coordinate (measured globally upward from the base of the cartilage layer)
1	-5r/4	0.2h
2	-5r/4	0.5h
3	-5r/4	0.95h
4	-r/2	0.2h
5	-r/2	0.5h
6	-r/2	0.95h
7	0	0.2h
8	0	0.5h
9	0	0.95h
10	r/2	0.2h
11	r/2	0.5h
12	r/2	0.95h
13	5r/4	0.2h
14	5r/4	0.5h
15	5r/4	0.95h

where: h = height of cartilage

r = radius of contact zone

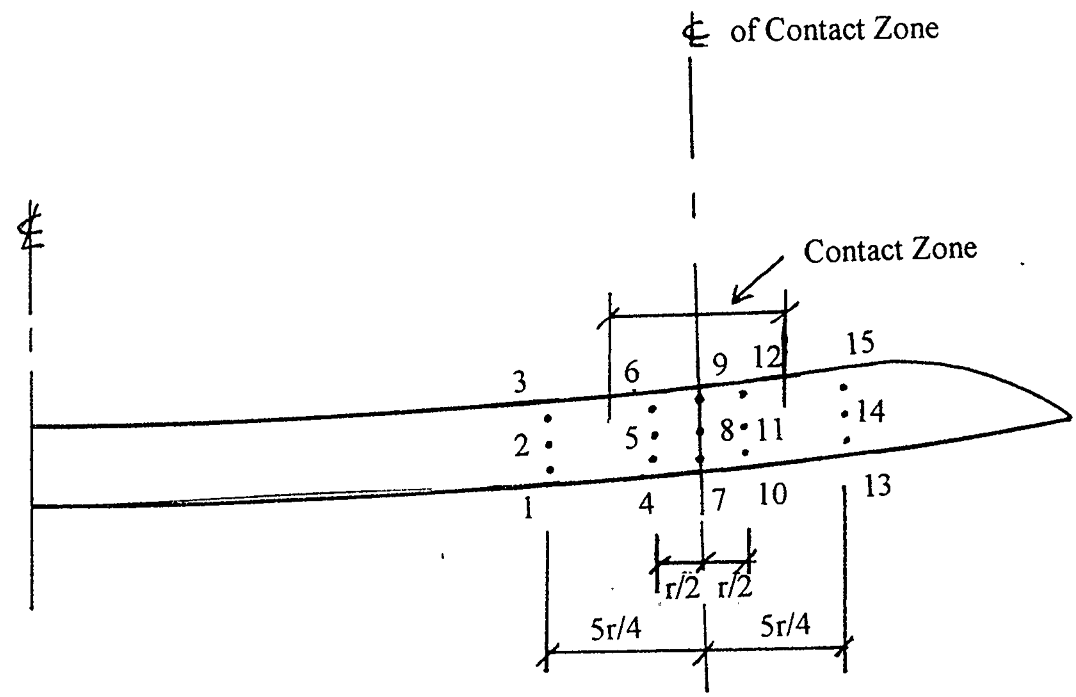

Figure 25
Location of Nodes on Lower Cartilage Layer for Models M through Q

The results of Model M were compared to the full joint model of Van der Voet (1992). The pore pressures, although similar in gradation to the pore pressures produced byVan der Voet, differed in magnitude by approximately 15%. The pore pressures were found to be uniform throughout the depth of the tissue, at any radial location within the tissue, similar to Van der Voet's results.

The version of ABAQUS used by Van der Voet (1992) (version 4.8.5) was an earlier version than used in this analysis (version 5.4). Support staff for ABAQUS indicated that many feature of the programme are now automated compared to the earlier version in which tolerances were input by the user. Results differing by at least 10% between the two versions are not uncommon, according to the staff. This fact in addition to the slight difference in geometry of the two apposing surfaces, leading to different contact widths (Van der Voet's contact zone width is greater than the width obtained in this study), are thought to account for the differences between the models. Thus the present model was used throughout the remainder of the analysis.

Tissue permeability was altered in the analysis in Model Q to determine the effect of this parameter on the model. The original value of 7.358E-08 mm/s was changed to 7.358E–09 mm/s and the results were compared. The effect of altering the permeability by a factor of 10 resulted in a slight increase in the horizontal and vertical stresses, reaction force, and the pore pressures, however, this increase was not too significant, see Table 4.9 a,b.

The vertical stresses recorded for Models M and N, although differing in magnitude, were similar in their compressive and tensile characteristics.

The vertical stresses along the centreline of the contact zone were compressive, as were nodes 4, 10, 11 in Model M, and nodes 10, 11, 12 in Model N and O. The remaining nodes in both models displayed vertical stresses which were in tension. Model P differed slightly from Models M and N, with the vertical stresses at nodes 4 through 12 compressive, and the remaining stresses in tension.

These results indicate the upward movement of water in the region of cartilage beyond the edge of the contact zone (nodes 1, 2, 3, 13, 14, 15), creating an upward drag on the matrix as the tissue attempts to pull away from the underlying subchondral bone. Similar results were seen in the contact zone for nodes 4, 5, 6 (excluding nodes 4 for Model M), thus the upward movement of water. Model P displayed less vertical movement of water than Models M and N; vertical movement of water only at the nodes beyond the contact zone. The contact zone in Model O was large enough that no results were obtained for nodes 1-3 and 13-15.

The horizontal stresses recorded for Models M, N, O, and P were also very similar in terms of their compressive and tensile natures.

The horizontal stresses measured at nodes 7, 8, 9 and 10, 11, 12 for Models M, N, O, and P (excluding node 12 for Model M) were in tension. The remaining nodes for both models (excluding node 5 for Model O) displayed compressive horizontal stresses. In these regions, no lateral movement of water occurred.

Thus it appears that in the full joint models, lateral movement of water away from the centreline regions of the contact zone occurs, with vertical movement of this fluid, toward the surface, near the outer edges of the contact zone, and beyond.

The pore pressures in Models M, N, O, and P were generally significantly larger than the vertical stresses recorded for the matrix at the same locations (excluding node 3 for Model N, node 12 for Model O, node 14 & 15 for Model P, and nodes 13, 14, & 15 for Model M). In these locations, the load is carried by the trapped tissue fluid.

The pore pressure plots of Figures 26 to 29 indicate the decrease in contact zone width as the radius of curvature of the upper surface decreases.

The magnitudes of the pore pressures significantly increase as the upper radius increases, or the surface flattens out.

The pore pressure gradient is steeper towards the outer edge of the cartilage layer, away from the centreline of the tissue.

The pore pressures are more uniform throughout the tissue thickness as the upper radius increases relative to the lower radius. Conversely, Model P has pore pressures which vary greatly with depth in the tissue.

These results indicate that as the radius of the upper articular joint surface increases relative to the radius of the lower joint, and therefore, the contact zone size increases, the magnitudes of the pore pressures similarly increase quite significantly. The increase in pore pressure indicates that the tissue fluid, as opposed to the tissue matrix, supports the majority of the load under these loading conditions. It appears that as the contact size increases, the water is unable to move laterally away from the contact zone. This behaviour is illustrated in the results. The magnitudes of the horizontal stresses decrease as the pore pressure increases, indicating less lateral tension on the matrix due to the lateral fluid movement.

The void ratios of the regions of tissue surrounding the centreline of the contact zone for Models M and N indicate that as the tissue compressed, some tissue fluid was squeezed out of the pores (void ratio = volume of voids/volume of solids). This result was displayed by the magnitudes of the void ratios in this region decreasing from the initial input value of 4.0. The void ratios of the outer regions of cartilage, beyond the contact region, either remained constant, or increased, as seen in the outer-most region of Model N. This increase implies a movement of tissue fluid into the region. This result was expected since the only route of escape for the fluid was laterally, away from the centreline, and up out of the cartilage.

The contact zone width increased as the upper radius increased in magnitude, relative to the lower layer. This result was expected since the outer regions of the cartilage layers make contact first as the two apposing surfaces are compressed together. Increasing the upper radius flattens this layer relative to the lower surface, thus bringing the two surfaces closer together prior to contact.

The vertical stresses decreased, whereas the pore pressures increased, with an increase in upper surface radius, thus, and increase in the contact surface width. Greenwald et al. (1971) analyzed the transmission of load through the human hip joint, as mentioned earlier, and determined that the location and magnitude of the contact area between the articular surfaces in the hip joint depended on the magnitude and direction of the applied load. The authors concluded that the function of this incongruity was to allow the articular surfaces to transmit large pressures when heavily loaded, and to come out of contact during lighter loading for lubrication and nutritional purposes with the synovial fluid.

The void ratios of the nodes under the contact zone decreased from the initial input value of 4.0 for the full joint models. This decrease in void ratio indicates a decrease in permeability, thus indicating no fluid flow under within the cartilage under the contact zone. This behaviour coupled with the columns of pore pressure through the depth of the tissue in the contact zone (no vertical movement of fluid), indicates that the tissue essentially seals itself. Thus the use of a sealed hydraulic boundary condition within the contact zone width seem valid.

The present study altered the geometry of the upper radius of curvature in the joint, which affected the size of the contact area width. However, the fluctuating contact area width between the two apposing surface in the diarthrodial joint model presented in this study could perhaps be controlled by the magnitude and direction of the applied load.

A further model could be established in which the results are adjusted to correlate with the same load. Since the contact pore pressures of this model increased significantly with an increase in contact zone width, and an increase in incongruity between the upper and lower surface, a model developed to load joints of differing degrees of incongruity with the same magnitude of load, would possibly produce low pore pressures for models with more congruous surfaces, and higher pore pressures for models with less incongruous surfaces.

During the present study, a range of upper surface radii of curvatures were studied, ranging from 50mm to 150mm. When the upper radius was less than the lower radius; the two surfaces did not contact for the displacement applied to the upper surface. This result is plausible when the geometry of the model during joint loading is considered. The outer regions contact first, followed by the regions toward the centreline of the model. However, with smaller upper radii, the surface slopes upward quickly, and given the 0.02mm gap maintained at the joint centreline, the two surfaces do not contact.

Similary, when the upper radius was increased up to 150mm, the upper surface became too flat relative to the lower surface, and the models continually stopped during the ABAQUS analysis. Thus the lower and upper bounds for this model for the upper radius of curvature were found to the extremes listed in this analysis, 90mm to 125mm, or R(upper)/R(lower) = 1.125 to 1.5625.

Model M

R upper= 100.00 mm

R lower= 80.00 mm **Permeability= 7.358E-08**

Note: '-' implies compressive; Stresses & Pore Pressures are measured in MPa

Node	Vertical Stress	Horizontal Stress	Shear Stress	Max Principal Stress	Min Principal Stress	Pore Pressure
1	1.0382E-03	-1.0067E-03	-2.5386E-03	2.7525E-03	-2.7210E-03	1.9146E-03
2	1.8860E-03	-1.8964E-03	-1.9667E-03	-2.7337E-03	2.7233E-03	2.3349E-03
3	2.9470E-03	-2.7504E-03	-5.7760E-04	3.0050E-03	-2.8084E-03	2.9823E-03
4	-5.0411E-04	5.2909E-04	-9.4294E-03	9.4560E-03	-9.4311E-03	2.5153E-02
5	7.6767E-05	-8.7903E-05	-7.1892E-03	-2.4456E-03	2.4344E-03	2.5439E-02
6	4.9001E-04	-9.6951E-04	-2.4386E-03	-7.5424E-03	7.0629E-03	2.5413E-02
7	-3.6035E-03	3.5361E-03	-7.2661E-03	-6.2935E-03	6.2261E-03	5.1822E-02
8	-5.0347E-03	5.0622E-03	-5.1422E-03	5.1859E-03	-5.1584E-03	5.1384E-02
9	-6.9010E-03	6.4721E-03	-1.1245E-03	-8.5728E-03	8.1439E-03	5.1822E-02
10	-4.4172E-03	3.8325E-03	5.0151E-03	-6.4035E-03	5.8188E-03	6.1065E-02
11	-7.6984E-03	7.4438E-03	4.5091E-03	-1.1205E-02	1.0950E-02	5.9785E-02
12	9.1204E-03	-9.1597E-03	8.0861E-03	-1.1876E-02	1.1837E-02	1.3191E-02
13	6.0357E-03	-5.8811E-03	7.5525E-03	7.6599E-03	-7.5053E-03	5.6863E-03
14	7.2289E-03	-7.2821E-03	4.6897E-03	-7.2946E-03	7.2414E-03	6.3070E-03
15	6.1881E-03	-6.4405E-03	4.2564E-04	-6.4548E-03	6.2024E-03	5.7051E-03

Table 4.5(a)

Model M - Matrix Stresses and Pore Pressures

Node	Vertical Strain	Horizontal Strain	Shear Strain	Max Principal Strain	Min Principal Strain	Void Ratio
1	2.5805E-03	-2.5281E-03	-1.2684E-02	6.8633E-03	-6.8109E-03	4.000
2	4.7162E-03	-4.7334E-03	-9.8268E-03	-6.8251E-03	6.8079E-03	4.000
3	7.2803E-03	-6.9532E-03	-2.8860E-03	7.6108E-03	9.8086E-04	4.002
4	-1.2698E-03	1.3114E-03	-4.7115E-02	-2.4306E-02	2.2821E-02	4.000
5	1.9642E-04	-2.1497E-04	-3.5922E-02	-1.9015E-02	1.6989E-02	4.000
6	1.4239E-03	-2.2224E-03	-1.2185E-02	-1.9949E-03	1.2281E-02	3.996
7	-1.9745E-03	8.8623E-03	-3.6305E-02	2.4897E-02	-1.4237E-02	3.999
8	-1.2589E-02	1.2635E-02	-2.5693E-02	2.1228E-02	-1.7469E-02	4.000
9	-1.7062E-02	1.6348E-02	-5.6185E-03	-1.7352E-02	1.0109E-02	3.996
10	-1.0792E-02	9.8182E-03	2.5058E-02	2.3307E-02	-1.5396E-02	3.995
11	-1.9127E-02	1.8703E-02	2.2530E-02	-3.2416E-02	-9.5778E-03	3.998
12	2.2802E-02	-2.2867E-02	4.0403E-02	3.1605E-02	-2.3560E-02	4.001
13	1.5015E-02	-1.4757E-02	3.7737E-02	-2.6705E-02	2.3549E-02	4.001
14	1.8082E-02	-1.8171E-02	2.3432E-02	2.1722E-02	-1.9625E-02	4.000
15	1.5565E-02	-1.5985E-02	2.1267E-03	-1.6021E-02	1.5601E-02	3.998

Model M

R upper= **100.00** **mm**

R lower= **80.00** **mm** **Permeability=** **7.358E-08**

Note: '-' implies compressive; Stresses & Pore Pressures are measured in MPa

Table 4.5(b)

Model M - Matrix Strains and Void Ratios

Model N

R upper= 110.00 mm

R lower= 80.00 mm Permeability= 7.358E-08

Note: '-' implies compressive; Stresses & Pore Pressures are measured in MPa

Node	Vertical Stress	Horizontal Stress	Shear Stress	Max Principal Stress	Min Principal Stress	Pore Pressure
1	1.4149E-03	-1.3629E-03	-6.5455E-04	1.5614E-03	-1.5094E-03	1.6658E-03
2	2.3620E-03	-2.3793E-03	-2.7716E-04	-2.3954E-03	2.3781E-03	2.2102E-03
3	3.2492E-03	-3.0947E-03	1.4002E-04	3.2523E-03	-3.0978E-03	3.1736E-03
4	1.9666E-04	-5.4794E-05	-1.4342E-02	1.4413E-02	-1.4272E-02	3.7631E-02
5	1.3271E-03	-1.4453E-03	-1.1149E-02	-5.4272E-03	5.3090E-03	3.8094E-02
6	1.3073E-03	-3.3074E-03	-5.1860E-03	-1.6140E-02	1.4140E-02	3.7396E-02
7	-3.2151E-03	3.7195E-03	-1.4963E-02	1.2120E-02	-1.1616E-02	8.8477E-02
8	-4.0673E-03	4.2544E-03	-1.1350E-02	5.8083E-03	-5.6212E-03	8.7916E-02
9	-4.8006E-03	4.6219E-03	-3.9174E-03	-5.7595E-03	5.5808E-03	8.7594E-02
10	-7.7142E-03	5.8979E-03	3.1552E-03	-8.4114E-03	6.5951E-03	1.1990E-01
11	-1.1939E-02	1.1315E-02	3.1586E-03	-1.1976E-02	1.1352E-02	1.1820E-01
12	-1.7197E-02	1.7051E-02	9.2930E-04	-3.4868E-02	3.4722E-02	1.1630E-01
13	1.5625E-02	-1.3677E-02	3.0290E-02	2.9087E-02	-2.7139E-02	3.9746E-02
14	1.7190E-02	-1.6133E-02	2.3994E-02	2.0122E-02	-1.9065E-02	3.7957E-02
15	2.2113E-02	-1.8831E-02	1.0311E-02	2.4563E-02	-2.1281E-02	2.7589E-02

Table 4.6(a)

Model N - Matrix Stresses and Pore Pressures

Node	Vertical Strain	Horizontal Strain	Shear Strain	Max Principal Strain	Min Principal Strain	Void Ratio
1	3.5133E-03	-3.4266E-03	-3.2705E-03	3.8793E-03	-3.7926E-03	4.000
2	5.9083E-03	-5.9370E-03	-1.3848E-03	5.9486E-03	-5.9773E-03	4.000
3	8.0532E-03	-7.7958E-03	6.9964E-04	8.0609E-03	-7.8035E-03	4.001
4	4.3224E-03	-1.9597E-04	-7.1661E-02	3.7965E-02	-3.3838E-02	4.001
5	3.3647E-03	-3.5615E-03	-5.5705E-02	-2.8165E-02	2.7969E-02	3.999
6	4.0990E-03	-7.4300E-03	-2.5912E-02	-1.5846E-02	1.2515E-02	3.983
7	-8.2423E-03	9.0823E-03	-7.4763E-02	3.8792E-02	-3.7952E-02	4.004
8	-1.0239E-02	1.0551E-02	-5.6711E-02	3.0357E-02	-3.0045E-02	4.002
9	-1.1919E-02	1.1621E-02	-1.9573E-02	-1.5456E-02	1.5158E-02	3.999
10	-1.8516E-02	1.5491E-02	1.5665E-02	-2.0233E-02	1.7208E-02	3.985
11	-2.9567E-02	2.8528E-02	1.5782E-02	-3.0620E-02	2.9581E-02	3.995
12	-4.2903E-02	4.2659E-02	5.4410E-03	-4.2989E-02	4.2745E-02	3.999
13	3.8224E-02	-3.4979E-02	1.5130E-01	8.5662E-02	-8.2417E-02	4.015
14	4.2505E-02	-4.0745E-02	1.1990E-01	7.3864E-02	-7.2104E-02	4.009
15	5.3877E-02	-4.8412E-02	5.1519E-02	5.9998E-02	-5.4533E-02	4.027

Model N

R upper= 110.00 mm

R lower= 80.00 mm **Permeability= 7.358E-08**

Note: '-' implies compressive; Stresses & Pore Pressures are measured in MPa

Table 4.6(b)

Model N - Matrix Strains and Void Ratios

Model O

R upper= 125.00 mm

R lower= 80.00 mm **Permeability= 7.358E-08**

Note: '-' implies compressive; Stresses & Pore Pressures are measured in MPa

Node	Vertical Stress	Horizontal Stress	Shear Stress	Max Principal Stress	Min Principal Stress	Pore Pressure
1						
2						
3						
4	1.6416E-03	-1.3787E-03	-1.5501E-02	1.5706E-02	-1.5443E-02	4.9597E-02
5	3.3599E-03	-3.5798E-03	-1.2008E-02	-5.7878E-03	5.5679E-03	5.0255E-02
6	3.9384E-03	-6.5377E-03	-4.4942E-03	-2.4083E-02	2.1484E-02	4.9376E-02
7	-3.2167E-03	3.8264E-03	-2.2173E-02	1.7810E-02	-1.7200E-02	1.2310E-01
8	-3.5412E-03	3.7691E-03	-1.7147E-02	7.4878E-03	-7.2599E-03	1.2280E-01
9	-3.4395E-03	3.2431E-03	-6.4042E-03	-3.4898E-03	3.2934E-03	1.2290E-01
10	-9.8029E-03	7.4569E-03	-5.8216E-04	-9.8088E-03	7.4628E-03	1.8070E-01
11	-1.4352E-02	1.3580E-02	3.2013E-04	-1.4370E-02	1.3598E-02	1.7900E-01
12	-1.9948E-02	2.0110E-02	-7.0083E-04	2.0110E-02	-1.9948E-02	1.7660E-01
13						
14						
15						

Table 4.7(a)
Model O - Matrix Stresses and Pore Pressures

Node	Vertical Strain	Horizontal Strain	Shear Strain	Max Principal Strain	Min Principal Strain	Void Ratio
1						
2						
3						
4	3.9916E-03	-3.5538E-03	-7.7490E-02	-4.1704E-02	3.6844E-02	4.002
5	8.4856E-03	-8.8517E-03	-5.9998E-02	-3.5644E-02	2.8879E-02	3.998
6	1.0922E-02	-1.5251E-02	-2.2456E-02	2.1371E-02	-1.1433E-03	3.979
7	-8.2902E-03	9.3055E-03	1.1080E-01	5.6611E-02	-5.5580E-02	4.005
8	-8.9419E-03	9.3214E-03	-8.5675E-02	-4.4064E-02	4.3306E-02	4.002
9	-8.5110E-03	8.1839E-03	-3.1999E-02	2.6846E-02	-1.5751E-02	3.998
10	-2.3513E-02	1.9606E-02	-2.9088E-02	3.7704E-02	-2.6968E-02	3.980
11	-3.5533E-02	3.4249E-02	1.5995E-03	5.0181E-02	-3.5540E-02	3.994
12	-4.9904E-02	5.0174E-02	-3.5018E-03	6.1356E-05	-4.9965E-02	4.001
13						
14						
15						

Model O

R upper= **125.00** **mm**

R lower= **80.00** **mm** **Permeability=** **7.358E-08**

Note: '-' implies compressive; Stresses & Pore Pressures are measured in MPa

Table 4.7(b)

Model O - Matrix Strains and Void Ratios

Model P

R upper= 90.00 mm

R lower= 80.00 mm **Permeability= 7.358E-08**

Note: '-' implies compressive; Stresses & Pore Pressures are measured in MPa

Node	Vertical Stress	Horizontal Stress	Shear Stress	Max Principal Stress	Min Principal Stress	Pore Pressure
1	6.0192E-04	-5.8256E-04	-1.8678E-03	1.9691E-03	-1.9498E-03	1.3080E-03
2	1.1602E-03	-1.1654E-03	-1.4541E-03	-1.8645E-03	1.8593E-03	1.5575E-03
3	1.8089E-03	-1.6353E-03	-4.3992E-04	1.8642E-03	-1.6906E-03	1.8483E-03
4	-5.0293E-04	4.9967E-04	-4.2661E-03	-4.2971E-03	4.2938E-03	1.0847E-02
5	-2.9315E-04	2.8978E-04	-3.1732E-03	-1.0009E-03	9.9758E-04	1.0965E-02
6	-1.4572E-04	6.2832E-05	-9.5581E-04	-3.3143E-03	3.2314E-03	1.1048E-02
7	-1.2811E-03	1.2675E-03	-3.2712E-03	-2.5148E-03	2.5012E-03	1.9748E-02
8	-1.6828E-03	1.6574E-03	-2.1601E-03	-1.6857E-03	1.6603E-03	1.9558E-02
9	-2.2159E-03	1.9179E-03	-9.8083E-05	-2.2888E-03	1.9908E-03	1.9366E-02
10	-2.8580E-03	2.7485E-03	5.5372E-04	-2.9047E-03	2.7952E-03	2.6748E-02
11	-4.7433E-03	4.7769E-03	5.1390E-04	4.7771E-03	-4.7435E-03	2.5955E-02
12	-6.2210E-03	6.2662E-03	3.8682E-05	8.1510E-03	-8.1058E-03	2.5667E-02
13	4.1484E-03	-4.2550E-03	5.2046E-03	-5.0551E-03	4.9485E-03	4.4308E-03
14	4.8841E-03	-4.8645E-03	2.7137E-03	4.9131E-03	-4.8935E-03	4.5311E-03
15	3.4766E-03	-3.3680E-03	-5.3224E-04	3.5177E-03	-3.4091E-03	3.1755E-03

Table 4.8(a)
Model P - Matrix Stresses and Pore Pressures

Node	Vertical Strain	Horizontal Strain	Shear Strain	Max Principal Strain	Min Principal Strain	Void Ratio
1	1.4957E-03	-1.4635E-03	-9.3326E-03	4.9114E-03	-4.8792E-03	4.000
2	2.9006E-03	-2.9094E-03	-7.2654E-03	-4.6558E-03	4.6470E-03	4.000
3	4.4469E-03	-4.1577E-03	-2.1981E-03	4.5851E-03	-4.2959E-03	4.001
4	-1.2551E-03	1.2497E-03	-2.1316E-02	-1.0734E-02	1.0729E-02	4.000
5	-7.3096E-04	7.2536E-04	-1.5855E-02	-7.9637E-03	7.9581E-03	4.000
6	-3.2954E-04	1.9149E-04	-4.7758E-03	-2.4711E-03	2.3330E-03	3.999
7	-3.1948E-03	3.1722E-03	-1.6345E-02	-8.7820E-03	8.7594E-03	4.000
8	-4.1936E-03	4.1513E-03	-1.0793E-02	-6.8426E-03	6.8003E-03	4.000
9	-5.4118E-03	4.9155E-03	-4.9008E-04	-5.4176E-03	4.9213E-03	3.997
10	-7.0945E-03	6.9121E-03	2.7667E-03	-7.2298E-03	7.0474E-03	3.999
11	-1.1864E-02	1.1920E-02	2.5678E-03	1.1989E-02	-1.1933E-02	4.000
12	-1.5561E-02	1.5636E-02	1.9328E-04	1.5636E-02	-1.5561E-02	4.000
13	1.0408E-02	-1.0586E-02	2.6005E-02	-1.6800E-02	1.6622E-02	3.999
14	1.2194E-02	-1.2161E-02	1.3559E-02	1.3954E-02	-1.3921E-02	4.000
15	8.6404E-03	-8.4594E-03	-2.6594E-03	8.7432E-03	-8.5622E-03	4.001

Model P

R upper= **90.00** **mm**

R lower= **80.00** **mm** **Permeability=** **7.358E-08**

Note: '-' implies compressive; Stresses & Pore Pressures are measured in MPa

Table 4.8(b)

Model P - Matrix Strains and Void Ratios

Model Q

R upper= 100.00 mm

R lower= 80.00 mm **Permeability= 7.358E-09**

Note: '-' implies compressive; Stresses & Pore Pressures are measured in MPa

Node	Vertical Stress	Horizontal Stress	Shear Stress	Max Principal Stress	Min Principal Stress	Pore Pressure
1	1.1309E-03	-1.1016E-03	-2.7404E-03	2.9737E-03	-2.9444E-03	2.0844E-03
2	2.0841E-03	-2.0453E-03	-2.1103E-03	2.9717E-03	-2.9329E-03	2.5713E-03
3	3.6906E-03	-2.8096E-03	-6.1331E-04	-2.8670E-03	3.7480E-03	3.7253E-03
4	-5.6460E-04	5.5417E-04	-9.6418E-03	-9.6632E-03	9.6528E-03	2.6370E-02
5	6.9118E-05	-4.8410E-05	-7.3538E-03	2.5427E-03	-2.5220E-03	2.6708E-02
6	1.3323E-03	-7.7042E-04	-2.5317E-03	7.7644E-03	-7.2025E-03	2.7527E-02
7	-3.6980E-03	3.5953E-03	-7.4092E-03	-6.4423E-03	6.3396E-03	5.3503E-02
8	-5.1238E-03	5.1562E-03	-5.2485E-03	5.2663E-03	-5.2339E-03	5.3083E-02
9	-6.5808E-03	6.7958E-03	-1.0694E-03	8.5257E-03	-8.3107E-03	5.4057E-02
10	-4.3499E-03	4.1841E-03	5.1121E-03	-6.3664E-03	6.2006E-03	6.3518E-02
11	-7.9550E-03	7.9946E-03	4.6125E-03	1.1643E-02	-1.1604E-02	6.2021E-02
12	9.4521E-03	-9.4265E-03	8.4565E-03	1.2318E-02	-1.2293E-02	1.3816E-02
13	6.2638E-03	6.1334E-03	7.8947E-03	1.2969E-03	1.1100E-02	5.8748E-03
14	7.5934E-03	-7.5649E-03	4.9013E-03	7.6052E-03	-7.5767E-03	6.6065E-03
15	7.7626E-03	-6.3774E-03	4.2307E-04	7.7752E-03	-6.3900E-03	7.2415E-03

Table 4.9(a)

Model Q - Matrix Stressures and Pore Pressures

Node	Vertical Strain	Horizontal Strain	Shear Strain	Max Principal Strain	Min Principal Strain	Void Ratio
1	2.8131E-03	-2.7643E-03	-1.3692E-02	7.4166E-03	-7.3678E-03	4.000
2	5.1905E-03	-5.1258E-03	-1.0544E-02	7.4080E-03	-7.3433E-03	4.000
3	8.8534E-03	-7.3861E-03	-3.0644E-03	9.1557E-03	1.0865E-03	4.007
4	-1.4062E-03	1.3888E-03	-4.8176E-02	-2.4864E-02	2.3329E-02	4.000
5	1.6405E-04	-1.2957E-04	3.6741E-02	-1.9404E-02	1.7410E-02	4.000
6	3.0945E-03	-2.1587E-03	-1.2650E-02	1.3045E-02	-9.2589E-04	4.005
7	-9.1959E-03	9.0248E-03	-3.7021E-02	2.3385E-02	-1.9713E-02	3.999
8	-1.2814E-02	1.2868E-02	-2.6225E-02	2.1848E-02	-1.7774E-02	4.000
9	-1.6530E-02	1.6888E-02	-5.3434E-03	-1.6791E-02	1.0783E-02	4.002
10	-1.0798E-02	1.0522E-02	2.5543E-02	2.4568E-02	-1.5410E-02	3.999
11	-1.9890E-02	1.9956E-02	2.3047E-02	-3.3394E-02	-1.0057E-02	4.000
12	2.3603E-02	-2.3561E-02	4.2254E-02	3.2857E-02	-2.4631E-02	4.000
13	1.5594E-02	-1.5377E-02	3.7447E-02	-2.7119E-02	2.3802E-02	4.001
14	1.8959E-02	-1.8911E-02	2.4490E-02	2.2776E-02	-2.0326E-02	4.000
15	1.8816E-02	-1.6509E-02	2.1139E-03	1.8848E-02	-1.6541E-02	4.011

Model Q

R upper= 100.00 mm

R lower= 80.00 mm **Permeability= 7.358E-09**

Note: '-' implies compressive; Stresses & Pore Pressures are measured in MPa

Table 4.9(b)

Model Q - Matrix Strains and Void Ratios

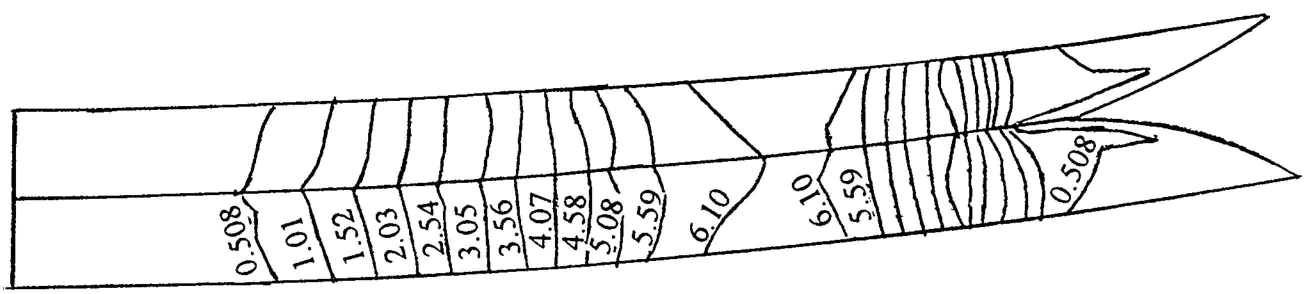

Figure 26
Model M
Pore Pressure Contours in
Apposing Cartilage Layers
R_{upper} = 100 mm, R_{lower} = 80 mm
x 100 MPa

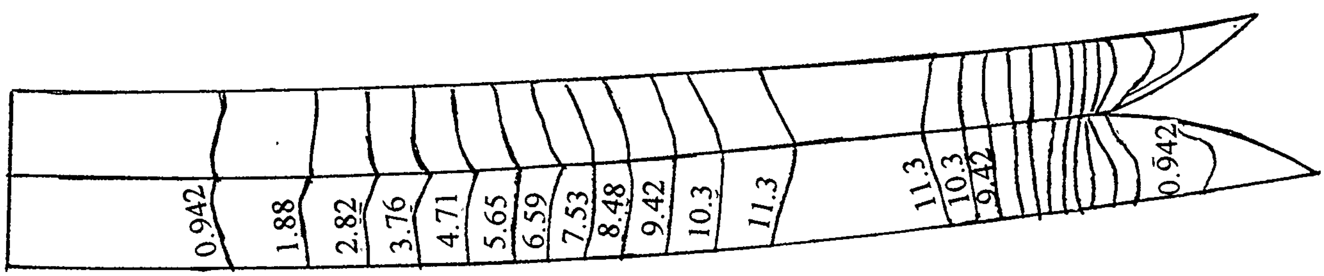

Figure 27
Model N
Pore Pressure Contours in
Apposing Cartilage Layers
R_{upper} = 110 mm, R_{lower} = 80 mm
x 100 MPa

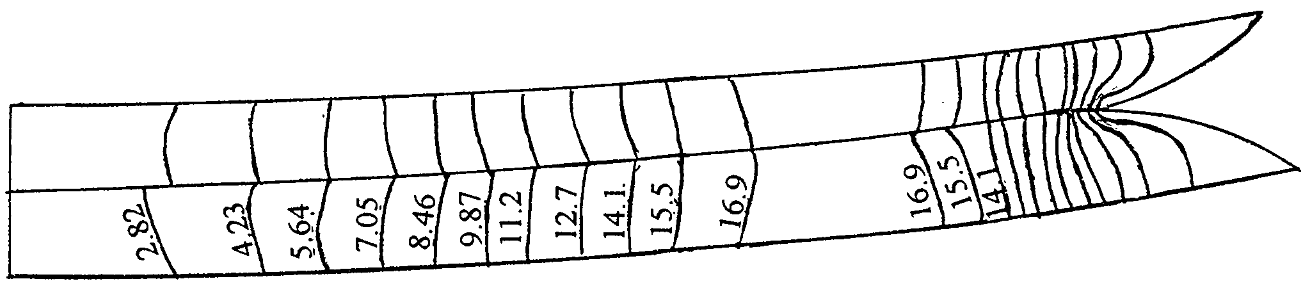

Figure 28
Model O
Pore Pressure Contours in
Apposing Cartilage Layers
R_{upper} = 125 mm, R_{lower} = 80 mm
x 100 MPa

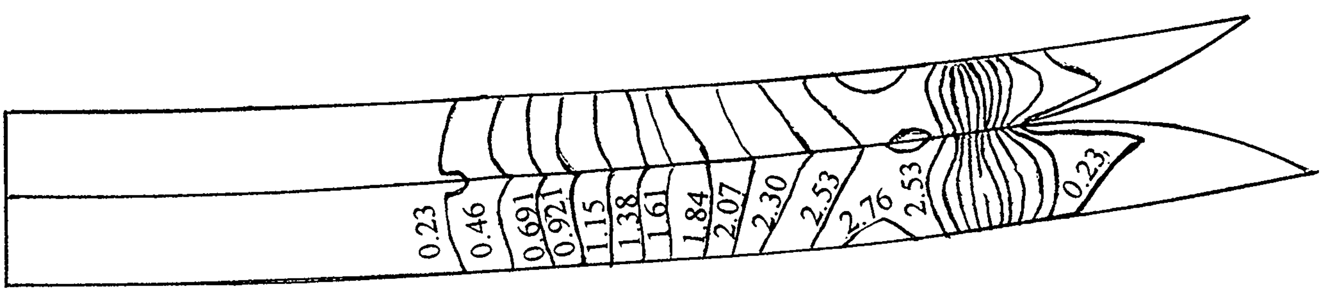

Figure 29
Model P
Pore Pressure Contours in
Apposing Cartilage Layers
R_{upper} = 90 mm, R_{lower} = 80 mm
x 100 MPa

5.0 Comparison of Indentor Model To Full Diarthrodial Joint Model

5.1 Discussion

The pore pressure plots of Models A through L at t=20 seconds, Figures C-1 to C-12 found in Appendix C, were compared to the pore pressure plots of Models M to P, Figures 26 to 29 in terms of magnitude and location.

This time t=20 seconds was arbitrarily chosen in order to compare the models at the same point in time. However, as seen in Figure C-1 to C-12, the pore pressures at t=20 seconds are not uniform through the depth of the tissue. T=500s (peak displacement) is probably the best time period at which to compare the pore pressures, since columns of pore pressure through the depth of the tissue are visible, see Figures B-1 to B-12, but realistically is too long for comparison with results from laboratory tests. Paul (1976) determined that during a normal walking speed, the human knee joint is loaded at a frequency between 0.5 and 1.0 Hertz. Thus comparisons of models should be made at shorter time periods in order to more closely simulate reality.

In order to develop indentation models of cartilage and full joint relaxation models of cartilage loaded at these faster rates, care must be taken to ensure that the length of time is greater that the critical time step. Refinement of the mesh under the loaded zone enables faster loading rates to be used in the models. However inertial effects associated with faster loading speeds seem to appear at loading rates faster than 1 second.

The magnitudes of pore pressures in Figure C-1 to C-12 compared closely to the pore pressures in Figures 26 to 29, however, only Figures C-1 to C-3 will be considered in this analysis since Figures C-4 to C-12 have significant variation in pore pressures through the depth of the tissue, and Figure C-1 to C-3 have fairly uniform columns of pore pressure through the depth of the tissue, as do Figures 26 to 29.

Further, the nodes in the region surrounding the indentor edge will be considered since these locations provide the most uniform pore pressures through the depth of the tissue. The magnitudes of pore pressures in these regions range from approximately 3E-2 to 4E-2 MPa. These columns of pressure correspond to different locations within the contact zone of Figures 26 to 29 depending on the width of this zone.

As illustrated earlier, the larger the radii of curvature of the upper surface relative to the lower surface (to a limiting radius as mentioned earlier), the larger the contacting surface, and thus, the larger the pore pressures.

In Model O, the pore pressures are the largest, relative to the other models, thus the column of pore pressure, 3E-2 to 4E-2 MPa, near the indentor edge of the indentation model corresponds to an area further out from the centre of the contact area. Similarly, this location moves inward toward the contact zone centreline as the upper radius decreases.

The pore pressures for Model P, Figure 29, are relatively small due to the small contact zone width; these pore pressures from Figure C-1 to C-3 differ remarkably from the pore pressures built up within the tissue of Model P.

Thus, it appears that comparison of data from the indentor model to the full joint model must be carefully examined.

The full joint model geometry must be taken into consideration since the magnitudes of stresses vary widely with the congruity of the apposing surfaces.

The aspect ratio, r/h, in the indentation model must be greater than approximately 1.60 for the tissue beneath the indentor to develop columns of pore pressure through its depth, and the results to be interpretable. For values of r/h<1.60, the pore pressures in the tissue are not uniform through the thickness of tissue. This behaviour was also present at t = 500 s, Figure B-1 to B-12. It appears, however, that at a longer time span, the pore pressures become uniform throughout the thickness of the tissue at aspect ratios, r/h, < 1.60. However, as indicated previously, a loading span of t = 500 s (or 8.5 minutes) is not very physiologically relevant.

Thus, in order for the results to be physiologically relevant, an aspect ratio, r/h, should be greater than 1.60.

These models were compared on the basis of pore pressure. Likewise, the vertical stresses could also have been used as a basis for comparison since one parameter increases as the other parameter decreases.

6.0 Overall Conclusions

Articular cartilage, a soft, water-saturated connective tissue covering the surface of bones in synovial joints, normally provides a lifetime of use. There may be wear and tear; articular cartilage can repair itself under typical activity levels. The tissue is uniquely designed to maintain significant stiffness and resilience because of its high water content, in order to provide a self-lubricating, low-friction gliding, and load-distributing surface for synovial joints.

The purpose of this study was to compare the results of an unconfined time-dependent model in which the indentor geometry was flat and indentor material properties were dissimilar to the articular cartilage, with the results from a diarthrodial joint model where the indentor was another non-planar cartilage surface, to observe where within the contact zone of the joint model the results compare.

An estimation of the aspect ratio (r/h) limit of the indentor model was also to be determined.

In this analysis, the finite element model was developed to study the behaviour of articular cartilage undergoing displacement-controlled indentation tests and stress relaxation.

The recorded pore pressures for the models in Step 2 of the displacement-controlled indentation test were generally found to be less than the magnitudes of the vertical stresses in the matrix. These results indicate that if the tissue is loaded sufficiently slow enough that the water does not get trapped in the matrix, and is able to flow away from the loaded region of tissue under the indentor. As a result, the matrix of the tissue has to support part of the applied load. These results indicate that under slow loading conditions more of the load is supported by the matrix than by the tissue fluid.

The pore pressures in the deep region of the cartilage, under the indentor, and along the centreline indicate that the pore pressures and matrix stresses are closer in value than for models A through D. The water in these regions of the cartilage gets trapped in the matrix and ends up carrying more load, and thus the magnitude of the pore pressure increases while the matrix stresses decrease as more of the load is shared between matrix and tissue fluid.

The pore pressures were greater in the region just beyond the edge of the indentor than the matrix stresses since this region of the tissue is not directly loaded, and the tissue fluid escapes laterally, and vertically out of the cartilage.

The vertical stresses in the loaded region of the matrix are compressive illustrating the lack of upward movement of tissue fluid in this region. However, outside of the loaded region, the vertical stresses are tensile towards the surface of the tissue layer indicating the upward movement of water in this region..

As the r/h ratio becomes smaller, or rather, as the height of the cartilage plug increases with respect to the indentor radius, more of the cartilage matrix experiences a lateral drag resulting from the movement of water. Since the cartilage plugs are loaded to the same depth relatively ($u_Z/h = -0.05$), models with smaller r/h experience more tissue fluid lateral movement than larger r/h models.

Fluid escaped from the voids as the tissue was indented. The degree to which the fluid was exuded out of the pores varied from model to model. The amount of fluid exuded from the models with larger r/h ratios seemed to generally increase with depth from the surface, thus more fluid flow occurred deeper in the tissue beneath the indentor. Conversely, with smaller r/h ratios, more fluid flow occurred towards the superficial region of the cartilage relative to the deeper regions.

The aspect ratio (r/h) limit necessary to produce physiologically relevant results in the cartilage is 1.60.

Loading rate had a substantial effect on the reaction force . The stresses in the matrix were higher for the model loaded at a slower rate. The pore pressures for the faster loading rate were found to be higher than the more slowly loaded case indicating that the water which is trapped in the tissue, under rapid loading, is unable to flow away from the loaded region because of the low permeability. The majority of the load is therefore resisted by this water and as a result, the tissue takes on the characteristics of water under compression.

The decrease in void ratio in the cartilage under the indentor indicated that the permeability of the tissue under the indentor decreased, and as a result there was no fluid flow. This behaviour combined with the columns of pore pressures through the depth of the tissue under the indentor, which indicates the lack of vertical fluid movement, point to the validity of a sealed boundary condition under the indentor, since the tissue essentially seals itself.

The results from the stress relaxation model for a full joint model indicate that as the radius of the upper joint becomes smaller, less vertical movement of water occurred within the matrix. Lateral movement of water away from the centreline regions of the cartilage tissue occurs, with vertical movement of this fluid, toward the surface, near the outer edges of the contact zone, and beyond.

The pore pressures for each of the models were generally significantly larger than the vertical stresses recorded for the matrix at the same locations indicating that the majority of the load is carried by the trapped tissue fluid.

The full joint model analysis, concluded that as the radius of the upper articular joint surface increases relative to the radius of the lower joint, and therefore, the contact zone size increases, the magnitudes of the pore pressures similarly increase.

The void ratios of the regions of tissue surrounding the centreline indicate that as the tissue is compressed, some tissue fluid was squeezed out of the pores (void ratio = volume of voids/volume of solids). This result was displayed by the magnitudes of the void ratios in this region decreasing from the initial input value of 4.0. The void ratios of the outer regions of cartilage, beyond the contact region, either remained constant, or increased. This increase implied a movement of tissue fluid into the region since the only route of escape for the fluid was laterally outward, away from the centreline, and up out of the cartilage. Thus, the results validate the use of a sealed hydraulic boundary in the contact zone. The permeability in this region decreases, indicating a lack of fluid flow, thus the cartilage essentially seals itself.

The contact zone width increased as the upper radius increased in magnitude, relative to the lower layer. This result was expected since the outer regions of the cartilage layers make contact first as the two apposing surfaces are compressed together. Increasing the upper radius flattens the layer relative to the lower surface, thus bringing the two surfaces closer together.

The full joint model analysis, concluded that as the radius of the upper articular joint surface increases relative to the radius of the lower joint, and therefore, the contact zone size increases, the magnitudes of the pore pressures similarly increase. This analysis determined the aspect ratio required for an indentor model to give reasonable results. As was shown, when compared to a full joint model, these values corresponded to different regions within the contact zone in the full joint model depending on the congruity between the two surfaces. Thus, it was not possible to determine an exact location within a full joint model that these values corresponded to.

In order to determine such a location, one approach could be to develop a model which allows the force applied to the full joint to be varied in order that the resulting contact zone is a set width for each model regardless of the congruity of the apposing layers. Under such conditions, the location under the contact zone withing the full joint model could be determined, and the force required could then be used in the laboratory in indentation testing. The values determined by laboratory tests could then be compared to a desired location within the full joint. By altering the magnitude of the applied load, the contact width would change, and the corresponding locations would likewise change.

This approach of controlling the size of the contact zone by altering the applied force may be required to determine where within the full joint, laboratory indentation testing corresponds.

In summary, the indentor model produced a number of interesting results:

- The radius of the corner of the indentor should be greater than 0, and less than or equal to to width of the outer-most cartilage element under the indentor
- As the rate of indentation increased:
    - the pore pressures in the cartilage increased,
    - the matrix stresses in the cartilage decreased,
    - the pore pressure contours under the indentor were no longer vertical columns through the tissue thickness
    - the tissue began to behave like water under compression
- The aspect ratio (r/h) should be kept greater than 1.60 in order to produce physiologically relevant results in the tissue
- Indentation tests estimated at t=20 seconds for $2.00 \leq \frac{r}{h} \leq 0.80$, and for the indentation test loaded for maximum displacement at t=5s, indicate that the highest pore pressures occur at the base of the cartilage, or rather, at the cartilage/bone interface possibly suggesting that the onset of osteoarthritis could occur at the cartilage/bone interface under these conditions

- Indentation tests estimated at t=20 seconds for $0.73 \leq \frac{r}{h} \leq 0.40$, indicate that the highest pore pressures occur in the STZ toward the centreline of the cartilage possibly suggesting that the onset of osteoarthritis could occur in the STZ under these conditions
- The use of a sealed hydraulic boundary condition on the cartilage surface under the indentor was verified by the results:
  - columns of pore pressure through the depth of the tissue under the indentor indicating the lack of vertical movement of fluid
  - a decrease in the void ratios at nodes under the indentor indicating a decrease in the permeability of the tissue indicating no fluid flow thus, indicating that the tissue essentially seals itself.

The full joint model produced the following results:

- Given R_{lower} = 80 mm, 80mm < $R_{upper} \leq$ 125mm. If,
  - R_{upper} is less than 80mm, the upper surface slopes upwards quickly toward the outer edge of the model. Given the gap necessary at the centreline of the model, and the fact that contact first occurs at the outer edge of the model, contact does not occur between the two apposing cartilage surfaces
  - R_{upper} is greater than 125mm, the upper surface becomes too flat relative to the lower surface and instabilities arise in the numerical model
- As R_{upper} increases, relative to R_{lower} :

- the contact zone width increases
- the pore pressures in the cartilage within the contact zone increases

- Given that a gap is maintained at the centreline of the joint model for each of the models, when R_{upper} is large (125mm) relative to the R_{lower} , the upper surface is flat relative to the lower surface, a large contact width develops between the apposing layers, and the pore pressures are large, indicating that large forces are induced in the tissue for a given applied displacement. When R_{upper} is approximately equal to R_{lower} , the contact width is small as are the pore pressure, indicating that smaller forces are induced in the tissue for the same applied displacement as for the case when R_{upper} is larger. Since the contact pore pressures of this model increased significantly with an increase in contact zone width, and increase in incongruity between the upper and lower surface, a model developed to load joint of differing degrees of incongruity with the same magnitude of load, would possibly produce low pore pressures for models with more congruous surfaces, and higher pore pressures for models with less incongruous surfaces.
- The use of a sealed hydraulic boundary condition for contacting nodes in the full joint model was verified by the results:
    - columns of pore pressure through the depth of the cartilage in the contact zone indicating the lack of vertical movement of fluid

- a decrease in the void ratios at nodes within the contact zone indicating a decrease in the permeability of the tissue indicating no fluid flow thus, indicating that the tissue essentially seals itself.

Comparison between the time-dependent indentation model and the full joint model produced the following results:

- Given $\frac{r}{h} > 1.60$, the pore pressures at the tip of the indentor correspond to pore pressures in the full joint relaxation model at the following locations:
  - Given $R_{lower} = 80$mm, the pore pressures correspond to a location on the full joint towards the contact zone centreline when $R_{upper} \approx 80$mm. This location moves outward from the contact zone centreline as R_{upper} increases.

This analysis provides mechanical information for properties of cartilage including pore pressures, principal stresses and strains in the matrix, global x and y stresses and strains in the matrix, and void ratios for correlation with future metabolic response of cartilage tissue to load.

This correlation will allow for the development of a logical hypothesis, which can be tested, as to which mechanical parameter of cartilage is of potential relevance.

References

Adams, M. K. (1994). Changes in aggrecan populations in experimental osteoarthritis. Osteoarthritis and Cartilage, 2, pp. 155-164.

Anderson, K. N., Anderson, L. E. (1990). Mosby's Pocket Dictionary of Medicine Nursing & Allied Health, St. Louis: The C. V. Mosby Company.

Askew, M. J., & Mow, V. C. (1978). The biomechanical function of the collagen fibril ultrastructure of articular cartilage. Journal of Biomechanical Engineering, 100, pp. 105-115.

Aspden, R. M., & Hukins, D. W. L. (1981a). Collagen organization in articular cartilage, determined by x-ray diffraction and its relationship to tissue function. Proc. Roy. Soc. London, 212 (B), pp. 299-304.

Aspden, R. M., & Hukins, D. W. L. (1981b). Calcification of the deep zone in pig femoral head cartilage. Experientia, 37, pp. 1333-1334.

Ateshian, G. A., & Wang, H. (1994). Rolling and Sliding Contact of Cylindrical Biphasic Articular Surfaces Using Integral Transform Methods. Proceedings from the Application of High Performance Computing in Engineering, 1994, pp. 21.

Bachrach, N. M., Ateshian, G. A., & Mow, V. C. (1993). Effects of Subchondral Plate Fracture on Articular Cartilage Response. 1993 Bioengineering Conference, BED-Vol. 24, New York: ASME, pp. 630-633.

Beer, F. P., Johnston, Jr., E. R. (1985). Mechanics of Materials, SI Metric Edition, 2nd ed., Toronto: McGraw-Hill Ryerson Ltd.

Brown, T. D., & Singerman, R. J. (1986). Experimental determination of the linear biphasic constitutive coefficients of human fetal proximal femoral chondroepiphysis. Journal of Biomechanics, 19 (8), pp. 597-605.

Coletti, J. M., Akeson, W. H., & Woo, S. L.-Y. (1972). A comparison of the physical behavior of normal articular cartilage and the arthroplasty surface. The Journal of Bone and Joint Surgery, 54-A (1), pp. 146-160.

Comper, W. D., Williams, R. J. W., & Zamparo, O. (1990). Water transport in extrarticular cellular matrices. Conn. Tiss. Res., 25, pp. 89-102.

Dodge, G. R., & Poole, A. R. (1989). Immunohistochemical detection and immunochemical analysis of type II collagen degradation in human normal, rhematoid, and osteoarthritic articular cartilages and in explants of bovine articular cartilage with interleukin 1. Journal of Clinical Investigation, 83, pp. 647-661.

Dunkin, M. A., & Morrow, S. (1994). 2020: A vision of arthritis in the future. Arthritis Today, Jul/Aug.

Eberhardt, A. W., Keer, L. M., Lewis, J. L., & Vithooritien, V. (1990). An analytical model of joint contact. Journal of Biomechanical Engineering, 112, pp. 407-413.

Eberhardt, A. W., Lewis, J. L., & Keer, L. M. (1991a). Contact of layered elastic spheres as a model of joint contact: Effect of tangential load and friction. Journal of Biomechanical Engineering, 113, pp. 107-108.

Eberhardt, A. W., Lewis, J. L., & Keer, L. M. (199b). Normal contact of elastic spheres with two elastic layers as a model of joint articulation. Journal of Biomechanical Engineering, 113, pp. 410-417.

Elmore, S. M., Sokoloff, L., Norris, G., & Carmeci, P. (1963). Nature of 'Imperfect' Elasticity of Articular Cartilage. Journal of Applied Physiology, 18, pp. 393-396.

Eyre, D. R., Apone, S., Wu, J. J., Ericsson, L. H., & Walsh, K. A. (1987). Collagen type IX: evidence for covalent links to type II collagen in cartilage. FEBS Lett., 220, pp. 337-341.

Eyre, D. R., Wu, J. J., Woods, P. E., & Weis, M. A. (1991). The cartilage collagens and joint degradation. British Journal of Rheumatology, 30 (Suppl. 1), pp. 10-15.

Greenwald, A. S., & O'Connor, J. J. (1971). The Transmission of load Through The Human Hip Joint. Journal of Biomechanics,4, pp. 507-528.

Hayes, W. C., Keer, L. M., Herrmann, G., & Mockros, L. F. (1972). A mathematical analysis for indentation tests of articular cartilage. Journal of Biomechanics, 5, pp. 541-551.

Hayes, W. C., & Mockros, L. F. (1971). Viscoelastic properties of human articular cartilage. Journal of Applied Physiology, 31 (4), pp. 562-568.

Hibbitt, Karlsson & Sorensen, Inc. (1994). ABAQUS version 5.4 (computer programme). Pawtucker, R. I: author.

Hirsch, C. (1944). Pathogenesis of chondromalacia of the patella. A Physical Histologic and Chemical Study. Acta Chir. Scand. Suppl, 83, pp. 1-106.

Holtz, R. D., Kovacs, W. D. (1981). An Introduction to Geotechnical Engineering, New Jersey: Prentice-Hall, Inc.

Hooley, C. J., & Cohen, R. E. (1979). A mödel for the creep behaviour of tendon. International Journal of Biological Macromolecules, 1, pp. 123-132.

Hori, R. Y., & Mockros, L. F. (1976). Indentation Tests of Human Articular Cartilage. Journal of Biomechanics, 9, pp. 259-268.

Hukins, D. W. L. (1982). Biomechanical properties of collagen. Collagen in Health and Disease, (eds. J. B. Weiss, & M. I. V. Jayson), Edinburgh: Churchill Livingstone, pp. 49-72.

Hukins, D. W. L. (1984). Collagen orientation. Connective Tissue Matrix, (ed. D. W. L. Hukins), London: Macmillan, pp. 211-240.

Hukins, D. W. L., & Aspden, R. M. (1989). Fibre-reinforcing in articular cartilage. In A. L. Yettram, ed. Material properties and stress analysis, Manchester: University Press, pp. 44-59.

Hukins, D. W. L., Aspden, R. M., & Yarker, Y. E. (1984). Fibre reinforcement and mechanical stability of articular cartilage. Engineering in Medicine, 13, pp. 153-56.

Jurvelin, J., Kirivanta, I., Säämänen, A. M., Tammi, M., & Helminen, H. J. (1990). Indentation stiffness of young canine knee articular cartilage - ingluence of strenuous joint loading. Journal of Biomechanics, 23 (12), pp. 1239-1246.

Kempson, G. E., Spivey, C. J., Swanson, S. A. V., & Freeman, M. A. R. (1971). Patterns of cartilage stiffness on normal and degenerate human femoral heads. Journal of Biomechanics, 4, pp. 597-609.

Lai, W. M., Mow, V. C., & Roth, V. (1981). Effects of nonlinear strain-dependent permeability and rate of compression on the stress behavior of articular cartilage. Journal of Biomechanical Engineering, 103, pp. 61-66.

Mak, A. F., Lai, W. M., & Mow, V. C. (1987). Biphasic indentation of articular cartilage - Theoretical analysis. Journal of Biomechanics, 20 (7), pp. 703-714.

Mankin, H. J., Mow, V. C., Buchwaller, J. A., Iannotti, J. P., Radcliffe, A. (1994) Form & Function of Articular Cartilage. Orthopaedic Basic Science, 1, pp. 1-44.

Mansour, J. M., & Mow, V. C. (1976). The permeability of articular cartilage under compressive strain and at high pressures. The Journal of Bone and Joint Surgery, 58A, pp. 509-516.

Maroudas, A. (1973). Physico - Chemical Properties of Articular Cartilage. Adult Articular Cartilage, ed., New York: M.A.R. Freeman; Grune and Stratton, pp. 131-170.

Mayne, R. (1989). Cartilage Collagens, What Is Their Function, and Are They Involved in Articular Disease? Journal of Arthritis and Rheumatism, 32 (3), pp. 241-246.

Meachim, G., & Stockwell, R., A. (1973). The Matrix. Adult Articular Cartilage, ed., New York: M.A.R. Freeman, Grune and Stratton, pp. 1-50.

Mizrahi, J., Maroudas, A., Lanir, Y., Ziv, I., & Webber, T. J. (1986). The 'instantaneous' deformation of cartilage: Effects of collagen fiber orientation and osmotic stress. Biorheology, 23, pp.311-330.

Mow, V. C., Holmes, M. H., & Lai, W. M. (1984). Fluid transport and mechanical properties of articular cartilage: A review. Journal of Biomechanics, 17 (5), pp. 377-394.

Mow, V. C., Hou, J. S., Owens, J. M., & Ratcliffe, A. (1990). Biphasic and quasilinear viscoelastic theories for hydrated soft tissues. In V.C. Mow, A. Ratcliffe, & S. L. - Y. Woo, ed. Biomechanics of diarthrodial joints: Volume I, New York: Springer-Verlag.

Mow, V. C., Kuei, S. C., Lai, W. M., & Armstrong, C. G. (1980). Biphasic Creep and Stress Relaxation of Articular Cartilage in Compression: Theory and Experiments. Journal of Biomechanical Engineering, 102, pp. 73-84.

Mow, V. C., & Lai, W. M. (1979). Mechanics of Animal Joints. Annual Review of Fluid Mechanics, 11, (ed. M. Van Dyke), pp. 247-288.

Mow, V. C., Lai, W. M. (1980). Recent developments in synovial joint biomechanics. SIAM Review, 22 (3), pp. 275-317.

Mow, V. C., Proctor, C. S., & Kelly, M. A. (1989). Biomechanics of articular cartilage. In V. H. Frankel & M. Nordin (ed.). Basic biomechanics of the musculoskeletal system, Philadelphia: Lea and Febiger, pp. 31-57.

Mow, V. C., Ratcliffe, A., & Poole, A. R. (1992). Cartilage and diarthrodial joints as paradigms for hierarchical materials and structures. Journal of Biomaterials, 13 (2), pp. 67-97.

Muir H. (1973). Biochemistry. Adult Articular Cartilage, ed., New York: M.A.R. Freeman, Grune and Stratton, pp. 100-130.

Muir, I. H. R. (1979). .Biochemistry. Adult Articular Cartilage, 2nd ed., ed. M. A. R. Freeman, Tunbridge Wells: Pitman Medical., pp. 145-214.

Muir, I. H. R. (1983). Proteoglycans as Organizers of the Intercellular Matrix. Biochemical Society Trans., 11 (6), pp. 613-622.

Oloyede, A., Flachsmann, R., & Broom, N. D. (1992). The dramatic influence of loading velocity on the compressive response of articular cartilage. Connective Tissue Research, 27, pp. 211-224.

Parsons, J. R., & Black, J. (1977). The viscoelastic shear behaviour of normal rabbit articular cartilage. Journal of Biomechanics, 10, pp. 21-29.

Parsons, J. R., & Black, J. (1979). Mechanical behavior of articular cartilage: Quantitative changes with alteration of ionic environment. Journal of Biomechanics, 12, pp. 765-773.

Paul, J. P. (1976). Approaches to design - forced actions transmitted by joints in the human body. Proceedings of the Royal Society of London, 192, pp. 163-172.

PDA Engineering ( ). Patran version 2.5-3 (computer programme).

Pillai, S., U., & Kirk, D., W. (1988). Reinforced Concrete Design, 2nd ed., Toronto: McGraw-Hill Ryerson Limited, pp. 19.

Roth, V., & Mow, V. C. (1980). The intrinsic tensile behaviour of the matrix of bovine articular cartilage and its variation with age. Journal of Bone Joint Surgery, 62A, pp. 1102-1117.

Schmidt, M. B., Mow, V. C., Chun, L. E., & Eyre, D. R. (1990). Effects of proteoglycan extraction on the tensile behaviour of articular cartilage. Journal of Orthopaedic Research, 8, pp. 353-363.

Sharma, M., Langrana, N. A., Rodriguez, J. (1993). Analytical Study on The Role of Lumbar Facets Under Compressive Loads. 1993 Bioengineering Conference, BED-Vol. 24, pp. 462-465.

Shrive, N. G., & Frank, C. B. (1994). Articular Cartilage. Biomechanics of the Musculo-Skeletal System, (Eds. Nigg & Herzog) John Wiley and Sons.

Sokoloff, L. (1966). Elasticity of aging cartilage. Federation Proc. Fedn Am Socs exp. Biol., 25, pp. 1089-1095.

Spilker, R. L., Suh, J. -K., & Mow, V. C. (1988). A finite element formulation of the nonlinear biphasic model for articular cartilage and hydrated soft tissues including strain-dependent permeability. In R. L. Spilker & B. R. Simon (eds.). Computational methods in bioengineering, New York: ASME, pp. 81-92.

Spilker, R. L., Suh, J. -K., & Mow, V. C. (1992). A finite element analysis of the indentation stress-relaxation response of linear biphasic articular cartilage. Journal of Biomechanical Engineering, 114, pp191-201.

Swanson, S. A. V. (1979). Friction, wear and lubrication. Adult Articular Cartilage, 2nd ed., (ed. M. A. R. Freeman), Tunbridge Wells: Pitman Medical., pp. 415-460.

Torzilli, P. A., & Mow, V. C. (1976). On the Fundamental Fluid Transport Mechanisms through Normal and Pathological Articular Cartilage. Journal of Biomechanics, 9, pp. 541-552.

van der Voet, A. F. (1992). Finite Element Modelling of Load Transfer Through Articular Cartilage, Ph.D. Thesis, University of Calgary. National Library of Canada, Ottawa.

van der Voet, A. F., Shrive, N. G., & Schachar, N. S. (1993). Numerical Modelling of Articular Cartilage in Synovial Joints: Poroelasticity and Boundary Conditions. Proceedings of the International Conference on Computer Methods in Biomechanics and Biomedical Engineering (eds. Middleton, J. and Pande, G. N.), Swansea: Books and Journals International, pp. 200-209.

Vermilyea, M. E., & Spilker, R. L. (1992). A hybrid finite element formulation of the linear biphasic equations for hydrated soft tissue. International Journal for Numerical Methods in Engineering, 33, pp. 567-593.

Waters, N. E. (1965). The indentation of thin rubber sheets by cylindrical indentors. British Journal of Applied Physics, 16, pp. 1387-1392.

Wayne, J. S. (1993). Effects of Interstitial Fluid Pressure on Cartilage Behaviour in Diarthrodial Joints. 1993 Bioengineering Conference, BED-Vol. 24, New York: ASME, pp. 638-641.

Wayne, J. S., Kwan, M. K., & Woo, S. L. -Y. (1989). Application of the u-p finite element method to biphasic modelling of articular cartilage. First World Biomechanics Congress, San Diego, pp. 37-40.

Wayne, J. S., Woo, S. L. -Y., & Kwan, M. K. (1991). Application of the u-p finite element method to the study of articular cartilage. Journal of Biomechanical Engineering, 113, pp. 397-403.

Woo, S. L. -Y., Akeson, W. H., & Jemmott, C. F. (1976). Measurements of Nonhomogeneous Directional Mechanical Properties of Articular Cartilage in Tension. Journal of Biomechanics, 9, pp. 785-791.

Woo, S. L. -Y., Lubock, P., Gomez, M. A., Jemmott, G. F., Kuei, S. C., & Akeson, W. H. (1979). Large deformation nonhomogeneous and directional properties of articular cartilage in uniaxial tension. Journal of Biomechanics, 12, pp. 437-446.

Woo, S. L. -Y., Mow, V. C., & Lai, W. M. (1987). Biomechanical properties of articular cartilage. Handbook of Bioengineering (eds. R. Skalak & S. Chien), New York: McGraw-Hill, pp. 4.1-4.44.

Zarek, J. M., & Edwards, J. (1963). The stress-structure relationship in articular cartilage. Medical Electronics and Biological Engineering, 1, pp. 497-507.

Zarek, J. M., & Edwards, J. (1965). Dynamic consideration of the human skeletal system. In R. M. Kenedi (ed.). Biomechanics and related bio-engineering topics, London: Pergamon, pp. 187-204.

A.0 Appendix A

In this analysis, the ABAQUS finite element code was used to model a simulation of a displacement-controlled indentation test in order to determine the effect that a rounded versus square indentor tip had on the cartilage plug.

A.1 Model Geometry

The axisymmetric model of cartilage developed in Step 1 of section 3.2 was used in this analysis. The indentor was of radius, r=1.25mm, and the cartilage layer had a radius, R=10mm, and height, h=2.5mm, see Figure A.1.

The radius of the indentor edge was modelled using the parameters found in Table A-1:

Table A-1

Corner Radius of Indentor Edge

Model	**r_{corner} (mm)**
A	0.03
B	0.00
C	0.075

The values of r_{corner} for Models A and C were chosen to illustrate the effect r_{corner} has on the results of the models when the magnitude is smaller, and greater, respectively, than the element width of the outermost interface element below the indentor, see Figure A-1.

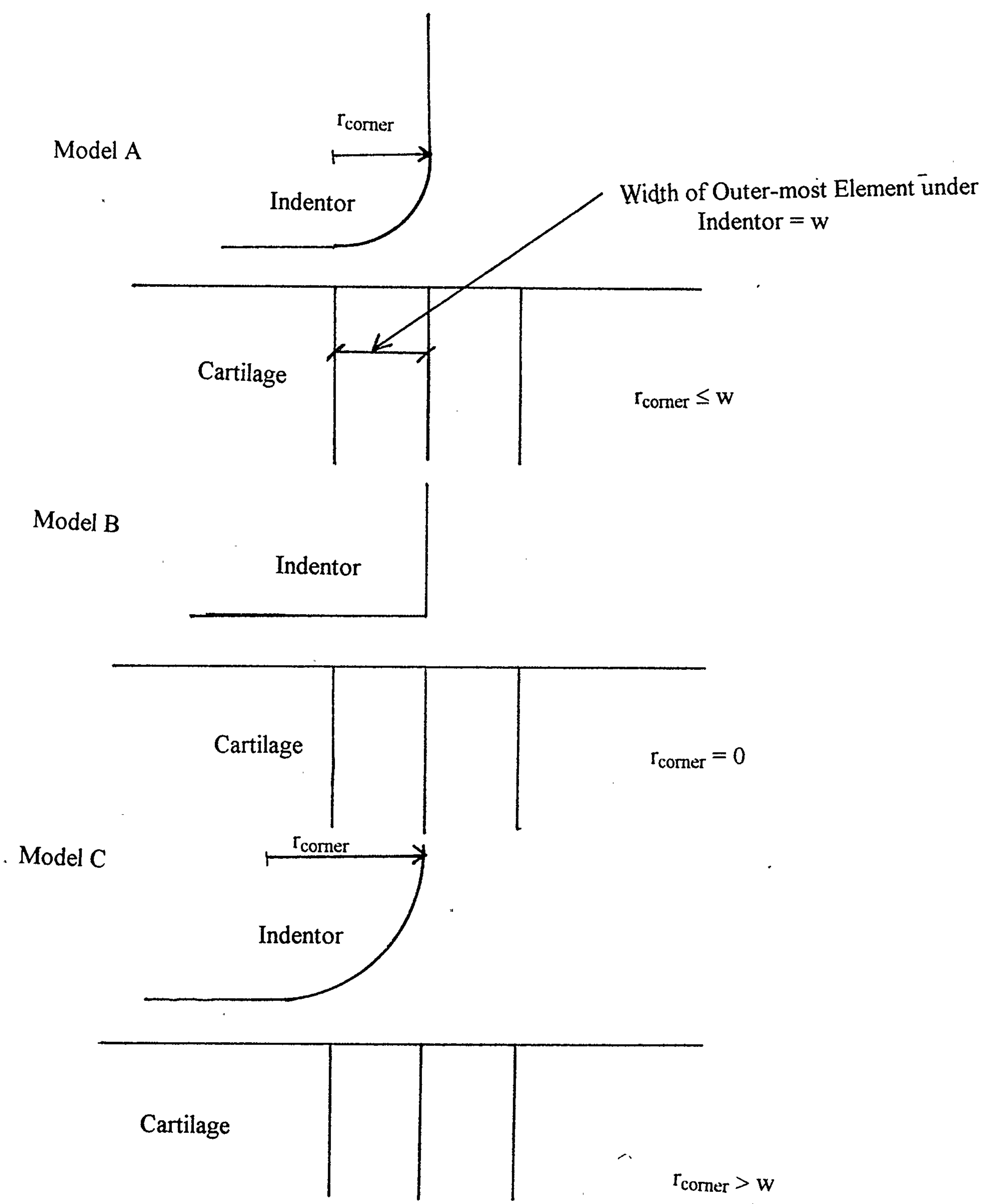

Figure A-1
Edge Detail of Indentor Tip for Models A, B, C

A.2 Elements

The elements used to model the cartilage were 8-noded axisymmetric elements, CAX8RP, with biquadratic displacement and bilinear pore pressure, as in Step 1 of section 3.2.

The indentor was modelled using solid section elements defined such that the normal to the section was pointing outward.

A.3 Boundary Conditions

Rollers were used along the centreline of the model which allowed for the cartilage to move freely in the global y-direction, but prevented radial displacements. The base of the model was fixed in the global x and y-directions.

The cartilage surface was modelled as sealed under the indentor and free-draining in the unloaded region, simulating an impermeable indentor. The free-draining cartilage surface was modelled by setting the pore pressures on the cartilage surface to zero.

A.4 Material Properties

The cartilage elastic and hydraulic material properties used in the model are the same as those listed in Table 3.1. Isotropy was assumed for both the elastic and hydraulic properties.

A.5 Loading

A time-dependent displacement was applied to the top of the indentor, ramping linearly from u_Z = 0mm at t=0s, to u_Z = 0.125mm at t=500s, and kept constant until t=2000s. The timestep used in this analysis was the same (5 s) as used in Step 1, section 3.2.

A.6 Results

The locations of the nodes at which the results were recorded are summarized in Table A-2. The results for the models A, B, and C (summarized in Table A-3, A-4, A-5 respectively) indicate the substantial effect that the corner of the indentor tip has on the results.

The results for Model A compared well with Spilker et al (1988) and Van der Voet (1992). This model was used in Section 3.2 , thus no further discussion will be given in this section.

The vertical stresses recorded for Model B in the superficial zone, at R=$\frac{3r}{4}$, and $\frac{5r}{4}$ were larger than those measured for Model A. This type of behaviour was expected since stress concentrations are known to develop in finite element models at sharp edges. This type of discontinuity causes the results of the model to be somewhat skewed. In Model B, this behaviour was displayed in the larger vertical stresses in the regions surrounding the indentor edge.

Table A-2
Location of Nodes for Models A, B, C

Node	**x-coordinate (measured radially outward from the centreline of plug)**	**y-coordinate (measured upwards from the base of plug)**
1	0	0.2h
2	0	0.4h
3	0	0.6h
4	0	0.8h
5	0	1.0h
6	3r/4	0.2h
7	3r/4	0.4h
8	3r/4	0.6h
9	3r/4	0.8h
10	3r/4	1.0h
11	r	0.2h
12	r	0.4h
13	r	0.6h
14	r	0.8h
15	r	1.0h
16	5r/4	0.2h
17	5r/4	0.4h
18	5r/4	0.6h
19	5r/4	0.8h
20	5r/4	1.0h

where: r = radius of indentor = 1.25mm

h = height of cartilage plug = 2.5mm

Model C produced vertical stresses at R=r, and $R=\frac{5r}{4}$ which were less than the vertical stresses recorded for Model A at the same locations. The vertical stresses at $R=\frac{3r}{4}$, however, were greater than the vertical stresses at the locations measured in Model A. This difference is attributed to the size of the radius of the corner. The larger the radius of the corner of the indentor tip, the smaller the contact area between indentor and cartilage, thus the larger the stresses developed at the edge of the contact zone on the cartilage. The ideal magnitude of r_{corner} appears to be large enough to prevent the stress concentration from developing at the edge of a square-tipped indentor, and small enough to prevent the contact zone from becoming too small, and the resulting stresses in the cartilage too large. The value of r_{corner} used in Model A was chosen to be less than the width of the outer-most element under the indentor (in this model, element width = 0.03125mm) in an effort to keep the contact zone width as close to r=1.25mm as possible.

Model A

r=	**1.25**	**mm**
h=	**2.50**	**mm**
R=	**10.00**	**mm**
r corner=	**0.03**	**mm**
r/h=	**0.50**	
t=	**500**	**sec**

Node	Vertical Stress	Horizontal Stress
1	-1.9997E-02	4.2317E-03
2	-2.7240E-02	4.3235E-03
3	-2.6498E-02	-4.0201E-03
4	-2.5334E-02	-5.5253E-03
5	-2.4953E-02	-6.0935E-03
6	-4.0231E-02	-1.4415E-02
7	-3.9603E-02	-1.6457E-02
8	-3.9010E-02	-1.8146E-02
9	-3.8586E-02	-1.9265E-02
10	-3.8431E-02	-1.9659E-02
11	-6.2336E-02	-4.9925E-03
12	-7.3914E-02	-5.0140E-03
13	-9.3316E-02	-1.6370E-02
14	-1.3430E-01	-9.3802E-04
15	-2.9680E-01	-1.7960E-01
16	1.5449E-02	7.3761E-04
17	4.2023E-04	3.7297E-03
18	4.5686E-04	7.3341E-03
19	2.8696E-04	1.1426E-02
20	7.8661E-06	1.5795E-02

Table A-3
Model A - Matrix Stresses for r_{corner} = 0.03 mm

Model B

r=	1.25	mm
h=	2.50	mm
R=	10.00	mm
r corner=	0.00	mm
r/h=	0.50	
t=	500	sec

Node	Vertical Stress	Horizontal Stress
1	-1.9151E-02	3.9488E-03
2	-2.6512E-02	4.3504E-03
3	-2.7985E-02	-2.2187E-03
4	-2.7304E-02	-3.3994E-03
5	-2.7127E-02	-3.8493E-03
6	-4.2384E-02	-9.3297E-03
7	-4.2224E-02	-1.0711E-02
8	-4.2028E-02	-1.1849E-02
9	-4.1871E-02	-1.2601E-02
10	-4.1810E-02	-1.2865E-02
11	-5.9084E-02	-6.0692E-03
12	-6.7992E-02	-1.1264E-02
13	-7.5903E-02	-8.3264E-03
14	-1.4650E-01	-8.4902E-02
15	-8.2365E-02	1.3720E-01
16	4.8818E-04	-4.0591E-03
17	4.3390E-05	-1.8467E-03
18	3.2762E-04	1.0708E-03
19	2.9695E-04	4.6502E-03
20	1.8000E-05	8.7922E-03

Table A-4
Model B - Matrix Stresses for $r_{corner} = 0$ mm

Model C

r=	**1.25**	**mm**
h=	**2.50**	**mm**
R=	**10.00**	**mm**
r corner=	**0.075**	**mm**
r/h=	**0.50**	
t=	**500**	**sec**

Node	Vertical Stress	Horizontal Stress
1	-1.9201E-02	3.9828E-03
2	-2.6819E-02	4.2884E-03
3	-2.7960E-02	-3.2115E-03
4	-2.7106E-02	-4.5862E-03
5	-2.6840E-02	-5.1048E-03
6	-4.3587E-02	-1.1471E-02
7	-4.3277E-02	-1.3343E-02
8	-4.2920E-02	-1.4922E-02
9	-4.2639E-02	-1.5984E-02
10	-4.2531E-02	-1.6362E-02
11	-5.0095E-02	-9.1132E-03
12	-5.3959E-02	-1.2919E-02
13	-5.7503E-02	-2.2199E-02
14	-6.7327E-02	-2.1990E-02
15	-2.7527E-02	-1.3120E-01
16	1.0583E-04	-1.2359E-03
17	4.0014E-04	1.1677E-03
18	4.7668E-04	4.1237E-03
19	3.2901E-04	7.5712E-03
20	1.1598E-05	1.1379E-02

Table A-5
Model C - Matrix Stresses for r_{corner} = 0.075 mm

B.0 Appendix B

Results recorded at t=500s. Figures B-1 to B-12 show only the location near the indentor edge, since the pore pressures change is negligible beyond this point.

Table B-1 Model A - Material Parameters @ t = 500s

Model A	**r=**	**2.00**	**mm**	**r/h=**	**2.67**	
	h=	**0.75**	**mm**	**t=**	**500**	**sec**
	R=	**20.00**	**mm**			

Note: '-' implies compressive; Stresses & Pore Pressures are measured in MPa

Node	Vertical Stress	Horizontal Stress	Shear Stress	Max Principal Stress	Min Principal Stress	Pore Pressure
1	-2.2838E-02	-3.7101E-03	5.0237E-07	-2.2838E-02	-3.7101E-03	1.7839E-02
2	-2.3591E-02	-2.7928E-03	2.2710E-07	-2.3591E-02	-2.7928E-03	1.7837E-02
3	-2.4680E-02	-1.4400E-03	2.2344E-07	-2.4680E-02	-1.4400E-03	1.7832E-02
4	-2.3255E-02	-3.8352E-03	3.2359E-03	-2.3780E-02	-3.3102E-03	1.4545E-02
5	-2.3944E-02	-3.0446E-03	2.4211E-03	-2.4221E-02	-2.7678E-03	1.4537E-02
6	-2.4691E-02	-2.2979E-03	8.3138E-04	-2.4722E-02	-2.2671E-03	1.4511E-02
7	-1.3370E-02	-2.7089E-03	7.9755E-03	-1.7632E-02	1.5534E-03	5.8281E-03
8	-1.4080E-02	-2.9428E-03	7.4633E-03	-1.7823E-02	8.0043E-04	5.6569E-03
9	-1.8020E-02	-3.7956E-03	9.6419E-03	-2.2889E-02	1.0734E-03	4.5770E-03
10	-1.0117E-03	-1.8740E-03	4.2766E-03	-5.7411E-03	2.8554E-03	2.3214E-03
11	-2.7499E-04	-3.3618E-03	3.2372E-03	-5.4047E-03	1.7679E-03	2.1635E-03
12	8.3837E-04	-3.1885E-03	4.2807E-04	-3.2335E-03	8.8337E-04	1.2539E-03
Node	**Vertical Strain**	**Horizontal Strain**	**Shear Strain**	**Max Principal Strain**	**Min Principal Strain**	**Void Ratio**
1	-4.6256E-02	1.5322E-03	2.5102E-06	-4.6256E-02	1.5322E-03	3.7930
2	-4.8522E-02	3.4376E-03	1.1347E-06	-4.8522E-02	3.4376E-03	3.8000
3	-5.1820E-02	6.2402E-03	1.1164E-06	-5.1820E-02	6.2402E-03	3.8110
4	-4.7060E-02	1.4557E-03	1.6168E-02	-4.8372E-02	2.7673E-03	3.7890
5	-4.9123E-02	3.0896E-03	1.2097E-02	-4.9815E-02	3.7811E-03	3.7950
6	-5.1393E-02	4.5499E-03	4.1540E-03	-5.1470E-02	4.6269E-03	3.8020
7	-2.6980E-02	-3.4628E-02	3.9850E-02	-5.1093E-02	-1.0515E-02	3.8750
8	-2.8655E-02	-8.3136E-04	3.7291E-02	-3.8007E-02	8.5204E-03	3.8730
9	-3.6729E-02	-1.1921E-03	4.8176E-02	-4.8893E-02	1.0972E-02	3.8400
10	-1.4488E-03	-3.6029E-03	2.1368E-02	-1.3264E-02	8.2123E-03	3.9790
11	5.7340E-04	-7.1384E-03	1.6175E-02	-1.2242E-02	5.6772E-03	3.9750
12	2.7583E-03	-7.3019E-03	2.1389E-03	-7.4143E-03	2.8707E-03	3.9870

Table B-2 Model B - Material Parameters @ t = 500s

Model B	r=	2.00	mm	r/h=	2.00	
	h=	1.00	mm	t=	500	sec
	R=	20.00	mm			

Note: '-' implies compressive; Stresses & Pore Pressures are measured in MPa

Node	Vertical Stress	Horizontal Stress	Shear Stress	Max Principal Stress	Min Principal Stress	Pore Pressure
1	-2.2381E-02	-2.6144E-03	8.4584E-08	-2.2381E-02	-2.6144E-03	1.9028E-02
2	-2.3744E-02	-9.1088E-04	3.6501E-07	-2.3744E-02	-9.1088E-04	1.9014E-02
3	-2.4622E-02	2.6527E-04	3.6091E-07	-2.4622E-02	2.6527E-04	1.8993E-02
4	-2.2812E-02	-2.5893E-03	3.4170E-03	-2.3374E-02	-2.0275E-03	1.8527E-02
5	-2.4146E-02	-1.2830E-03	1.7446E-03	-2.4278E-02	-1.1506E-03	1.5776E-02
6	-2.4597E-02	-1.2764E-03	2.9712E-04	-2.4601E-02	-1.2726E-03	1.5701E-02
7	-1.2851E-02	-2.5181E-03	8.0980E-03	-1.7290E-02	1.9212E-03	7.5498E-03
8	-1.4745E-02	-2.8218E-03	7.9333E-03	-1.8707E-02	1.1402E-03	7.0227E-03
9	-2.1012E-02	-3.8289E-03	1.1516E-02	-2.6788E-02	1.9473E-03	5.3727E-03
10	-1.8257E-03	-2.9612E-03	5.4348E-03	-7.8578E-03	3.0709E-03	3.8547E-03
11	-6.4247E-04	-4.8885E-03	3.7706E-03	-7.0927E-03	1.5617E-03	3.2995E-03
12	9.4006E-04	-3.5569E-03	6.9454E-04	-3.6617E-03	1.0449E-03	1.7205E-03

Node	Vertical Strain	Horizontal Strain	Shear Strain	Max Principal Strain	Min Principal Strain	Void Ratio
1	-4.6058E-02	3.3239E-03	4.2263E-07	-4.6058E-02	3.3239E-03	3.8100
2	-5.0193E-02	6.8503E-03	1.8238E-06	-5.0193E-02	6.8503E-03	3.8240
3	-5.2913E-02	9.2624E-03	1.8033E-06	-5.2913E-02	9.2624E-03	3.8340
4	-4.6968E-02	3.5538E-03	1.7073E-02	-4.8371E-02	4.9572E-03	3.8070
5	-5.0830E-02	6.2875E-03	8.7170E-03	-5.1161E-02	6.6182E-03	3.8170
6	-5.2053E-02	6.2077E-03	1.4846E-03	-5.2062E-02	6.2172E-03	3.8190
7	-2.6259E-02	-4.4477E-04	4.0662E-02	-3.7434E-02	1.0730E-02	3.8860
8	-3.0554E-02	-7.6727E-04	3.9639E-02	-4.0452E-02	9.1310E-03	3.8770
9	-4.3238E-02	-3.0972E-04	5.7540E-02	-5.7668E-02	1.4121E-02	3.8220
10	-2.8818E-03	-5.7185E-03	2.7155E-02	-1.7952E-02	9.3512E-03	3.9670
11	1.2935E-04	-1.0479E-02	1.8840E-02	-1.5985E-02	5.6358E-03	3.9660
12	2.9240E-03	-8.3107E-03	3.4703E-03	-8.5726E-03	3.1859E-03	3.9890

Table B-3 Model C - Material Parameters @ t = 500s

Model C r= 2.00 mm   r/h= 1.60

h= 1.25 mm   t= 500 sec

R= 20.00 mm

Note: '-' implies compressive; Stresses & Pore Pressures are measured in MPa

Node	Vertical Stress	Horizontal Stress	Shear Stress	Max Principal Stress	Min Principal Stress	Pore Pressure
1	-2.2130E-02	-1.4600E-03	-1.2861E-07	-2.2130E-02	-1.4600E-03	1.9993E-02
2	-2.3884E-02	7.5732E-04	3.3496E-07	-2.3884E-02	7.5732E-04	1.9938E-02
3	-2.4414E-02	1.5663E-03	3.2872E-07	-2.4414E-02	1.5663E-03	1.9893E-02
4	-2.2291E-02	-1.2540E-03	3.5274E-03	-2.2867E-02	-6.7829E-04	1.6926E-02
5	-2.4331E-02	2.0491E-03	1.1398E-03	-2.4380E-02	2.0983E-03	1.6785E-02
6	-2.4599E-02	-5.8042E-04	-1.0824E-04	-2.4599E-02	-5.7993E-04	1.6653E-02
7	-1.2253E-02	-2.1925E-03	8.1085E-03	-1.6765E-02	2.3193E-03	9.1040E-03
8	-1.5487E-02	-2.4414E-03	8.4608E-03	-1.9647E-02	1.7191E-03	8.1620E-03
9	-2.4064E-02	-3.7113E-03	1.3268E-02	-3.0609E-02	2.8335E-03	5.9987E-03
10	-2.4952E-03	-3.3800E-03	6.1535E-03	-9.1070E-03	3.2318E-03	5.3539E-03
11	-1.0917E-03	-5.5471E-03	4.4248E-03	-8.2733E-03	1.6345E-03	4.2964E-03
12	1.0268E-03	-3.6039E-03	1.0790E-03	-3.8430E-03	1.2659E-03	2.0815E-03
Node	**Vertical Strain**	**Horizontal Strain**	**Shear Strain**	**Max Principal Strain**	**Min Principal Strain**	**Void Ratio**
1	-4.6346E-02	5.2944E-03	-6.4262E-07	-4.6346E-02	5.2944E-03	3.8270
2	-5.1684E-02	9.8769E-03	1.6737E-06	-5.1684E-02	9.8769E-03	3.8450
3	-5.3397E-02	1.1510E-02	1.6425E-06	-5.3397E-02	1.1510E-02	3.8530
4	-4.6788E-02	5.7690E-03	1.7625E-02	-4.8226E-02	7.2073E-03	3.8280
5	-5.2322E-02	8.9766E-03	5.6950E-03	-5.2454E-02	9.1086E-03	3.8360
6	-5.2657E-02	7.3478E-03	-5.4085E-04	-5.2658E-02	7.3490E-03	3.8300
7	-2.5424E-02	-2.9064E-04	4.0515E-02	-3.6696E-02	1.0981E-02	3.8980
8	-3.2661E-02	-7.0289E-05	4.2275E-02	-4.3055E-02	1.0324E-02	3.8820
9	-4.9882E-02	9.6626E-04	6.6293E-02	-6.6232E-02	1.7316E-02	3.8030
10	-4.3168E-03	-6.5273E-03	3.0746E-02	-2.0835E-02	9.9906E-03	3.9630
11	-8.4532E-04	-1.1976E-02	2.2109E-02	-1.8787E-02	5.9657E-03	3.9620
12	2.9497E-03	-8.6193E-03	5.3914E-03	-9.2166E-03	3.5470E-03	3.9920

Table B-4 Model D - Material Parameters @ t = 500s

Model D r= 2.00 mm r/h= 1.33

h= 1.50 mm t= 500 sec

R= 20.00 mm

Note: '-' implies compressive; Stresses & Pore Pressures are measured in MPa

Node	Vertical Stress	Horizontal Stress	Shear Stress	Max Principal Stress	Min Principal Stress	Pore Pressure
1	-2.2000E-02	-2.5061E-04	-3.1834E-07	-2.2000E-02	-2.5061E-04	2.0671E-02
2	-2.3968E-02	2.1102E-03	1.0477E-07	-2.3968E-02	2.1102E-03	2.0562E-02
3	-2.4117E-02	2.4131E-03	2.3261E-07	-2.4117E-02	2.4131E-03	2.0502E-02
4	-2.1695E-02	-1.5627E-05	3.6181E-03	-2.2283E-02	5.7226E-04	1.7763E-02
5	-2.4596E-02	1.4101E-03	7.4142E-04	-2.4617E-02	1.4312E-03	1.7513E-02
6	-2.4761E-02	-1.5277E-04	-3.8613E-04	-2.4767E-02	-1.4671E-04	1.7339E-02
7	-1.1714E-02	-1.7918E-03	8.0122E-03	-1.6177E-02	2.6709E-03	1.0397E-02
8	-1.6263E-02	-1.9311E-03	8.9549E-03	-2.0566E-02	2.3721E-03	9.0636E-03
9	-2.7126E-02	-3.5301E-03	1.4897E-02	-3.4331E-02	3.6749E-03	6.4670E-03
10	-3.0537E-03	-3.4120E-03	6.5662E-03	-9.8015E-03	3.3358E-03	6.6746E-03
11	-1.6448E-03	-5.7775E-03	5.1306E-03	-9.2422E-03	1.8199E-03	5.1177E-03
12	1.0617E-03	-3.5155E-03	1.5060E-03	-3.9666E-03	1.5128E-03	1.8994E-03

Node	Vertical Strain	Horizontal Strain	Shear Strain	Max Principal Strain	Min Principal Strain	Void Ratio
1	-4.6930E-02	7.4058E-03	-1.5906E-06	-4.6930E-02	7.4058E-03	3.8440
2	-5.2830E-02	1.2321E-02	5.2347E-07	-5.2830E-02	1.2321E-02	3.8630
3	-5.3365E-02	1.2915E-02	1.1622E-06	-5.3365E-02	1.2915E-02	3.8660
4	-4.6416E-02	7.7452E-03	1.8078E-02	-4.7885E-02	9.2139E-03	3.8490
5	-5.3768E-02	1.1203E-02	3.7045E-03	-5.3821E-02	1.1256E-02	3.8510
6	-5.3368E-02	8.1113E-03	-1.9293E-03	-5.3383E-02	8.1264E-03	3.8360
7	-2.4728E-02	5.9730E-05	4.0034E-02	-3.5877E-02	1.1209E-02	3.9110
8	-3.4836E-02	9.6900E-04	4.4744E-02	-4.5587E-02	1.1720E-02	3.8870
9	-5.6511E-02	2.4375E-03	7.4432E-02	-7.4511E-02	2.0437E-02	3.7850
10	-5.6838E-03	-6.5791E-03	3.2808E-02	-2.2542E-02	1.0279E-02	3.9610
11	-2.1913E-03	-1.2516E-02	2.5636E-02	-2.1172E-02	6.4649E-03	3.9620
12	2.8482E-03	-8.5871E-03	7.5250E-03	-9.7140E-03	3.9751E-03	3.9960

Model E r= 2.00 mm r/h= 1.14

h= 1.75 mm t= 500 sec

R= 20.00 mm

Note: '-' implies compressive; Stresses & Pore Pressures are measured in MPa

Node	Vertical Stress	Horizontal Stress	Shear Stress	Max Principal Stress	Min Principal Stress	Pore Pressure
1	-2.1895E-02	9.6622E-04	-5.2127E-07	-2.1895E-02	9.6622E-04	2.1074E-02
2	-2.4028E-02	3.1349E-03	-1.3525E-07	-2.4028E-02	3.1349E-03	2.0939E-02
3	-2.3824E-02	2.8722E-03	1.6441E-07	-2.3824E-02	2.8722E-03	2.0896E-02
4	-2.1071E-02	1.0649E-03	3.7054E-03	-2.1675E-02	1.6687E-03	1.8329E-02
5	-2.4962E-02	2.3900E-03	5.4808E-04	-2.4973E-02	2.4010E-03	1.8002E-02
6	-2.5057E-02	5.3463E-05	-5.7419E-04	-2.5070E-02	6.6586E-05	1.7822E-02
7	-1.1286E-02	-1.3619E-03	7.8431E-03	-1.5605E-02	2.9570E-03	1.1402E-02
8	-1.7027E-02	-1.3833E-03	9.4071E-03	-2.1439E-02	3.0290E-03	9.7571E-03
9	-3.0138E-02	-3.3471E-03	1.6397E-02	-3.7916E-02	4.4305E-03	6.8147E-03
10	-3.5519E-03	-3.2376E-03	6.7673E-03	-1.0164E-02	3.3744E-03	7.7595E-03
11	-2.2960E-03	-5.7743E-03	5.8435E-03	-1.0132E-02	2.0617E-03	5.7731E-03
12	1.0469E-03	-3.3861E-03	1.9451E-03	-4.1185E-03	1.7793E-03	2.5171E-03
Node	**Vertical Strain**	**Horizontal Strain**	**Shear Strain**	**Max Principal Strain**	**Min Principal Strain**	**Void Ratio**
1	-4.7575E-02	9.5398E-03	-2.6046E-06	-4.7575E-02	9.5398E-03	3.8610
2	-5.3691E-02	1.4171E-02	-6.7580E-07	-5.3691E-02	1.4171E-02	3.8760
3	-5.3067E-02	1.3630E-02	8.2147E-07	-5.3067E-02	1.3630E-02	3.8740
4	-4.5903E-02	9.3992E-03	1.8514E-02	-4.7411E-02	1.0908E-02	3.8690
5	-5.5246E-02	1.3088E-02	2.7385E-03	-5.5273E-02	1.3115E-02	3.8620
6	-5.4171E-02	8.5618E-03	-2.8690E-03	-5.4204E-02	8.5946E-03	3.8370
7	-2.4254E-02	5.3892E-04	3.9189E-02	-3.5044E-02	1.1329E-02	3.9220
8	-3.6946E-02	2.1356E-03	4.7003E-02	-4.7969E-02	1.3159E-02	3.8910
9	-6.2982E-02	3.9490E-03	8.1928E-02	-8.2413E-02	2.3380E-02	3.7650
10	-7.0014E-03	-6.2161E-03	3.3813E-02	-2.3520E-02	1.0302E-02	3.9630
11	-3.8071E-03	-1.2497E-02	2.9197E-02	-2.3383E-02	7.0793E-03	3.9620
12	2.6670E-03	-8.4079E-03	9.7188E-03	-1.0238E-02	4.4969E-03	3.9990

Table B-5 Model E - Material Parameters @ t = 500s

Model F r= 2.00 mm r/h= 1.00

h= 2.00 mm t= 500 sec

R= 20.00 mm

Note: '-' implies compressive; Stresses & Pore Pressures are measured in MPa

Node	Vertical Stress	Horizontal Stress	Shear Stress	Max Principal Stress	Min Principal Stress	Pore Pressure
1	-2.1759E-02	2.1278E-03	-7.1995E-07	-2.1759E-02	2.1278E-03	2.1243E-02
2	-2.4117E-02	3.8861E-03	-2.7362E-07	-2.4117E-02	3.8861E-03	2.1164E-02
3	-2.3591E-02	3.0441E-03	1.3565E-07	-2.3591E-02	3.0441E-03	2.1184E-02
4	-2.0460E-02	1.9888E-03	3.7870E-03	-2.1082E-02	2.6104E-03	1.8659E-02
5	-2.5406E-02	3.1950E-03	5.1758E-04	-2.5415E-02	3.2044E-03	1.8834E-02
6	-2.5437E-02	7.9494E-05	-7.0701E-04	-2.5457E-02	9.9069E-05	1.8197E-02
7	-1.0971E-02	-9.2881E-04	7.6348E-03	-1.5088E-02	3.1880E-03	1.2146E-02
8	-1.7740E-02	-8.5183E-04	9.8279E-03	-2.2253E-02	3.6613E-03	1.0298E-02
9	-3.3067E-02	-3.1954E-03	1.7772E-02	-4.1346E-02	5.0835E-03	7.0882E-03
10	-4.0120E-03	-2.9573E-03	6.8304E-03	-1.0335E-02	3.3661E-03	8.6163E-03
11	-3.0079E-03	-5.6412E-03	6.5427E-03	-1.0998E-02	2.3493E-03	6.2994E-03
12	1.0012E-03	-3.2617E-03	2.3784E-03	-4.3240E-03	2.0635E-03	2.6389E-03
Node	**Vertical Strain**	**Horizontal Strain**	**Shear Strain**	**Max Principal Strain**	**Min Principal Strain**	**Void Ratio**
1	-4.8113E-02	1.1564E-02	-3.5973E-06	-4.8113E-02	1.1564E-02	3.8780
2	-5.4416E-02	1.5543E-02	-1.3671E-06	-5.4416E-02	1.5543E-02	3.8860
3	-5.2689E-02	1.3853E-02	6.7781E-07	-5.2689E-02	1.3853E-02	3.8780
4	-4.5320E-02	1.0765E-02	1.8922E-02	-4.6873E-02	1.2318E-02	3.8870
5	-5.6746E-02	1.4707E-02	2.5861E-03	-5.6769E-02	1.4730E-02	3.8690
6	-5.5007E-02	8.7404E-03	-3.5326E-03	-5.5056E-02	8.7893E-03	3.8350
7	-2.3992E-02	1.0964E-03	3.8148E-02	-3.4277E-02	1.1381E-02	3.9330
8	-3.8897E-02	3.2946E-03	4.9106E-02	-5.0172E-02	1.4570E-02	3.8940
9	-6.9216E-02	5.4106E-03	8.8800E-02	-8.9900E-02	2.6094E-02	3.7460
10	-8.2680E-03	-5.6333E-03	3.4129E-02	-2.4066E-02	1.0165E-02	3.9650
11	-5.5708E-03	-1.2149E-02	3.2691E-02	-2.5533E-02	7.8132E-03	3.9610
12	2.4624E-03	-8.1874E-03	1.1884E-02	-1.0841E-02	5.1163E-03	4.0010

Table B-6 Model F - Material Parameters @ t = 500s

Model G r= 2.00 mm r/h= 0.89
h= 2.25 mm t= 500 sec
R= 20.00 mm

Note: '-' implies compressive; Stresses & Pore Pressures are measured in MPa

Node	Vertical Stress	Horizontal Stress	Shear Stress	Max Principal Stress	Min Principal Stress	Pore Pressure
1	-2.1572E-02	3.1874E-03	-8.9054E-07	-2.1572E-02	3.1874E-03	2.1230E-02
2	-2.4265E-02	4.4376E-03	-2.9474E-07	-2.4265E-02	4.4376E-03	2.1328E-02
3	-2.3428E-02	3.0163E-03	1.3325E-07	-2.3428E-02	3.0163E-03	2.1464E-02
4	-1.9886E-02	2.7763E-03	3.8571E-03	-2.0524E-02	3.4148E-03	1.8801E-02
5	-2.5897E-02	3.8659E-03	6.0569E-04	-2.5909E-02	3.8782E-03	1.8593E-02
6	-2.5859E-02	-4.0168E-05	-8.1029E-04	-2.5884E-02	-1.4763E-05	1.8551E-02
7	-1.0753E-02	-5.0516E-04	7.4134E-03	-1.4641E-02	3.3827E-03	1.2677E-02
8	-1.8382E-02	-3.6357E-04	1.0230E-02	-2.3004E-02	4.2588E-03	1.0742E-02
9	-3.5902E-02	-3.0846E-03	1.9030E-02	-4.4621E-02	5.6341E-03	7.3291E-03
10	-4.4401E-03	-2.6260E-03	6.8095E-03	-1.0403E-02	3.3366E-03	9.2791E-03
11	-3.7386E-03	-5.4390E-03	7.2180E-03	-1.1857E-02	2.6791E-03	6.7367E-03
12	9.4456E-04	-3.1560E-03	2.7905E-03	-4.5685E-03	2.3570E-03	2.7277E-03
Node	**Vertical Strain**	**Horizontal Strain**	**Shear Strain**	**Max Principal Strain**	**Min Principal Strain**	**Void Ratio**
1	-4.8468E-02	1.3388E-02	-4.4497E-06	-4.8468E-02	1.3388E-02	3.8940
2	-5.5127E-02	1.6580E+02	-1.4727E-06	-5.5127E-02	1.6580E+02	3.8930
3	-5.2320E-02	1.3745E-02	6.6582E-07	-5.2320E-02	1.3745E-02	3.8790
4	-4.4717E-02	1.1899E-02	1.9272E-02	-4.6312E-02	1.3494E-02	3.9030
5	-5.8241E-02	1.6114E-02	3.0264E-03	-5.8272E-02	1.6145E-02	3.8740
6	-5.5820E-02	8.6822E-03	-4.0487E-03	-5.5883E-02	8.7457E-03	3.8300
7	-2.3903E-02	1.6985E-03	3.7042E-02	-3.3616E-02	1.1412E-02	3.9410
8	-4.0642E-02	4.3726E-03	5.1115E-02	-5.2190E-02	1.5921E-02	3.8970
9	-7.5196E-02	6.7908E-03	9.5085E-02	-9.6978E-02	2.8573E-02	3.7260
10	-9.4718E-03	-4.9398E-03	3.4024E-02	-2.4368E-02	9.9565E-03	3.9680
11	-7.3726E-03	-1.1621E-02	3.6065E-02	-2.7654E-02	8.6604E-03	3.9610
12	2.2772E-03	-7.9670E-03	1.3943E-02	-1.1496E-02	5.8060E-03	4.0020

Table B-7 Model G - Material Parameters @ t = 500s

Model H r= 2.00 mm r/h= 0.80

h= 2.50 mm t= 500 sec

R= 20.00 mm

Note: '-' implies compressive; Stresses & Pore Pressures are measured in MPa

Node	Vertical Stress	Horizontal Stress	Shear Stress	Max Principal Stress	Min Principal Stress	Pore Pressure
1	-2.1337E-02	4.1230E-03	-1.0196E-06	-2.1337E-02	4.1230E-03	2.1090E-02
2	-2.4482E-02	4.8546E-03	-2.1607E-07	-2.4482E-02	4.8546E-03	2.1509E-02
3	-2.3244E-02	2.7470E-03	1.7907E-07	-2.3244E-02	2.7470E-03	2.1815E-02
4	-1.9360E-02	3.4497E-03	3.9120E-03	-2.0012E-02	4.1020E-03	1.8806E-02
5	-2.6412E-02	4.4366E-03	7.7526E-04	-2.6431E-02	4.4561E-03	1.8849E-02
6	-2.6284E-02	-2.8415E-04	-9.0426E-04	-2.6315E-02	-2.5274E-04	1.8959E-02
7	-1.0610E-02	-9.7453E-05	7.1968E-03	-1.4266E-02	3.5582E-03	1.3046E-02
8	-1.8943E-02	7.0742E-05	1.0623E-02	-2.3692E-02	4.8197E-03	1.1138E-02
9	-3.8649E-02	-3.0064E-03	2.0173E-02	-4.7745E-02	6.0897E-03	7.5722E-03
10	-4.8371E-03	-2.2741E-03	6.7422E-03	-1.0419E-02	3.3073E-03	9.7879E-03
11	-4.4523E-03	-5.2071E-03	7.8620E-03	-1.2701E-02	3.0414E-03	7.1184E-03
12	8.9381E-04	-3.0561E-03	3.1619E-03	-4.8092E-03	2.6469E-03	2.7974E-03
Node	**Vertical Strain**	**Horizontal Strain**	**Shear Strain**	**Max Principal Strain**	**Min Principal Strain**	**Void Ratio**
1	-4.8632E-02	1.4973E-02	-5.0944E-06	-4.8632E-02	1.4973E-02	3.9080
2	-5.5891E-02	1.7402E-02	-1.0796E-06	-5.5891E-02	1.7402E-02	3.8970
3	-5.1964E-02	1.3406E-02	7.3024E-07	-5.1964E-02	1.3406E-02	3.8770
4	-4.4130E-02	1.2855E-02	1.9547E-02	-4.5760E-02	1.4485E-02	3.9170
5	-5.9714E-02	1.7355E-02	3.8736E-02	-6.4308E-02	2.1949E-02	3.8780
6	-5.6511E-02	8.4040E-03	-4.5182E-03	-5.6590E-02	8.4825E-03	3.8240
7	-2.3942E-02	2.3215E-03	3.5960E-02	-3.3075E-02	1.1455E-02	3.9490
8	-4.2166E-02	5.3351E-03	5.3079E-02	-5.4031E-02	1.7200E-02	3.8990
9	-8.0941E-02	8.1049E-03	1.0080E-01	-1.0367E-01	3.0831E-02	3.7060
10	-1.0602E-02	-4.1988E-03	3.3688E-02	-2.4546E-02	9.7452E-03	3.9710
11	-9.1261E-03	-1.1012E-02	3.9283E-02	-2.9733E-02	9.5951E-03	3.9600
12	2.1372E-03	-7.7308E-03	1.5798E-02	-1.2110E-02	6.5166E-03	4.0020

Table B-8 Model H - Material Parameters @ t = 500s

Table B-9 Model I - Material Parameters @ t = 500s

Model I r= 2.00 mm r/h= 0.73

h= 2.75 mm t= 500 sec

R= 20.00 mm

Note: '-' implies compressive; Stresses & Pore Pressures are measured in MPa

Node	Vertical Stress	Horizontal Stress	Shear Stress	Max Principal Stress	Min Principal Stress	Pore Pressure
1	-2.0986E-02	4.8910E-03	-1.0814E-06	-2.0986E-02	4.8910E-03	2.0706E-02
2	-2.4792E-02	5.1991E-03	-7.8798E-08	-2.4792E-02	5.1991E-03	2.1543E-02
3	-2.3377E-02	2.6489E-03	1.5831E-07	-2.3377E-02	2.6489E-03	2.2032E-02
4	-1.8817E-02	3.9975E-03	3.9345E-03	-1.9476E-02	4.6570E-03	1.8586E-02
5	-2.6930E-02	4.9213E-03	1.0485E-03	-2.6964E-02	4.9558E-03	1.8942E-02
6	-2.6853E-02	-5.3895E-04	-9.4693E-04	-2.6887E-02	-5.0492E-04	1.9178E-02
7	-1.0512E-02	3.0401E-04	6.9673E-03	-1.3924E-02	3.7159E-03	1.3229E-02
8	-1.9433E-02	4.6382E-04	1.0987E-02	-2.4306E-02	5.3372E-03	1.1442E-02
9	-4.1314E-02	-3.0329E-03	2.1257E-02	-5.0778E-02	6.4311E-03	7.7175E-03
10	-5.2193E-03	-1.8876E-03	6.6369E-03	-1.0396E-02	3.2893E-03	1.0147E-02
11	-5.1821E-03	-4.9220E-03	8.5017E-03	-1.3555E-02	3.4506E-03	7.4704E-03
12	8.4021E-04	-3.1104E-03	3.6141E-03	-5.2538E-03	2.9836E-03	2.9037E-03
Node	**Vertical Strain**	**Horizontal Strain**	**Shear Strain**	**Max Principal Strain**	**Min Principal Strain**	**Void Ratio**
1	-4.8430E-02	1.6219E-02	-5.4034E-06	-4.8430E-02	1.6219E-02	3.9210
2	-5.6799E-02	1.8127E-02	-3.9372E-07	-5.6799E-02	1.8127E-02	3.8990
3	-5.1949E-02	1.3071E-02	7.9100E-07	-5.1949E-02	1.3071E-02	3.8740
4	-4.3405E-02	1.3593E-02	1.9659E-02	-4.5053E-02	1.5241E-02	3.9290
5	-6.1138E-02	1.8437E-02	5.2387E-03	-6.1224E-02	1.8523E-02	3.8800
6	-5.7580E-02	8.1609E-03	-4.7314E-03	-5.7665E-02	8.2459E-03	3.8170
7	-2.4041E-02	2.9809E-03	3.4812E-02	-3.2564E-02	1.1504E-02	3.9560
8	-4.3499E-02	6.2087E-03	5.4895E-02	-5.5673E-02	1.8383E-02	3.9010
9	-8.6470E-02	9.1685E-03	1.0620E-01	-1.1011E-01	3.2808E-02	3.6860
10	-1.1693E-02	-3.3693E-03	3.3162E-02	-2.4626E-02	9.5642E-03	3.9730
11	-1.0915E-02	-1.0265E-02	4.2480E-02	-3.1832E-02	1.0652E-02	3.9600
12	2.0632E-03	-7.8064E-03	1.8058E-02	-1.3161E-02	7.4180E-03	4.0010

Table B-10 Model J - Material Parameters @ t = 500s

Model J r= **2.00** mm r/h= **0.67**
h= **3.00** mm t= **500** sec
R= **20.00** mm

Note: '-' implies compressive; Stresses & Pore Pressures are measured in MPa

Node	Vertical Stress	Horizontal Stress	Shear Stress	Max Principal Stress	Min Principal Stress	Pore Pressure
1	-2.0568E-02	5.5178E-03	-1.0894E-06	-2.0568E-02	5.5178E-03	2.0230E-02
2	-2.5183E-02	5.5076E-03	9.2907E-08	-2.5183E-02	5.5076E-03	2.1565E-02
3	-2.3544E-02	2.4277E-03	1.7065E-07	-2.3544E-02	2.4277E-03	2.2256E-02
4	-1.8293E-02	4.4543E-03	3.9297E-03	-1.8953E-02	5.1140E-03	1.8269E-02
5	-2.7452E-02	5.3941E-03	1.3728E-03	-2.7509E-02	5.4514E-03	1.9020E-02
6	-2.7470E-02	-7.8812E-04	-9.7559E-04	-2.7506E-02	-7.5250E-04	1.9411E-02
7	-1.0447E-02	6.8744E-04	6.7461E-03	-1.3626E-02	3.8669E-03	1.3302E-02
8	-1.9865E-02	8.0826E-04	1.1351E-02	-2.4881E-02	5.8239E-03	1.1715E-02
9	-4.3841E-02	-3.1354E-03	2.2318E-02	-5.3693E-02	6.7166E-03	7.8794E-03
10	-5.5730E-03	-1.4983E-03	6.5165E-03	-1.0363E-02	3.2919E-03	1.0400E-02
11	-5.8980E-03	-4.6439E-03	9.1174E-03	-1.4410E-02	3.8680E-03	7.7883E-03
12	7.4703E-04	-3.3090E-03	4.0874E-03	-5.8438E-03	3.2819E-03	2.9759E-03
Node	**Vertical Strain**	**Horizontal Strain**	**Shear Strain**	**Max Principal Strain**	**Min Principal Strain**	**Void Ratio**
1	-4.7982E-02	1.7188E-02	-5.4433E-06	-4.7982E-02	1.7188E-02	3.9330
2	-5.7857E-02	1.8817E-02	4.6419E-07	-5.7857E-02	1.8817E-02	3.9010
3	-5.2148E-02	1.2736E-02	8.5267E-07	-5.2148E-02	1.2736E-02	3.8700
4	-4.2643E-02	1.4188E-02	1.9635E-02	-4.4291E-02	1.5836E-02	3.9400
5	-6.2545E-02	1.9440E-02	6.8592E-03	-6.2688E-02	1.9583E-02	3.8820
6	-5.8711E-02	7.9482E-03	-4.8746E-03	-5.8800E-02	8.0372E-03	3.8090
7	-2.4177E-02	3.6392E-03	3.3707E-02	-3.2120E-02	1.1582E-02	3.9620
8	-4.4678E-02	6.9703E-03	5.6715E-02	-5.7208E-02	1.9500E-02	3.9030
9	-9.1681E-02	1.0012E-02	1.1150E-01	-1.1629E-01	3.4620E-02	3.6670
10	-1.2707E-02	-2.5275E-03	3.2560E-02	-2.4674E-02	9.4398E-03	3.9760
11	-1.2659E-02	-9.5254E-03	4.5556E-02	-3.3924E-02	1.1740E-02	3.9590
12	1.9724E-03	-8.1608E-03	2.0423E-02	-1.4494E-02	8.3051E-03	3.9980

Model K r= 2.00 mm r/h= 0.50

h= 4.00 mm t= 500 sec

R= 20.00 mm

Note: '-' implies compressive; Stresses & Pore Pressures are measured in MPa

Node	Vertical Stress	Horizontal Stress	Shear Stress	Max Principal Stress	Min Principal Stress	Pore Pressure
1	-1.8661E-02	6.9461E-03	-7.5223E-07	-1.8661E-02	6.9461E-03	1.8049E-02
2	-2.7241E-02	6.7428E-03	6.1675E-07	-2.7241E-02	6.7428E-03	2.2147E-02
3	-2.4713E-02	1.5492E-03	2.4269E-07	-2.4713E-02	1.5492E-03	2.3943E-02
4	-1.6465E-02	5.6122E-03	3.7206E-03	-1.7075E-02	6.2224E-03	1.6626E-02
5	-2.9431E-02	6.9226E-03	2.9146E-03	-2.9663E-02	7.1548E-03	1.9713E-02
6	-3.0084E-02	-1.7931E-03	-1.0621E-03	-3.0124E-02	-1.7533E-03	2.1057E-02
7	-1.0318E-02	1.9817E-03	5.9835E-03	-1.2749E-02	4.4122E-03	1.2961E-02
8	-2.1080E-02	1.8165E-03	1.2727E-02	-2.6750E-02	7.4866E-03	1.2827E-02
9	-5.3094E-02	-3.9357E-03	2.6245E-02	-6.4472E-02	7.4426E-03	8.7296E-03
10	-6.6791E-03	-6.1279E-05	6.0128E-03	-1.0233E-02	3.4929E-03	1.0723E-02
11	-8.3219E-03	-3.6683E-03	1.1214E-02	-1.7448E-02	5.4578E-03	8.9564E-03
12	4.5433E-04	-4.5698E-03	5.7928E-03	-8.3718E-03	4.2563E-03	3.2849E-03
Node	**Vertical Strain**	**Horizontal Strain**	**Shear Strain**	**Max Principal Strain**	**Min Principal Strain**	**Void Ratio**
1	-4.4918E-02	1.9056E-02	-3.7586E-06	-4.4918E-02	1.9056E-02	3.9660
2	-6.3147E-02	2.1756E-02	3.0816E-06	-6.3147E-02	2.1756E-02	3.9040
3	-5.4025E-02	1.1586E-02	1.2126E-06	-5.4025E-02	1.1586E-02	3.8500
4	-3.9594E-02	1.5560E-02	1.8590E-02	-4.1118E-02	1.7084E-02	3.9690
5	-6.7851E-02	2.2971E-02	1.4563E-02	-6.8431E-02	2.3551E-02	3.8890
6	-6.3561E-02	7.1184E-03	-5.3069E-03	-6.3660E-02	7.2179E-03	3.7780
7	-2.4725E-02	6.0045E-03	2.9897E-02	-3.0797E-02	1.2076E-02	3.9790
8	-4.8094E-02	9.1070E-03	6.3593E-02	-6.2260E-02	2.3273E-02	3.9100
9	1.1060E-01	1.2247E-02	1.3110E-01	-2.0522E-02	1.4337E-01	3.5940
10	-1.5922E-02	6.1069E-04	3.0044E-02	-2.4802E-02	9.4906E-03	3.9850
11	-1.8574E-02	-6.9478E-03	5.6031E-02	-4.1373E-02	1.5851E-02	3.9560
12	2.0199E-03	-1.0532E-02	2.8944E-02	-2.0030E-02	1.1518E-02	3.9820

Table B-11 Model K - Material Parameters @ t = 500s

Table B-12 Model L - Material Parameters @ t = 500s

Model L r= **2.00** **mm** r/h= **0.40**

h= **5.00** **mm** t= **500** **sec**

R= **20.00** **mm**

Note: '-' implies compressive; Stresses & Pore Pressures are measured in MPa

Node	Vertical Stress	Horizontal Stress	Shear Stress	Max Principal Stress	Min Principal Stress	Pore Pressure
1	-1.6745E-02	7.2445E-03	-2.8047E-07	-1.6745E-02	7.2445E-03	1.5754E-02
2	-2.9676E-02	8.1996E-03	-2.2558E-07	-2.9676E-02	8.1996E-03	2.3137E-02
3	-2.6487E-02	8.9165E-04	2.9820E-07	-2.6487E-02	8.9165E-04	2.6382E-02
4	-1.4937E-02	6.0168E-03	3.3262E-03	-1.5452E-02	6.5321E-03	1.4735E-02
5	-3.1142E-02	8.2967E-03	4.5710E-03	-3.1665E-02	8.8196E-03	2.0697E-02
6	-3.3011E-02	-2.6802E-03	-1.1261E-03	-3.3053E-02	-2.6384E-03	2.3287E-02
7	-1.0185E-02	2.8831E-03	5.3118E-03	-1.2072E-02	4.7698E-03	1.2068E-02
8	-2.1829E-02	2.5172E-03	1.3907E-02	-2.8138E-02	8.8262E-03	1.3974E-02
9	-6.1456E-02	-5.1003E-03	2.9989E-02	-7.4428E-02	7.8720E-03	9.7539E-03
10	-7.3735E-03	1.0973E-03	5.4950E-03	-1.0076E-02	3.7997E-03	1.0385E-02
11	-1.0105E-02	-2.8469E-03	1.2790E-02	-1.9771E-02	6.8189E-03	1.0103E-02
12	2.8117E-04	-6.2430E-03	7.2908E-03	-1.0968E-02	5.0064E-03	3.6716E-03

Node	Vertical Strain	Horizontal Strain	Shear Strain	Max Principal Strain	Min Principal Strain	Void Ratio
1	-4.1029E-02	1.8904E-02	-1.4014E-06	-4.1029E-02	1.8904E-02	3.9840
2	-6.9400E-02	2.5224E-02	-1.1271E-06	-6.9400E-02	2.5224E-02	3.9070
3	-5.7353E-02	1.1046E-02	1.4900E-06	-5.7353E-02	1.1046E-02	3.8300
4	-3.6575E-02	1.5773E-02	1.6619E-02	-3.7862E-02	1.7060E-02	3.9850
5	-7.2550E-02	2.5979E-02	2.2839E-02	-7.3856E-02	2.7285E-02	3.8970
6	-6.9194E-02	6.5807E-03	-5.6264E-03	-6.9298E-02	6.6850E-03	3.7480
7	-2.4894E-02	7.7544E-03	2.6541E-02	-2.9608E-02	1.2468E-02	3.9890
8	-5.0361E-02	1.0462E-02	6.9489E-02	-6.6124E-02	2.6225E-02	3.9180
9	-1.2750E-01	1.3327E-02	1.4980E-01	-1.5989E-01	4.5715E-02	3.5280
10	-1.7980E-02	3.1822E-03	2.7456E-02	-2.4731E-02	9.9337E-03	3.9910
11	-2.3020E-02	-4.8880E-03	6.3905E-02	-4.7168E-02	1.9260E-02	3.9560
12	2.4958E-03	-1.3803E-02	3.6429E-02	-2.5608E-02	1.4301E-02	3.9640

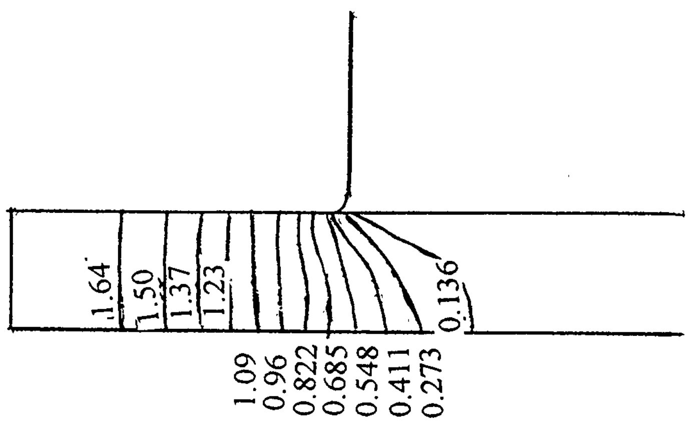

Figure B-1
h=0.75mm
r/h=2.67
x 100 MPa
Model A - Pore Pressures @ t = 500s

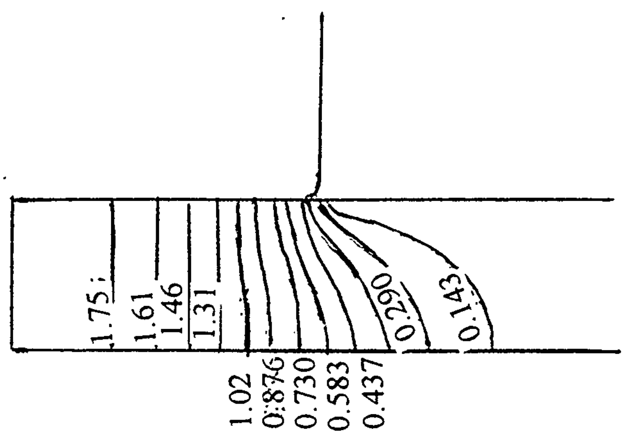

Figure B-2
h=1mm
r/h=2.00
x 100 MPa
Model B - Pore Pressures @ t = 500s

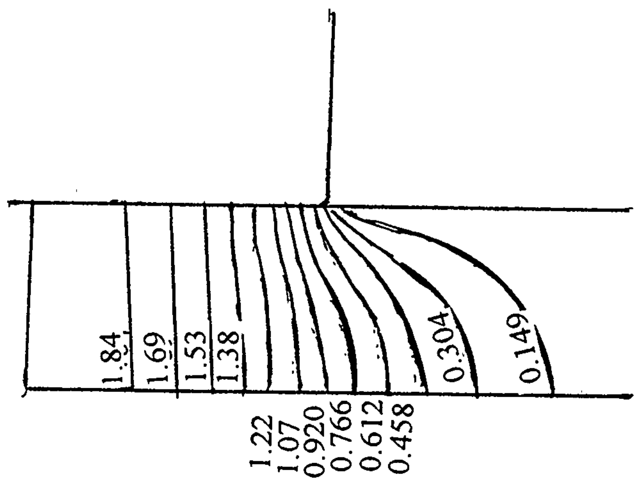

Figure B-3
h=1.25mm
r/h=1.60
x 100 MPa

Model C - Pore Pressures @ t = 500s

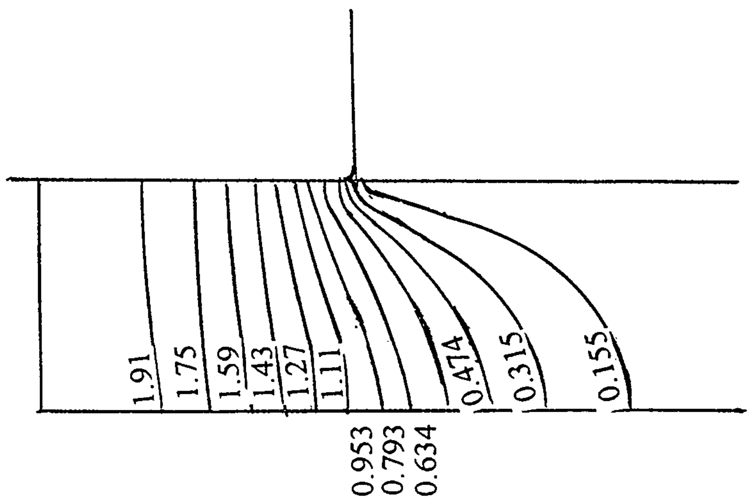

Figure B-4
h=1.50mm
r/h=1.33
x 100 MPa
Model D - Pore Pressures @ t = 500s

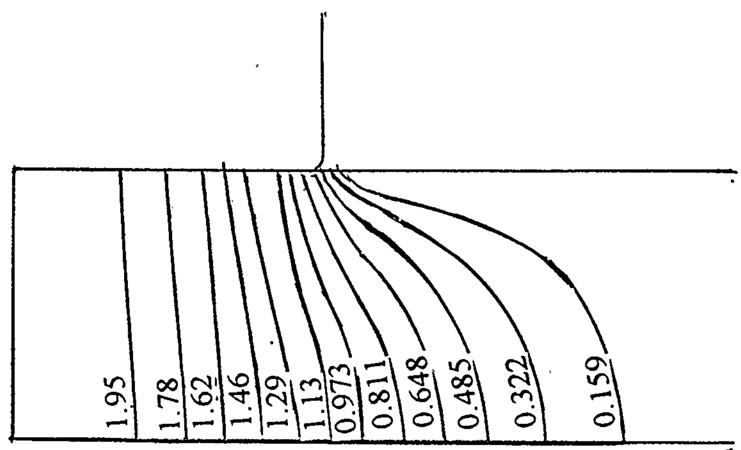

Figure B-5
h=1.75mm
r/h=1.14
x 100 MPa
Model E - Pore Pressures @ t = 500s

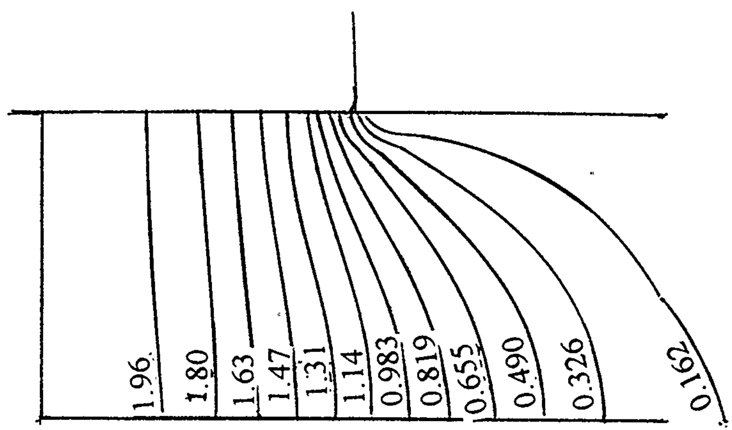

Figure B-6
h=2.00mm
r/h=1.00
x 100 MPa
Model F - Pore Pressures @ t = 500s

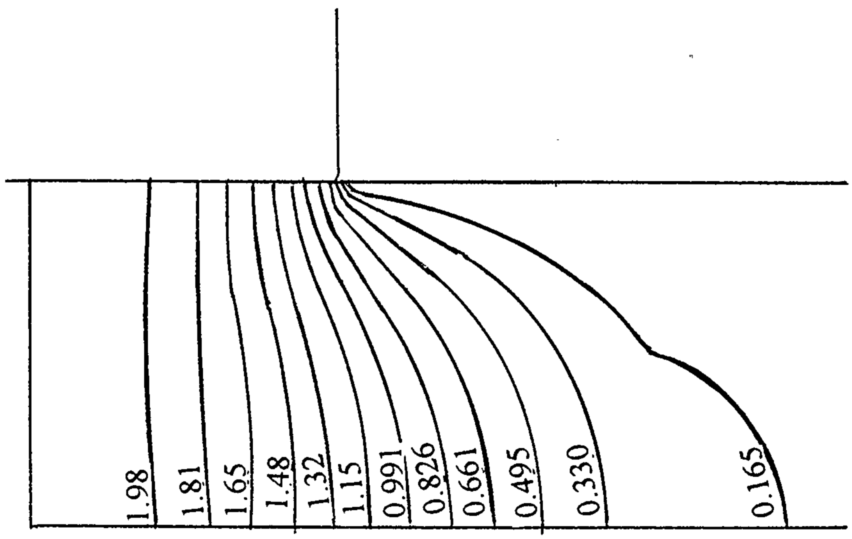

Figure B-7
h=2.25mm
r/h=0.89
x 100 MPa
Model G - Pore Pressures @ t = 500s

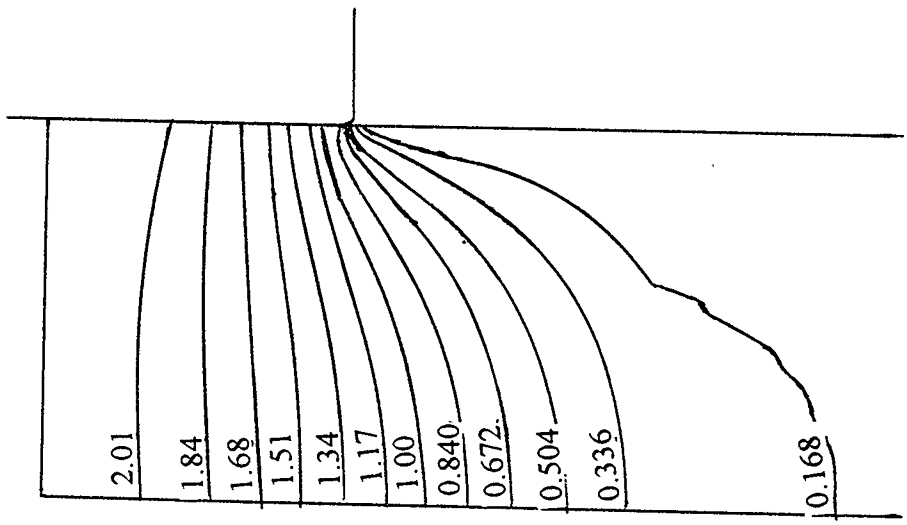

Figure B-8
h=2.50mm
r/h=0.80
x 100 MPa
Model H - Pore Pressures @ t = 500s

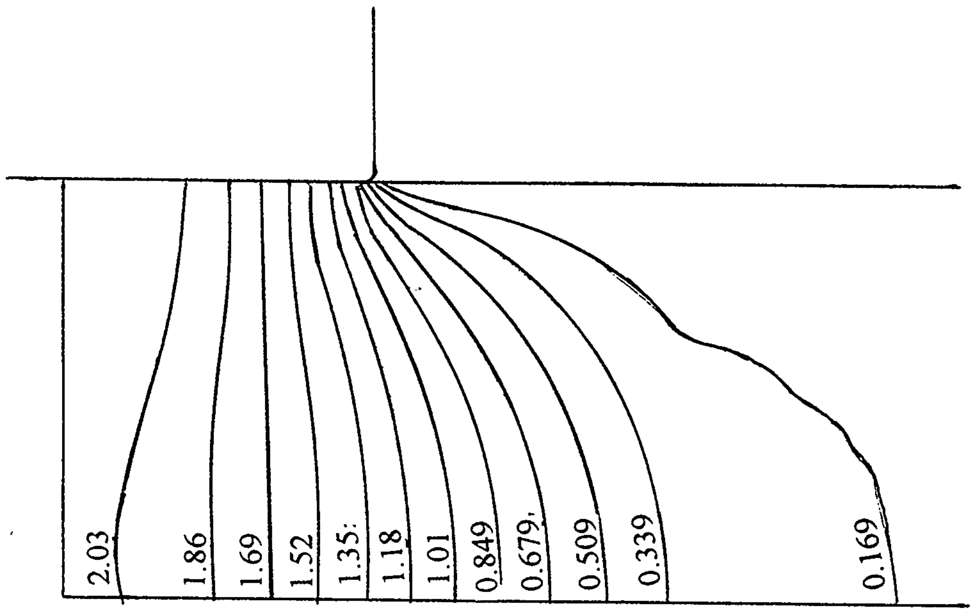

Figure B-9
h=2.75mm
r/h=0.73
x 100 MPa
Model I - Pore Pressures @ t = 500s

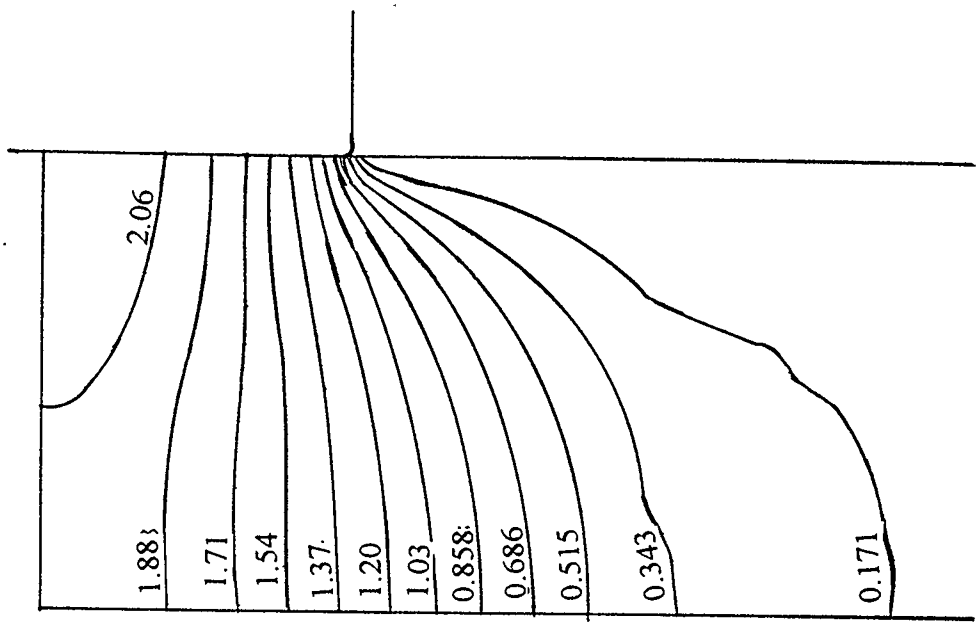

Figure B-10
h=3.00mm
r/h=0.67
x 100 MPa
Model J - Pore Pressures @ t = 500s

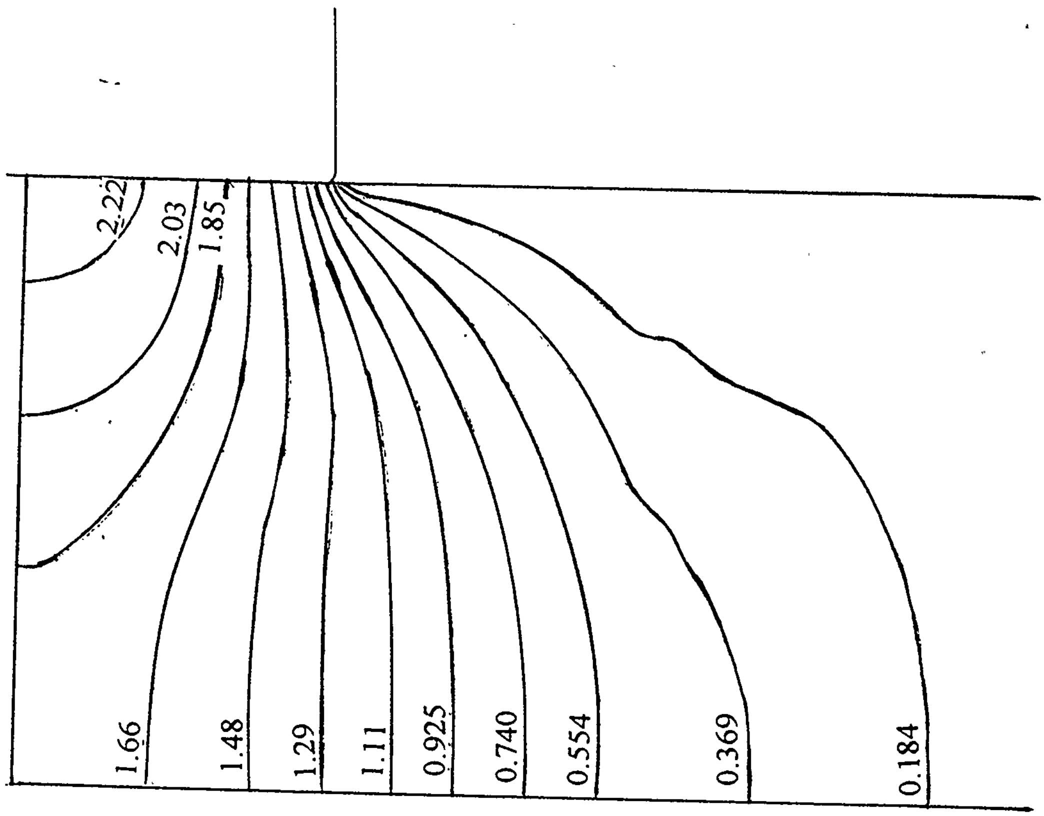

Figure B-11
h=4.00mm
r/h=0.50
x 100 MPa
Model K - Pore Pressures @ t = 500s

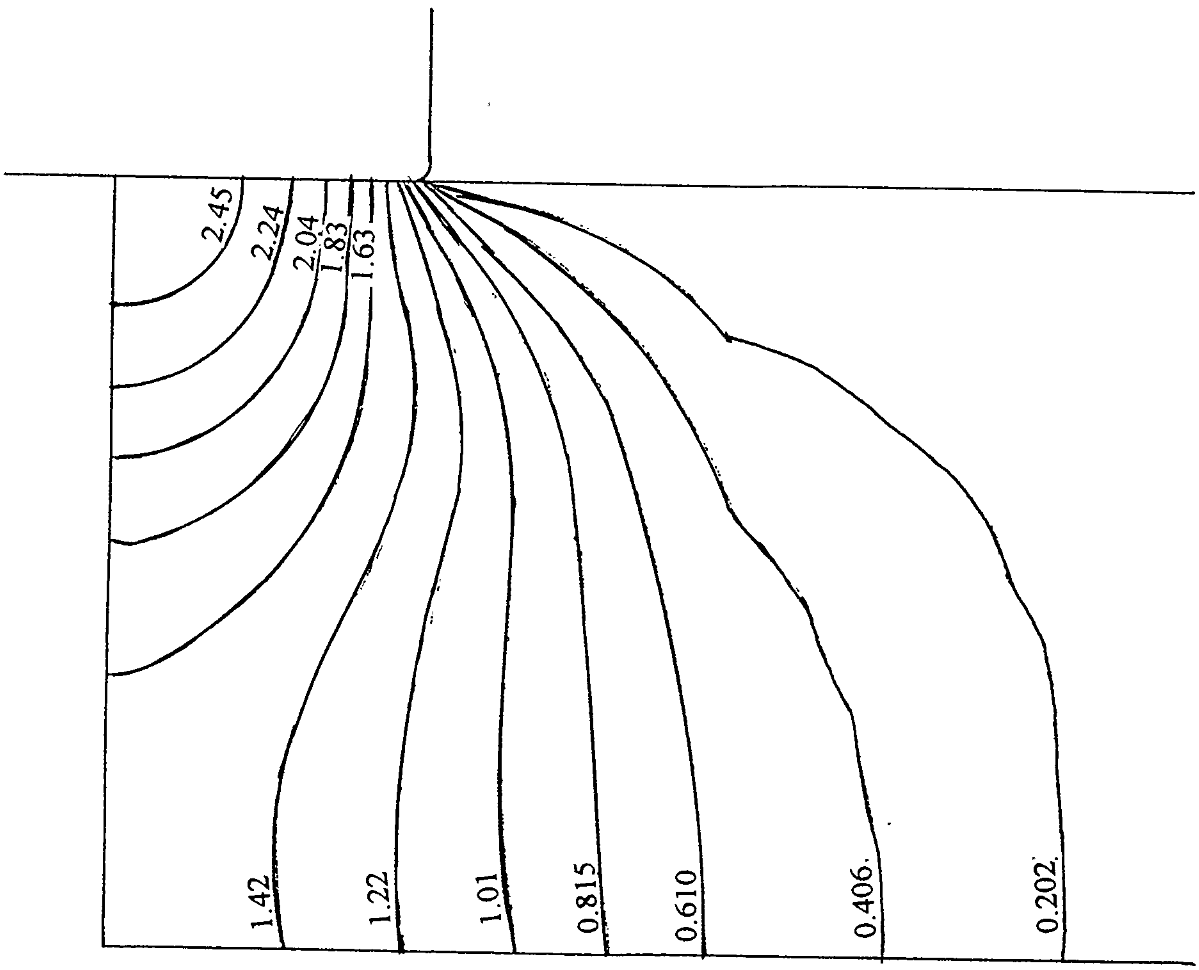

Figure B-12
h=5.00mm
r/h=0.40
x 100 MPa
Model L - Pore Pressures @ t = 500s

C.0 Appendix C

Results recorded at t=20s. Figures C-1 to C-12 show only the location near the indentor edge, since the pore pressures change is negligible beyond this point.

Table C-1 Model A - Material Parameters @ t = 20s

Model A	r=	2.00	mm	r/h=	2.67	
	h=	0.75	mm	t=	20	sec
	R=	20.00	mm			

Note: '-' implies compressive; Stresses & Pore Pressures are measured in MPa

Node	Vertical Stress	Horizontal Stress	Shear Stress	Max Principal Stress	Min Principal Stress	Pore Pressure
1	-1.1449E-02	1.7467E-03	8.8982E-07	-2.2838E-02	-3.7101E-03	1.0490E-01
2	-1.6251E-02	5.9197E-03	1.2733E-07	-2.3591E-02	-2.7928E-03	1.0380E-01
3	-2.7458E-02	1.3483E-02	1.6353E-07	-2.4680E-02	-1.4400E-03	9.9468E-02
4	-1.2419E-02	1.8952E-03	1.6362E-02	-2.3780E-02	-3.3102E-03	9.1833E-02
5	-1.7124E-02	6.1808E-03	1.2749E-02	-2.4221E-02	-2.7678E-03	9.0771E-02
6	-2.6355E-02	1.2267E-02	9.6416E-04	-2.4722E-02	-2.2671E-03	8.7119E-02
7	-1.9822E-03	-2.4943E-03	3.0408E-02	-1.7632E-02	1.5534E-03	3.9015E-02
8	-2.7984E-03	-5.0840E-03	2.5441E-02	-1.7823E-02	8.0043E-04	3.8488E-02
9	1.5417E-02	-2.5333E-02	2.3191E-02	-2.2889E-02	1.0734E-03	2.2638E-02
10	6.8883E-03	-4.4256E-03	1.6846E-02	-5.7411E-03	2.8554E-03	1.2791E-02
11	8.8906E-03	-1.0122E-02	1.2429E-02	-5.4047E-03	1.7679E-03	1.2480E-02
12	2.1300E-03	-1.2348E-02	-5.2787E-04	-3.2335E-03	8.8337E-04	2.0662E-03
Node	**Vertical Strain**	**Horizontal Strain**	**Shear Strain**	**Max Principal Strain**	**Min Principal Strain**	**Void Ratio**
1	-2.5762E-02	7.2034E-03	4.4461E-06	-4.6256E-02	1.5322E-03	3.944
2	-3.9024E-02	1.6364E-02	6.3621E-07	-4.8522E-02	3.4376E-03	3.969
3	-6.8422E-02	3.3860E-02	8.1711E-07	-5.1820E-02	6.2402E-03	3.996
4	-2.7867E-02	7.8930E-03	8.1754E-02	-4.8372E-02	2.7673E-03	3.938
5	-4.0982E-02	1.7240E-02	6.3700E-02	-4.9815E-02	3.7811E-03	3.964
6	-6.5499E-02	3.0991E-02	4.8175E-03	-5.1470E-02	4.6269E-03	3.993
7	-4.2155E-03	-5.4949E-03	1.5190E-01	-5.1093E-02	-1.0515E-02	3.985
8	-6.1494E-03	-1.1859E-02	1.2710E-01	-3.8007E-02	8.5204E-03	3.983
9	3.8581E-02	-6.3216E-02	1.1590E-01	-4.8893E-02	1.0972E-02	3.995
10	1.5675E-02	-9.6826E-03	8.7658E-02	-1.3264E-02	8.2123E-03	4.031
11	2.1595E-02	-2.5903E-02	6.2102E-02	-1.2242E-02	5.6772E-03	4.012
12	7.4699E-03	-2.8701E-02	-2.6375E-03	-7.4143E-03	2.8707E-03	3.957

Table C-2 Model B - Material Parameters @ t = 20s

Model B	r=	2.00	mm	r/h=	2.00	
	h=	1.00	mm	t=	20	sec
	R=	20.00	mm			

Note: '-' implies compressive; Stresses & Pore Pressures are measured in MPa

Node	Vertical Stress	Horizontal Stress	Shear Stress	Max Principal Stress	Min Principal Stress	Pore Pressure
1	-1.2017E-02	3.8575E-03	-2.6921E-07	-2.2381E-02	-2.6144E-03	8.1607E-02
2	-1.9857E-02	9.3181E-03	8.6549E-07	-2.3744E-02	-9.1088E-04	7.8633E-02
3	-2.7904E-02	1.3917E-02	2.5158E-07	-2.4622E-02	2.6527E-04	7.4618E-02
4	-1.3619E-02	4.5512E-03	1.2187E-02	-2.3374E-02	-2.0275E-03	7.2752E-02
5	-2.0816E-02	9.8163E-03	6.9059E-03	-2.4278E-02	-1.1506E-03	7.0302E-02
6	-2.5770E-02	1.1966E-02	3.1114E-04	-2.4601E-02	-1.2726E-03	6.7798E-02
7	-3.6304E-03	-2.0531E-03	2.3431E-02	-1.7290E-02	1.9212E-03	3.5019E-02
8	-6.1378E-03	-3.8257E-03	1.9414E-02	-1.8707E-02	1.1402E-03	3.4082E-02
9	1.2719E-02	-2.4536E-02	2.5047E-02	-2.6788E-02	1.9473E-03	2.0469E-02
10	5.7677E-03	-6.5928E-03	1.5672E-02	-7.8578E-03	3.0709E-03	1.4332E-02
11	8.1334E-03	-1.2734E-02	9.2815E-03	-7.0927E-03	1.5617E-03	1.3371E-02
12	1.7730E-03	-8.4185E-03	-7.3166E-04	-3.6617E-03	1.0449E-03	1.7373E-03

Node	Vertical Strain	Horizontal Strain	Shear Strain	Max Principal Strain	Min Principal Strain	Void Ratio
1	-2.8486E-02	1.1173E-02	-1.3451E-06	-4.6058E-02	3.3239E-03	3.969
2	-4.9173E-02	2.3715E-02	4.3245E-06	-5.0193E-02	6.8503E-03	3.991
3	-6.9687E-02	3.4793E-02	1.2570E-06	-5.2913E-02	9.2624E-03	3.999
4	-3.2211E-02	1.3183E-02	6.0893E-02	-4.8371E-02	4.9572E-03	3.964
5	-5.1445E-02	2.5083E-02	3.4506E-02	-5.1161E-02	6.6182E-03	3.989
6	-6.4197E-02	3.0078E-02	1.5546E-03	-5.2062E-02	6.2172E-03	3.996
7	-8.5015E-03	-4.5608E-03	1.1710E-01	-3.7434E-02	1.0730E-02	3.989
8	-1.4753E-02	-8.9769E-03	9.7003E-02	-4.0452E-02	9.1310E-03	3.988
9	3.2536E-02	-6.0540E-02	1.2510E-01	-5.7668E-02	1.4121E-02	3.980
10	1.3753E-02	-1.7127E-02	7.8305E-02	-1.7952E-02	9.3512E-03	4.013
11	2.0245E-02	-3.1889E-02	4.6376E-02	-1.5985E-02	5.6358E-03	4.002
12	4.7432E-03	-2.0718E-02	-3.6558E-03	-8.5726E-03	3.1859E-03	3.994

Table C-3 Model C - Material Parameters @ t = 20s

Model C r= 2.00 mm r/h= 1.60

h= 1.25 mm t= 20 sec

R= 20.00 mm

Note: '-' implies compressive; Stresses & Pore Pressures are measured in MPa

Node	Vertical Stress	Horizontal Stress	Shear Stress	Max Principal Stress	Min Principal Stress	Pore Pressure
1	-1.3160E-02	5.3300E-03	-3.7633E-07	-2.2130E-02	-1.4600E-03	6.8201E-02
2	-2.2387E-02	1.1033E-02	7.4858E-07	-2.3884E-02	7.5732E-04	6.3852E-02
3	-2.7315E-02	1.3658E-02	1.8542E-07	-2.4414E-02	1.5663E-03	6.0716E-02
4	-1.4826E-02	6.2639E-03	9.6682E-03	-2.2867E-02	-6.7829E-04	6.0983E-02
5	-2.3032E-02	1.1405E-02	3.5468E-03	-2.4380E-02	2.0983E-03	5.7951E-02
6	-2.4739E-02	1.1417E-02	-2.4384E-05	-2.4599E-02	-5.7993E-04	5.7132E-02
7	-5.0056E-03	-1.2650E-03	1.9036E-02	-1.6765E-02	2.3193E-03	3.1872E-02
8	-8.9662E-03	-2.0047E-03	1.6852E-02	-1.9647E-02	1.7191E-03	3.0833E-02
9	9.1945E-03	-2.7341E-02	2.8702E-02	-3.0609E-02	2.8335E-03	1.9551E-02
10	3.9968E-03	-6.7974E-03	1.4261E-02	-9.1070E-03	3.2318E-03	1.5308E-02
11	6.3819E-03	-1.2564E-02	8.0449E-03	-8.2733E-03	1.6345E-03	1.3532E-02
12	1.4492E-03	-5.3609E-03	-7.0566E-04	-3.8430E-03	1.2659E-03	1.4290E-03
Node	**Vertical Strain**	**Horizontal Strain**	**Shear Strain**	**Max Principal Strain**	**Min Principal Strain**	**Void Ratio**
1	-3.1986E-02	1.4208E-02	-1.8804E-06	-4.6346E-02	5.2944E-03	3.982
2	-5.5814E-02	2.7677E-02	3.7404E-06	-5.1684E-02	9.8769E-03	3.998
3	-6.8240E-02	3.4121E-02	9.2647E-07	-5.3397E-02	1.1510E-02	4.000
4	-3.5993E-02	1.6695E-02	4.8308E-02	-4.8226E-02	7.2073E-03	3.979
5	-5.7364E-02	2.8669E-02	1.7722E-02	-5.2454E-02	9.1086E-03	3.996
6	-6.1646E-02	2.8681E-02	-1.2184E-02	-5.2658E-02	7.3490E-03	3.997
7	-1.2130E-02	-2.7845E-03	9.5114E-02	-3.6696E-02	1.0981E-02	3.992
8	-2.2004E-02	-4.6123E-03	8.4203E-02	-4.3055E-02	1.0324E-02	3.992
9	2.6375E-02	-6.4903E-02	1.4340E-01	-6.6232E-02	1.7316E-02	3.929
10	9.7502E-03	-1.7217E-02	7.1255E-02	-2.0835E-02	9.9906E-03	4.005
11	1.5938E-02	-3.1394E-02	4.0197E-02	-1.8787E-02	5.9657E-03	4.000
12	2.6460E-03	-1.4367E-02	-3.5259E-03	-9.2166E-03	3.5470E-03	4.020

Table C-4 Model D - Material Parameters @ t = 20s

Model D r= 2.00 mm r/h= 1.33

h= 1.50 mm t= 20 sec

R= 20.00 mm

Note: '-' implies compressive; Stresses & Pore Pressures are measured in MPa

Node	Vertical Stress	Horizontal Stress	Shear Stress	Max Principal Stress	Min Principal Stress	Pore Pressure
1	-1.4688E-02	6.5969E-03	-5.2647E-07	-2.2000E-02	-2.5061E-04	5.9289E-02
2	-2.3848E-02	1.1892E-02	3.4753E-08	-2.3968E-02	2.1102E-03	5.4329E-02
3	-2.5983E-02	1.2995E-02	9.8047E-08	-2.4117E-02	2.4131E-03	5.2285E-02
4	-1.5867E-02	7.3099E-03	8.0421E-03	-2.2283E-02	5.7226E-04	5.2852E-02
5	-2.4327E-02	1.2194E-02	1.6719E-03	-2.4617E-02	1.4312E-03	5.0047E-02
6	-2.3576E-02	1.0902E-02	-2.0127E-04	-2.4767E-02	-1.4671E-04	5.0894E-02
7	-6.1045E-03	-5.5179E-04	1.6053E-02	-1.6177E-02	2.6709E-03	2.9378E-02
8	-1.1190E-02	-3.7707E-04	1.5708E-02	-2.0566E-02	2.3721E-03	2.8503E-02
9	5.6652E-03	-3.1598E-02	3.2993E-02	-3.4331E-02	3.6749E-03	1.9352E-02
10	2.2547E-03	-6.2191E-03	1.2985E-02	-9.8015E-03	3.3358E-03	1.5889E-02
11	4.5344E-03	-1.1683E-02	7.8914E-03	-9.2422E-03	1.8199E-03	1.3410E-02
12	1.2105E-03	-3.1552E-03	-6.1609E-04	-3.9666E-03	1.5128E-03	1.1988E-03

Node	Vertical Strain	Horizontal Strain	Shear Strain	Max Principal Strain	Min Principal Strain	Void Ratio
1	-3.6160E-02	1.7014E-02	-2.6306E-06	-4.6930E-02	7.4058E-03	3.9890
2	-5.9555E-02	2.9732E-02	-1.7365E-07	-5.2830E-02	1.2321E-02	4.0000
3	-6.4914E-02	3.2462E-02	4.8990E-07	-5.3365E-02	1.2915E-02	4.0000
4	-3.9047E-02	1.8855E-02	4.0183E-02	-4.7885E-02	9.2139E-03	3.9880
5	-6.0712E-02	3.0528E-02	8.3536E-03	-5.3821E-02	1.1256E-02	3.9990
6	-5.8738E-02	2.7397E-02	-1.0057E-03	-5.3383E-02	8.1264E-03	3.9970
7	-1.5020E-02	-1.1481E-03	8.0213E-02	-3.5877E-02	1.1209E-02	3.9950
8	-2.7670E-02	-6.5532E-04	7.8485E-02	-4.5587E-02	1.1720E-02	3.9940
9	2.0857E-02	-7.2237E-02	1.6490E-01	-7.4511E-02	2.0437E-02	3.8660
10	5.5663E-03	-1.5603E-02	6.4880E-02	-2.2542E-02	1.0279E-02	4.0010
11	1.1314E-02	-2.9202E-02	3.9430E-02	-2.1172E-02	6.4649E-03	4.0000
12	1.1900E-03	-9.7169E-03	-3.0783E-03	-9.7140E-03	3.9751E-03	4.0370

Table C-5 Model E - Material Parameters @ t = 20s

Model E	r=	2.00	mm	r/h=	1.14	
	h=	1.75	mm	t=	20	sec
	R=	20.00	mm			

Note: '-' implies compressive; Stresses & Pore Pressures are measured in MPa

Node	Vertical Stress	Horizontal Stress	Shear Stress	Max Principal Stress	Min Principal Stress	Pore Pressure
1	-1.6301E-02	7.7179E-03	-8.3350E-07	-2.1895E-02	9.6622E-04	5.2691E-02
2	-2.4481E-02	1.2244E-02	-7.5529E-07	-2.4028E-02	3.1349E-03	4.7910E-02
3	-2.4310E-02	1.2154E-02	4.5944E-08	-2.3824E-02	2.8722E-03	4.7001E-02
4	-1.6723E-02	7.9325E-03	6.9681E-03	-2.1675E-02	1.6687E-03	4.6805E-02
5	-2.5101E-02	1.2684E-02	7.2814E-04	-2.4973E-02	2.4010E-03	4.4801E-02
6	-2.2411E-02	1.0447E-02	-2.9628E-04	-2.5070E-02	6.6586E-05	4.7192E-02
7	-7.0071E-03	4.3006E-05	1.3919E-02	-1.5605E-02	2.9570E-03	2.7360E-02
8	-1.2922E-02	9.7888E-03	1.5241E-02	-2.1439E-02	3.0290E-03	2.6842E-02
9	2.4061E-03	-3.6336E-02	3.7466E-02	-3.7916E-02	4.4305E-03	1.9590E-02
10	6.9436E-04	5.3979E-03	1.1893E-02	-1.0164E-02	3.3744E-03	1.6189E-02
11	2.8285E-03	-1.0672E-02	8.2660E-03	-1.0132E-02	2.0617E-03	1.3244E-02
12	1.0526E-03	-1.5750E-03	-5.1748E-04	-4.1185E-03	1.7793E-03	1.0458E-03
Node	**Vertical Strain**	**Horizontal Strain**	**Shear Strain**	**Max Principal Strain**	**Min Principal Strain**	**Void Ratio**
1	-4.0416E-02	1.9590E-02	-4.1647E-06	-4.7575E-02	9.5398E-03	3.994
2	-6.1164E-02	3.0586E-02	-3.7739E-06	-5.3691E-02	1.4171E-02	4.000
3	-6.0732E-02	3.0365E-02	2.2956E-07	-5.3067E-02	1.3630E-02	4.000
4	-4.1455E-02	2.0142E-02	3.4816E-02	-4.7411E-02	1.0908E-02	3.994
5	-6.2683E-02	3.1715E-02	3.6382E-03	-5.5273E-02	1.3115E-02	3.999
6	-5.5820E-02	2.6268E-02	-1.4804E-02	-5.4204E-02	8.5946E-03	3.997
7	-1.7372E-02	2.4132E-04	6.9548E-02	-3.5044E-02	1.1329E-02	3.997
8	-3.2068E-02	2.6607E-03	7.6155E-02	-4.7969E-02	1.3159E-02	3.996
9	1.6129E-02	-8.0661E-02	1.8720E-01	-8.2413E-02	2.3380E-02	3.803
10	1.7266E-03	-1.3494E-02	5.9424E-02	-2.3520E-02	1.0302E-02	4.000
11	7.0436E-03	-2.6686E-02	4.1302E-02	-2.3383E-02	7.0793E-03	4.000
12	2.2458E-04	-6.3399E-03	-2.5856E-03	-1.0238E-02	4.4969E-03	4.049

Table C-6 Model F - Material Parameters @ t = 20s

Model F r= 2.00 mm r/h= 1.00

h= 2.00 mm t= 20 sec

R= 20.00 mm

Note: '-' implies compressive; Stresses & Pore Pressures are measured in MPa

Node	Vertical Stress	Horizontal Stress	Shear Stress	Max Principal Stress	Min Principal Stress	Pore Pressure
1	-1.7778E-02	8.6596E-03	-1.2088E-06	-2.1759E-02	2.1278E-03	4.7437E-02
2	-2.4622E-02	1.2322E-02	-1.1236E-06	-2.4117E-02	3.8861E-03	4.3493E-02
3	-2.2583E-02	1.1287E-02	2.4274E-08	-2.3591E-02	3.0441E-03	4.3787E-02
4	-1.7406E-02	8.3028E-03	6.2515E-03	-2.1082E-02	2.6104E-03	4.2067E-02
5	-2.5595E-02	1.3050E-02	3.6426E-04	-2.5415E-02	3.2044E-03	4.1224E-02
6	-2.1304E-02	1.0039E-02	3.4904E-04	-2.5457E-02	9.9069E-05	4.5057E-02
7	-7.7751E-03	5.4929E-04	1.2331E-02	-1.5088E-02	3.1880E-03	2.5682E-02
8	-1.4280E-02	2.0903E-02	1.5136E-02	-2.2253E-02	3.6613E-03	2.5652E-02
9	-6.1119E-04	-4.1250E-02	4.2015E-03	-4.1346E-02	5.0835E-03	2.0115E-02
10	-6.7463E-04	-4.5429E-03	1.0970E-02	-1.0335E-02	3.3661E-03	1.6289E-02
11	1.3159E-03	-9.6935E-03	8.8899E-03	-1.0998E-02	2.3493E-03	1.3141E-02
12	9.6122E-04	-4.4382E-04	-4.2557E-04	-4.3240E-03	2.0635E-03	9.5744E-04
Node	**Vertical Strain**	**Horizontal Strain**	**Shear Strain**	**Max Principal Strain**	**Min Principal Strain**	**Void Ratio**
1	-4.4250E-02	2.1798E-02	-6.0398E-06	-4.8113E-02	1.1564E-02	3.997
2	-6.1520E-03	3.0775E-02	-5.6139E-06	-5.4416E-02	1.5543E-02	4.000
3	-5.6417E-02	2.8202E-02	1.2129E-07	-5.2689E-02	1.3853E-02	4.000
4	-4.3318E-02	2.0911E-02	3.1236E-02	-4.6873E-02	1.2318E-02	3.997
5	-6.3933E-02	3.2612E-02	1.8200E-03	-5.6769E-02	1.4730E-02	4.000
6	-5.3047E-02	2.5256E-02	-1.7440E-03	-5.5056E-02	8.7893E-03	3.996
7	-1.9351E-02	1.4455E-03	6.1613E-02	-3.4277E-02	1.1381E-02	3.999
8	-3.5514E-02	5.3848E-03	7.5626E-02	-5.0172E-02	1.4570E-02	3.997
9	1.1989E-02	-8.9593E-02	2.0990E-01	-8.9900E-02	2.6094E-02	3.741
10	-1.6785E-03	-1.1343E-02	5.4812E-02	-2.4066E-02	1.0165E-02	4.000
11	3.2609E-03	-2.4244E-02	4.6098E-02	-2.5533E-02	7.8132E-03	4.001
12	-3.7869E-04	-3.8889E-03	-2.1264E-03	-1.0841E-02	5.1163E-03	4.056

Model G r= 2.00 mm r/h= 0.89

h= 2.25 mm t= 20 sec

R= 20.00 mm

Note: '-' implies compressive; Stresses & Pore Pressures are measured in MPa

Node	Vertical Stress	Horizontal Stress	Shear Stress	Max Principal Stress	Min Principal Stress	Pore Pressure
1	-1.9002E-02	9.3997E-03	-1.5632E-06	-2.1572E-02	3.1874E-03	4.3064E-02
2	-2.4542E-02	1.2284E-02	-1.1519E-06	-2.4265E-02	4.4376E-03	4.0429E-02
3	-2.0960E-02	1.0472E-02	1.3199E-06	-2.3428E-02	3.0163E-03	4.1673E-02
4	-1.7929E-02	8.5236E-03	5.7665E-03	-2.0524E-02	3.4148E-03	3.8213E-02
5	-2.5951E-02	1.3354E-02	3.5576E-04	-2.5909E-02	3.8782E-03	3.8738E-02
6	-2.0286E-02	9.6664E-03	-3.8046E-04	-2.5884E-02	-1.4763E-05	4.3949E-02
7	-8.4443E-03	9.9723E-04	1.1115E-02	-1.4641E-02	3.3827E-03	2.4249E-02
8	-1.5358E-02	2.9933E-03	1.5236E-02	-2.3004E-02	4.2588E-03	2.4790E-02
9	-3.4196E-03	-4.6200E-02	4.6594E-02	-4.4621E-02	5.6341E-03	2.0845E-02
10	-1.8726E-03	-3.7288E-03	1.0191E-02	-1.0403E-02	3.3366E-03	1.6245E-02
11	-8.5147E-06	-8.7907E-03	9.6282E-03	-1.1857E-02	2.6791E-03	1.3114E-02
12	9.2300E-04	3.6184E-04	-3.4393E-04	-4.5685E-03	2.3570E-03	9.2108E-04

Node	Vertical Strain	Horizontal Strain	Shear Strain	Max Principal Strain	Min Principal Strain	Void Ratio
1	-4.7399E-02	2.3555E-02	-7.8108E-06	-4.8468E-02	1.3388E-02	3.999
2	-6.1322E-02	3.0680E-02	-5.7557E-06	-5.5127E-02	1.6580E+02	4.000
3	-5.2358E-02	2.6167E-02	6.5951E-06	-5.2320E-02	1.3745E-02	4.000
4	-4.4713E-02	2.1373E-02	2.8813E-02	-4.6312E-02	1.3494E-02	3.998
5	-6.4835E-02	3.3359E-02	1.7776E-03	-5.8272E-02	1.6145E-02	4.000
6	-5.0495E-02	2.4334E-02	-1.9010E-03	-5.5883E-02	8.7457E-03	3.996
7	-2.1060E-02	2.5277E-03	5.5535E-02	-3.3616E-02	1.1412E-02	3.999
8	-3.8245E-02	7.6007E-03	7.6130E-02	-5.2190E-02	1.5921E-02	3.998
9	8.3044E-03	-9.8574E-02	2.3280E-01	-9.6978E-02	2.8573E-02	3.682
10	-4.6715E-03	-9.3088E-03	5.0918E-02	-2.4368E-02	9.9565E-03	4.000
11	-5.0167E-05	-2.1991E-02	4.8108E-02	-2.7654E-02	8.6604E-03	4.001
12	-7.1449E-04	-2.1164E-03	-1.7185E-03	-1.1496E-02	5.8060E-03	4.061

Table C-7 Model G - Material Parameters @ t = 20s

Table C-8 Model H - Material Parameters @ t = 20s

Model H r= 2.00 mm r/h= 0.80
h= 2.50 mm t= 20 sec
R= 20.00 mm

Note: '-' implies compressive; Stresses & Pore Pressures are measured in MPa

Node	Vertical Stress	Horizontal Stress	Shear Stress	Max Principal Stress	Min Principal Stress	Pore Pressure
1	-1.9938E-02	9.9436E-03	-1.8485E-03	-2.1337E-02	4.1230E-03	3.9337E-02
2	-2.4417E-02	1.2226E-02	-9.2461E-07	-2.4482E-02	4.8546E-03	3.8308E-02
3	-1.9499E-02	9.7372E-03	4.0974E-06	-2.3244E-02	2.7470E-03	4.0557E-02
4	-1.8307E-02	8.6528E-03	5.4289E-03	-2.0012E-02	4.1020E-03	3.4996E-02
5	-2.6254E-02	1.3625E-02	5.6157E-04	-2.6431E-02	4.4561E-03	3.6993E-02
6	-1.9363E-02	9.3237E-03	-4.0196E-04	-2.6315E-02	-2.5274E-04	4.3553E-02
7	-9.0331E-03	1.4046E-03	1.0162E-02	-1.4266E-02	3.5582E-03	2.2995E-02
8	-3.5546E-03	-5.3128E-03	1.0298E-02	-2.3692E-02	4.8197E-03	2.4164E-02
9	-6.0379E-03	-5.1086E-02	5.1160E-02	-4.7745E-02	6.0897E-03	2.1712E-02
10	-2.9219E-03	-2.9789E-03	9.5322E-03	-1.0419E-02	3.3073E-03	1.6100E-02
11	-1.1653E-03	-7.9742E-03	1.0412E-02	-1.2701E-02	3.0414E-03	1.3165E-02
12	9.2043E-04	9.3002E-04	-2.7254E-04	-4.8092E-03	2.6469E-03	9.1964E-04
Node	**Vertical Strain**	**Horizontal Strain**	**Shear Strain**	**Max Principal Strain**	**Min Principal Strain**	**Void Ratio**
1	-4.9792E-02	2.4860E-02	-9.2361E-06	-4.8632E-02	1.4973E-02	4.000
2	-6.1013E-02	3.0531E-02	-4.6199E-06	-5.5891E-02	1.7402E-02	4.000
3	-4.8705E-02	2.4335E-02	2.0473E-05	-5.1964E-02	1.3406E-02	4.000
4	-4.5707E-02	2.1647E-02	2.7126E-02	-4.5760E-02	1.4485E-02	3.999
5	-6.5605E-02	3.4024E-02	2.8059E-03	-6.4308E-02	2.1949E-02	4.000
6	-4.8182E-02	2.3487E-02	-2.0084E-03	-5.6590E-02	8.4825E-03	3.996
7	-2.2553E-02	3.5238E-03	5.0774E-02	-3.3075E-02	1.1455E-02	4.000
8	-4.0443E-02	9.3885E-03	7.7262E-02	-5.4031E-02	1.7200E-02	3.998
9	4.9887E-03	-1.0760E-01	2.5560E-01	-1.0367E-01	3.0831E-02	3.626
10	-7.2969E-03	-7.4394E-03	4.7628E-02	-2.4546E-02	9.7452E-03	4.000
11	-2.9441E-03	-1.9955E-02	5.2022E-02	-2.9733E-02	9.5951E-03	4.001
12	-8.6554E-04	-8.4158E-04	-1.3618E-03	-1.2110E-02	6.5166E-03	4.064

Table C-9 Model I - Material Parameters @ t = 20s

Model I

r=	2.00	mm	r/h=	0.73		
h=	2.75	mm	t=	20	sec	
R=	20.00	mm				

Note: '-' implies compressive; Stresses & Pore Pressures are measured in MPa

Node	Vertical Stress	Horizontal Stress	Shear Stress	Max Principal Stress	Min Principal Stress	Pore Pressure
1	-2.0597E-02	1.0313E-02	-2.0454E-06	-2.0986E-02	4.8910E-03	3.6118E-02
2	-2.4345E-02	1.2196E-02	-5.1267E-07	-2.4792E-02	5.1991E-03	3.6854E-02
3	-1.8208E-02	9.0895E-03	6.3970E-06	-2.3377E-02	2.6489E-03	4.0079E-02
4	-1.8557E-02	8.7212E-03	5.1817E-03	-1.9476E-02	4.6570E-03	3.2258E-02
5	-2.6555E-02	1.3880E-02	8.9646E-04	-2.6964E-02	4.9558E-03	3.5762E-02
6	-1.8532E-02	9.0077E-03	-4.1986E-04	-2.6887E-02	-5.0492E-04	4.3667E-02
7	-9.5506E-03	1.7801E-03	9.4010E-03	-1.3924E-02	3.7159E-03	2.1877E-02
8	-1.6937E-02	4.3034E-03	1.5770E-02	-2.4306E-02	5.3372E-03	2.3710E-02
9	-8.4621E-03	-5.5835E-02	5.5606E-02	-5.0778E-02	6.4311E-03	2.2625E-02
10	-3.8426E-03	-2.2958E-03	8.9752E-03	-1.0396E-02	3.2893E-03	1.5884E-02
11	-2.1791E-03	-7.2421E-03	1.1202E-02	-1.3555E-02	3.4506E-03	1.3285E-02
12	9.3198E-04	1.3155E-03	-2.0869E-04	-5.2538E-03	2.9836E-03	9.3218E-04

Node	Vertical Strain	Horizontal Strain	Shear Strain	Max Principal Strain	Min Principal Strain	Void Ratio
1	-5.1467E-02	2.5755E-02	-1.0220E-05	-4.8430E-02	1.6219E-02	4.000
2	-6.0837E-02	3.0452E-02	-2.5616E-04	-5.6799E-02	1.8127E-02	4.000
3	-4.5480E-02	2.2719E-02	3.1963E-05	-5.1949E-02	1.3071E-02	4.000
4	-4.6355E-02	2.1793E-02	2.5891E-02	-4.5053E-02	1.5241E-02	4.000
5	-6.6371E-02	3.4648E-02	4.4792E-03	-6.1224E-02	1.8523E-02	4.001
6	-4.6096E-02	2.2705E-02	-2.0979E-03	-5.7665E-02	8.2459E-03	3.996
7	-2.3857E-02	4.4501E-03	4.6973E-02	-3.2564E-02	1.1504E-02	4.000
8	-4.2244E-02	1.0821E-02	7.8794E-02	-5.5673E-02	1.8383E-02	3.999
9	2.0151E-03	-1.1630E-01	2.7780E-01	-1.1011E-01	3.2808E-02	3.574
10	-9.6010E-03	-5.7366E-03	4.4845E-02	-2.4626E-02	9.5642E-03	4.000
11	-5.4840E-03	-1.8133E-02	5.5973E-02	-3.1832E-02	1.0652E-02	4.001
12	-9.0584E-04	5.2386E-05	1.0427E-03	-1.3161E-02	7.4180E-03	4.066

Table C-10 Model J - Material Parameters @ t = 20s

Model J

r=	2.00	mm	r/h=	0.67		
h=	3.00	mm	t=	20	sec	
R=	20.00	mm				

Note: '-' implies compressive; Stresses & Pore Pressures are measured in MPa

Node	Vertical Stress	Horizontal Stress	Shear Stress	Max Principal Stress	Min Principal Stress	Pore Pressure
1	-2.1008E-02	1.0537E-02	-2.1492E-06	-2.0568E-02	5.5178E-03	3.3310E-02
2	-2.4371E-02	1.2218E-02	3.3494E-08	-2.5183E-02	5.5076E-03	3.5872E-02
3	-1.7082E-02	8.5245E-03	8.3166E-06	-2.3544E-02	2.4277E-03	4.0063E-02
4	-1.8691E-02	8.7451E-03	4.9871E-03	-1.8953E-02	5.1140E-03	2.9894E-02
5	-2.6882E-02	1.4127E-02	1.3113E-03	-2.7509E-02	5.4514E-03	3.4893E-02
6	-1.7788E-02	8.7188E-03	-4.3697E-04	-2.7506E-02	-7.5250E-04	4.4154E-02
7	-1.0001E-02	2.1276E-03	8.7818E-03	-1.3626E-02	3.8669E-03	2.0865E-02
8	-1.7536E-02	4.7680E-03	1.6123E-02	-2.4881E-02	5.8239E-03	2.3382E-02
9	-1.0693E-02	-6.0423E-02	5.9866E-02	-5.3693E-02	6.7166E-03	2.3525E-02
10	-4.6515E-03	-1.6744E-03	8.5017E-03	-1.0363E-02	3.2919E-03	1.5619E-02
11	-3.0742E-03	-6.5856E-03	1.1977E-02	-1.4410E-02	3.8680E-03	1.3460E-02
12	9.4631E-04	1.5612E-03	-1.5039E-04	-5.8438E-03	3.2819E-03	9.4773E-04
Node	**Vertical Strain**	**Horizontal Strain**	**Shear Strain**	**Max Principal Strain**	**Min Principal Strain**	**Void Ratio**
1	-5.2506E-02	2.6300E-02	-1.0739E-05	-4.7982E-02	1.7188E-02	4.000
2	-6.0909E-02	3.0502E-02	1.6735E-07	-5.7857E-02	1.8817E-02	4.000
3	-4.2664E-02	2.1308E-02	4.1555E-05	-5.2148E-02	1.2736E-02	4.000
4	-4.6701E-02	2.1841E-02	2.4918E-02	-4.4291E-02	1.5836E-02	4.000
5	-6.7199E-02	3.5253E-02	6.5521E-03	-6.2688E-02	1.9583E-02	4.001
6	-4.4232E-02	2.1990E-02	-2.1834E-03	-5.8800E-02	8.0372E-03	3.996
7	-2.4989E-02	5.3124E-03	4.3879E-02	-3.2120E-02	1.1582E-02	4.000
8	-4.3754E-02	1.1968E-02	8.0561E-02	-5.7208E-02	1.9500E-02	3.999
9	-6.3344E-04	-1.2490E-01	2.9910E-01	-1.1629E-01	3.4620E-02	3.525
10	-1.1625E-02	-4.1870E-03	4.2479E-02	-2.4674E-02	9.4398E-03	4.000
11	-7.7308E-03	-1.6503E-02	5.9846E-02	-3.3924E-02	1.1740E-02	4.001
12	-8.8113E-04	6.5496E-04	-7.5141E-04	-1.4494E-02	8.3051E-03	4.066

Model K r= **2.00** mm r/h= **0.50**

h= **4.00** mm t= **20** sec

R= **20.00** mm

Note: '-' implies compressive; Stresses & Pore Pressures are measured in MPa

Node	Vertical Stress	Horizontal Stress	Shear Stress	Max Principal Stress	Min Principal Stress	Pore Pressure
1	-2.0929E-02	1.0485E-02	-1.7961E-06	-1.8661E-02	6.9461E-03	2.5044E-02
2	-2.5593E-02	1.2896E-02	2.8674E-06	-2.7241E-02	6.7428E-03	3.4586E-02
3	-1.3782E-02	6.8742E-03	1.3728E-05	-2.4713E-02	1.5492E-03	4.2774E-02
4	-1.8385E-02	8.5578E-03	4.3877E-03	-1.7075E-02	6.2224E-03	2.2957E-02
5	-2.8581E-02	1.5111E-02	3.3167E-03	-2.9663E-02	7.1548E-03	3.3416E-02
6	-1.5491E-02	7.7648E-03	-5.1618E-04	-3.0124E-02	-1.7533E-03	4.8413E-02
7	-1.1206E-02	3.2470E-03	7.1378E-03	-1.2749E-02	4.4122E-03	1.7555E-02
8	-1.9315E-02	5.8593E-03	1.7657E-02	-2.6750E-02	7.4866E-03	2.2789E-02
9	-1.8732E-02	-7.7024E-02	7.7107E-02	-6.4472E-02	7.4426E-03	2.7549E-02
10	-7.0053E-03	2.9622E-04	7.1709E-03	-1.0233E-02	3.4929E-03	1.4309E-02
11	-5.8304E-03	-4.5393E-03	1.4711E-02	-1.7448E-02	5.4578E-03	1.4469E-02
12	1.0948E-03	1.9802E-03	-4.4259E-06	-8.3718E-03	4.2563E-03	1.0974E-03
Node	**Vertical Strain**	**Horizontal Strain**	**Shear Strain**	**Max Principal Strain**	**Min Principal Strain**	**Void Ratio**
1	-5.2301E-02	2.6180E-02	-8.9743E-06	-4.4918E-02	1.9056E-02	4.000
2	-6.4010E-02	3.2146E-02	1.4327E-05	-6.3147E-02	2.1756E-02	4.001
3	-3.4420E-02	1.7186E-02	6.8791E-05	-5.4025E-02	1.1586E-02	4.000
4	-4.5933E-02	2.1377E-02	2.1924E-02	-4.1118E-02	1.7084E-02	4.000
5	-7.1490E-02	3.7665E-02	1.6572E-02	-6.8431E-02	2.3551E-02	4.002
6	-3.8463E-02	1.9636E-02	-2.5791E-03	-6.3660E-02	7.2179E-03	3.995
7	-2.7998E-02	8.1096E-03	3.5664E-02	-3.0797E-02	1.2076E-02	4.000
8	-4.8191E-02	1.4701E-02	8.8224E-02	-6.2260E-02	2.3273E-02	3.999
9	-1.0133E-02	-1.5580E-01	3.8530E-01	-2.0522E-02	1.4337E-01	3.357
10	-1.7506E-02	7.3569E-04	3.5830E-02	-2.4802E-02	9.4906E-03	4.000
11	-1.4694E-02	-1.1468E-02	7.3506E-02	-4.1373E-02	1.5851E-02	4.003
12	-3.8209E-04	1.8298E-03	-2.2114E-05	-2.0030E-02	1.1518E-02	4.063

Table C-11 Model K - Material Parameters @ t = 20s

Table C-12 Model L - Material Parameters @ t = 20s

Model L	r=	2.00	mm	r/h=	0.40	
	h=	5.00	mm	t=	20	sec
	R=	20.00	mm			

Note: '-' implies compressive; Stresses & Pore Pressures are measured in MPa

Node	Vertical Stress	Horizontal Stress	Shear Stress	Max Principal Stress	Min Principal Stress	Pore Pressure
1	-1.9180E-02	9.5864E-03	-1.0013E-06	-1.6745E-02	7.2445E-03	1.9462E-02
2	-2.8221E-02	1.4301E-02	4.4579E-06	-2.9676E-02	8.1996E-03	3.4111E-02
3	-1.2923E-02	6.4490E-03	1.7285E-05	-2.6487E-02	8.9165E-04	4.6339E-02
4	-1.7069E-02	7.9997E-03	3.7518E-03	-1.5452E-02	6.5321E-03	1.8179E-02
5	-3.0627E-02	1.5956E-02	5.5319E-03	-3.1665E-02	8.8196E-03	3.2399E-02
6	-1.5504E-02	7.9304E-03	-5.3237E-04	-3.3053E-02	-2.6384E-03	5.2916E-02
7	-1.1528E-02	3.9415E-03	6.0072E-03	-1.2072E-02	4.7698E-03	1.4826E-02
8	-2.0661E-02	6.3288E-03	1.8876E-02	-2.8138E-02	8.8262E-03	2.2306E-02
9	-2.0352E-02	-9.1247E-02	8.3290E-02	-7.4428E-02	7.8720E-03	3.0881E-02
10	-8.2721E-03	1.6526E-03	6.2119E-03	-1.0076E-02	3.7997E-03	1.2737E-02
11	-7.9841E-03	-2.9277E-03	1.6710E-02	-1.9771E-02	6.8189E-03	1.5458E-02
12	1.4976E-03	7.8528E-04	1.9983E-04	-1.0968E-02	5.0064E-03	1.5110E-03
Node	**Vertical Strain**	**Horizontal Strain**	**Shear Strain**	**Max Principal Strain**	**Min Principal Strain**	**Void Ratio**
1	-4.7915E-02	2.3952E-02	-5.0029E-06	-4.1029E-02	1.8904E-02	4.000
2	-7.0639E-02	3.5592E-02	2.2274E-05	-6.9400E-02	2.5224E-02	4.003
3	-3.2277E-02	1.6120E-02	8.6358E-04	-5.7353E-02	1.1046E-02	4.000
4	-4.2635E-02	1.9994E-02	1.8746E-02	-3.7862E-02	1.7060E-02	4.000
5	-7.6621E-02	3.9757E-02	2.7641E-02	-7.3856E-02	2.7285E-02	4.002
6	-3.8463E-02	2.0083E-02	-2.6600E-03	-6.9298E-02	6.6850E-03	3.995
7	-2.8797E-02	9.8514E-03	3.0015E-02	-2.9608E-02	1.2468E-02	4.000
8	-5.1471E-02	1.5958E-02	9.4314E-02	-6.6124E-02	2.6225E-02	3.997
9	-7.7648E-03	-1.8490E-01	4.1620E-01	-1.5989E-01	4.5715E-02	3.260
10	-2.0666E-02	4.1291E-03	3.1038E-02	-2.4731E-02	9.9337E-03	4.000
11	-2.0172E-02	-7.5395E-03	8.3492E-03	-4.7168E-02	1.9260E-02	4.005
12	1.1108E-03	-6.6881E-04	9.9844E-04	-2.5608E-02	1.4301E-02	4.053

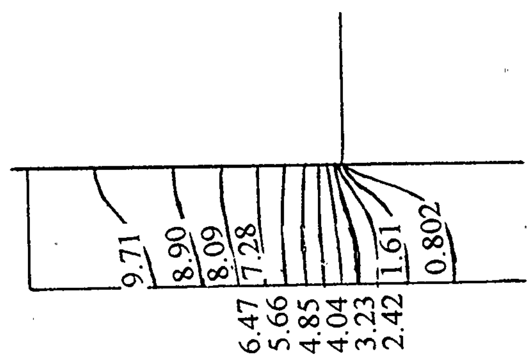

Figure C-1
h=0.75mm
r/h=2.67
x 100 MPa
Model A - Pore Pressures @ t = 20s

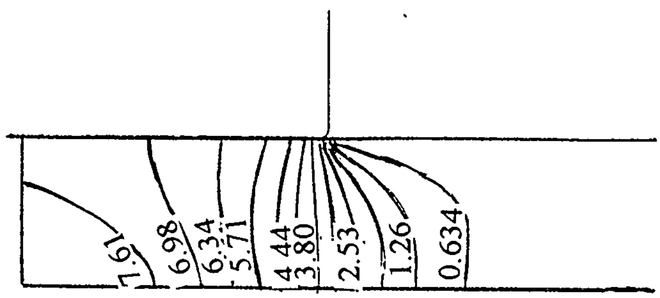

Figure C-2
h=1mm
r/h=2.00
x 100 MPa
Model B - Pore Pressures @ t = 20s

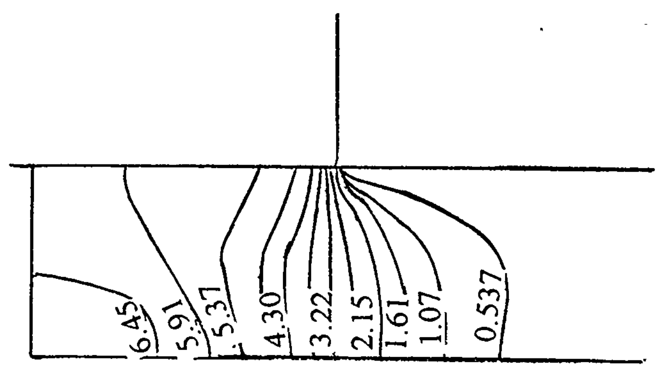

Figure C-3
h=1.25mm
r/h=1.60
x 100 MPa
Model C - Pore Pressures @ t = 20s

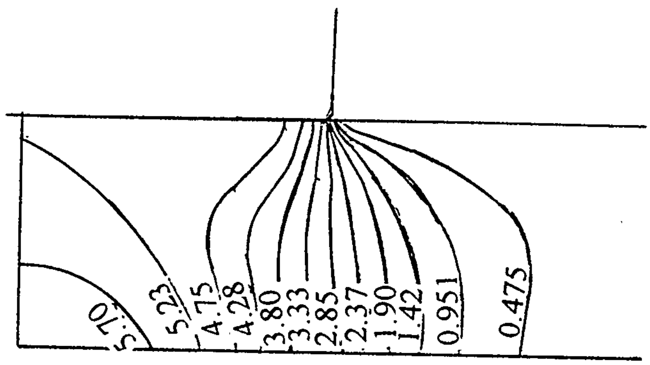

Figure C-4
h=1.50mm
r/h=1.33
x 100 MPa
Model D - Pore Pressures @ t = 20s

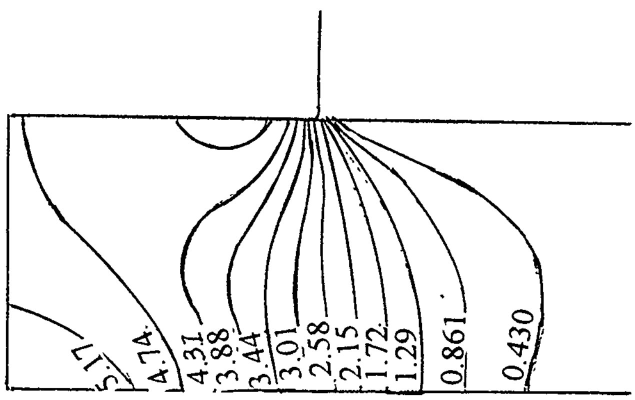

Figure C-5
h=1.75mm
r/h=1.14
x 100 Mpa
Model E - Pore Pressures @ t = 20s

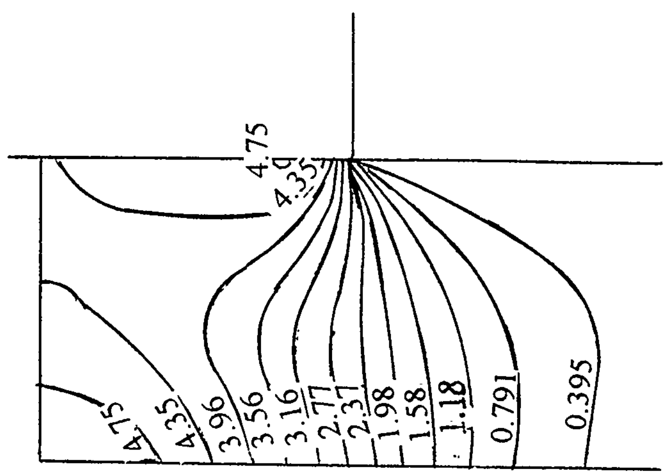

Figure C-6
h=2.00mm
r/h=1.00
x 100 MPa
Model F - Pore Pressures @ t = 20s

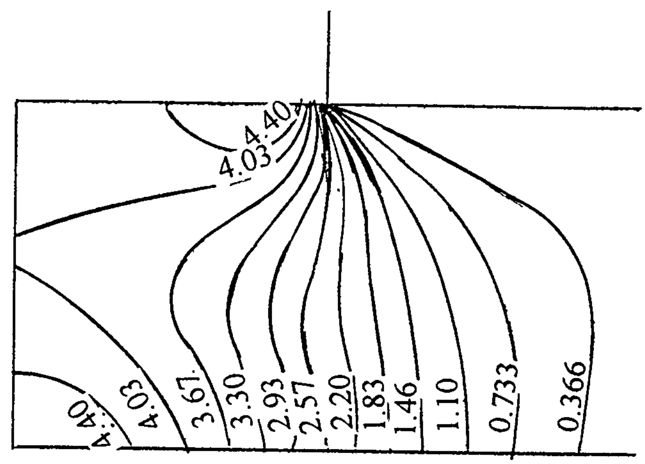

Figure C-7
h=2.25mm
r/h=0.89
x 100 MPa
Model G - Pore Pressures @ t = 20s

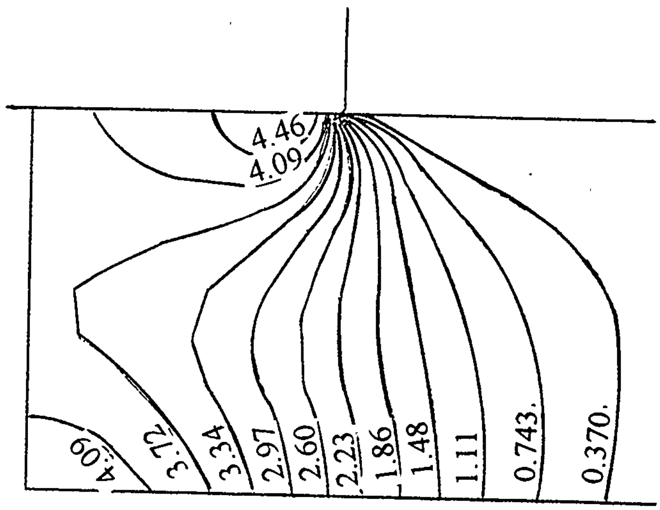

Figure C-8
h=2.50mm
r/h=0.80
x 100 MPa
Model H - Pore Pressures @ t = 20s

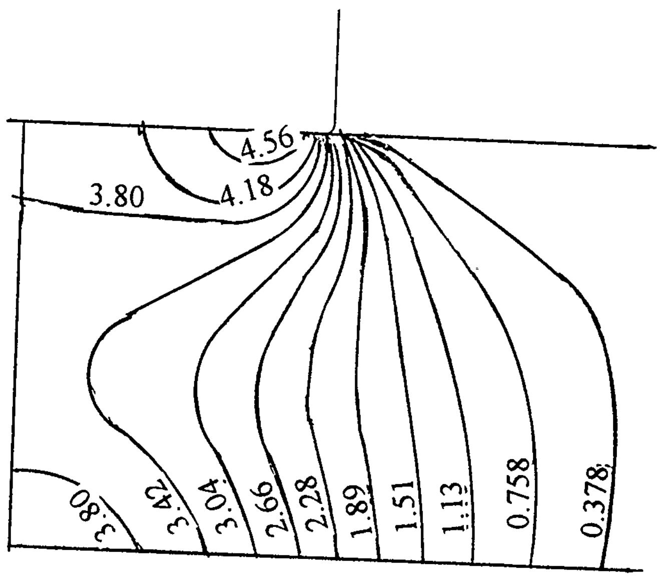

Figure C-9
h=2.75mm
r/h=0.73
x 100 MPa
Model I - Pore Pressures @ t = 20s

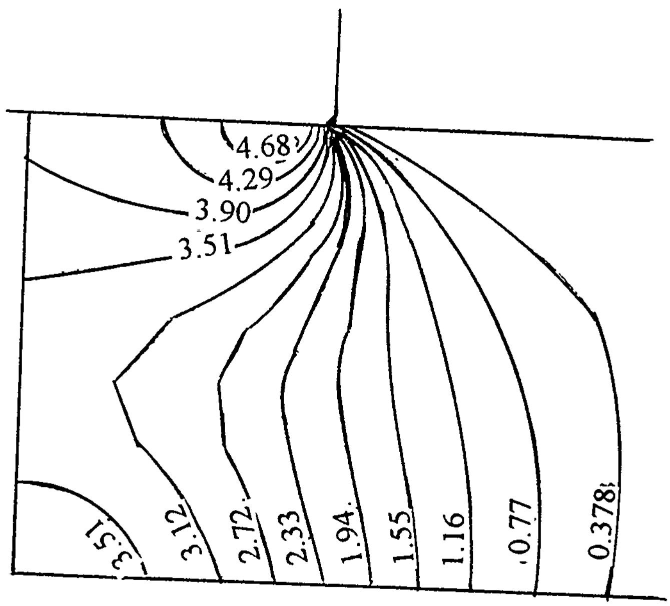

Figure C-10
h=3.00mm
r/h=0.67
x 100 MPa
Model J - Pore Pressures @ t = 20s

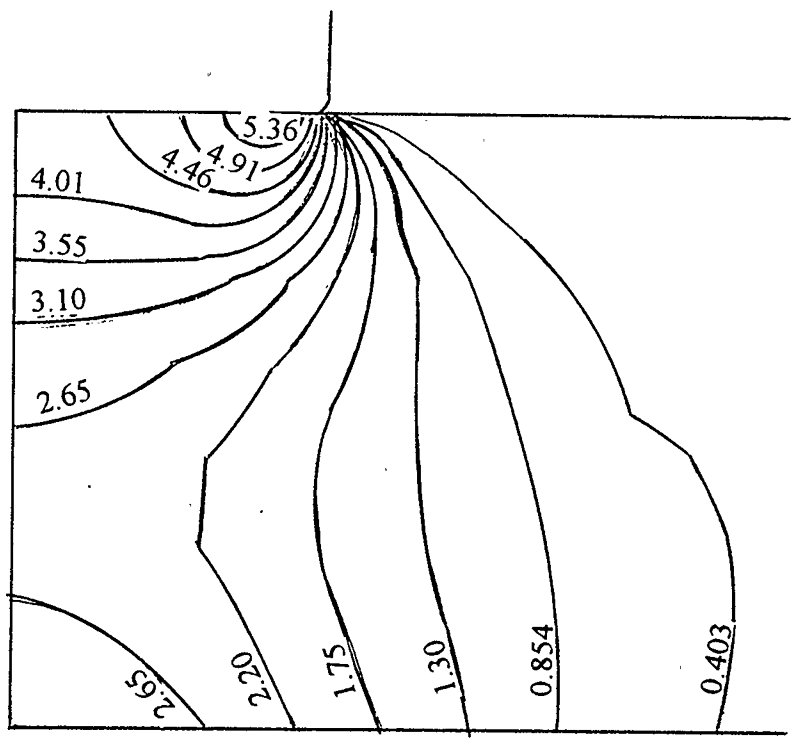

Figure C-11
h=4.00mm
r/h=0.50
x 100 MPa
Model K - Pore Pressures @ t = 20s

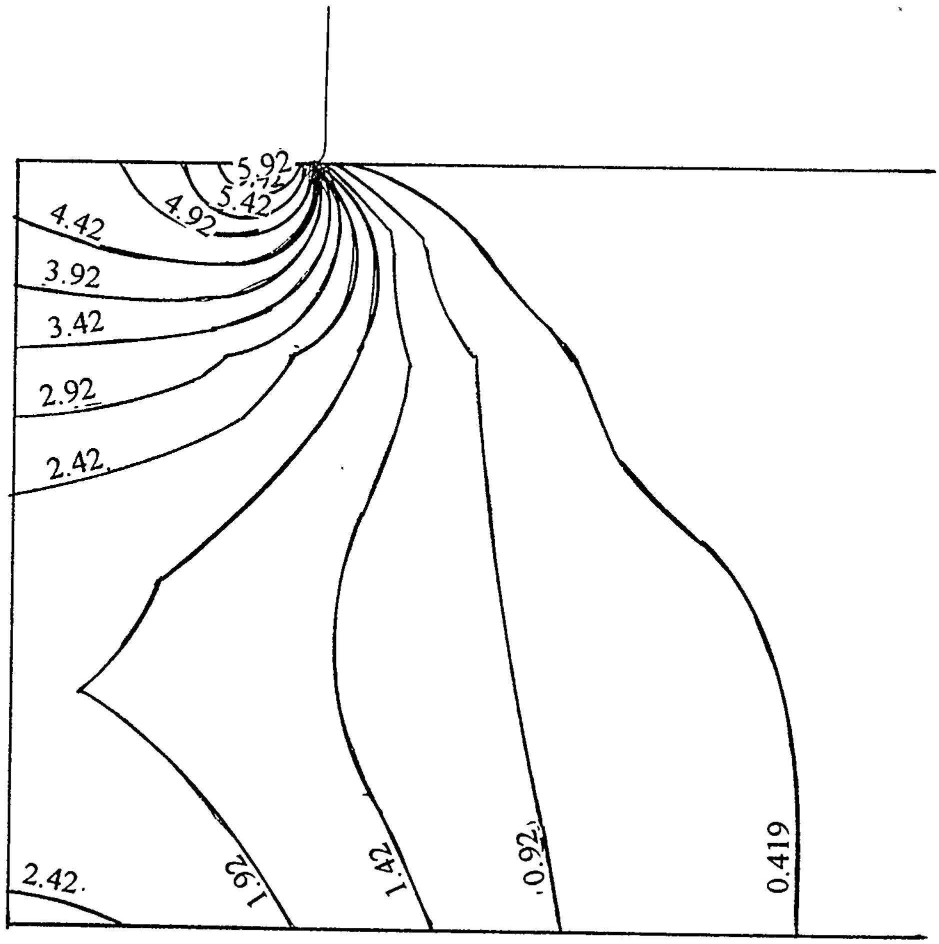

Figure C-12
h=5.00mm
r/h=0.40
x 100 MPa
Model L - Pore Pressures @ t = 20s

D.0 Appendix D

Effect of different loading rates on pore pressures.

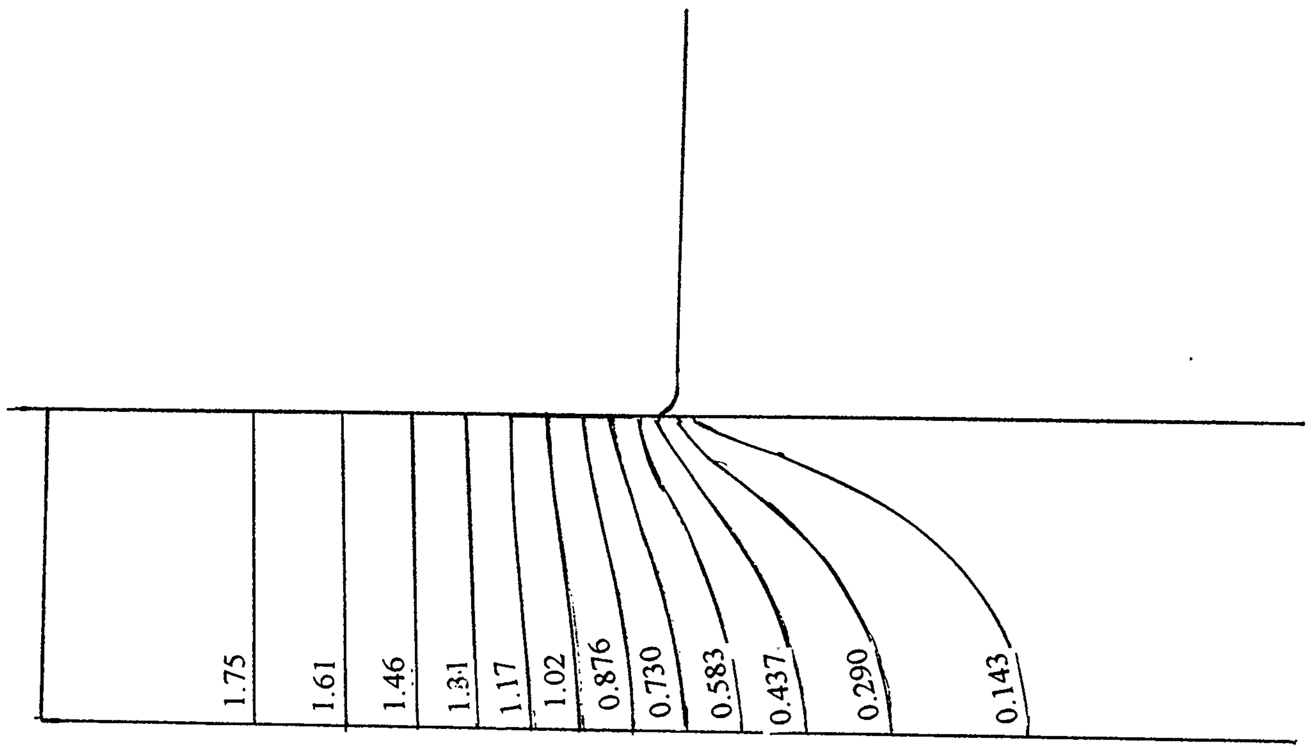

Figure D-1
t=500s
x 100 MPa
Model B - Pore Pressures @ t = 500s

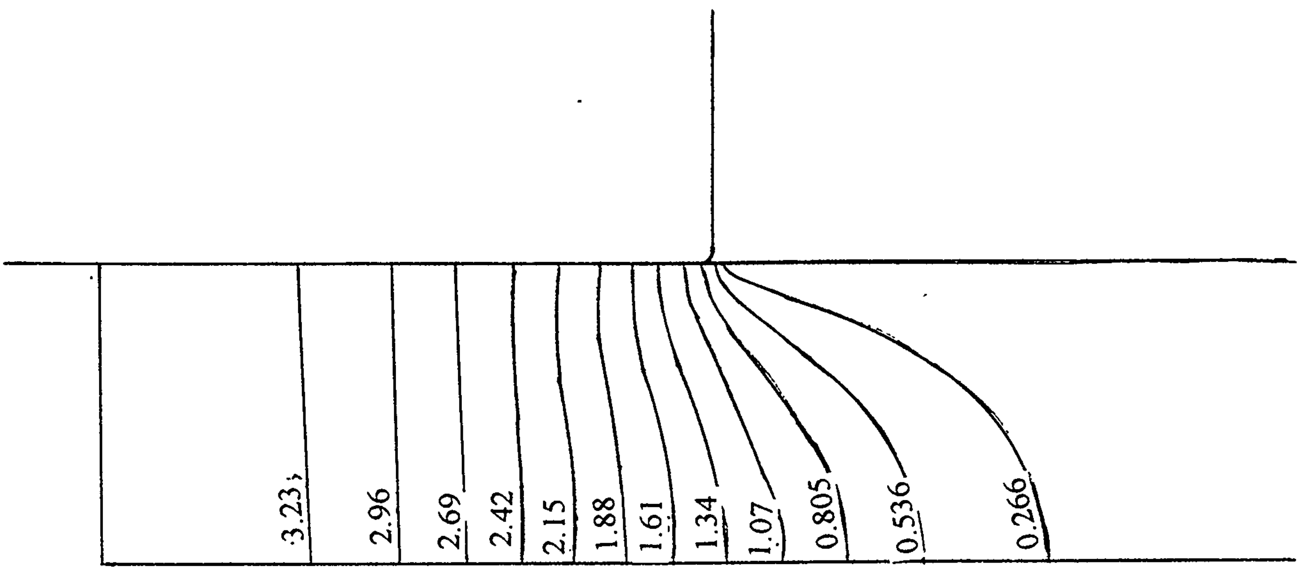

Figure D-2
t=250s
x 100 MPa
Model B - Pore Pressures @ t = 250s

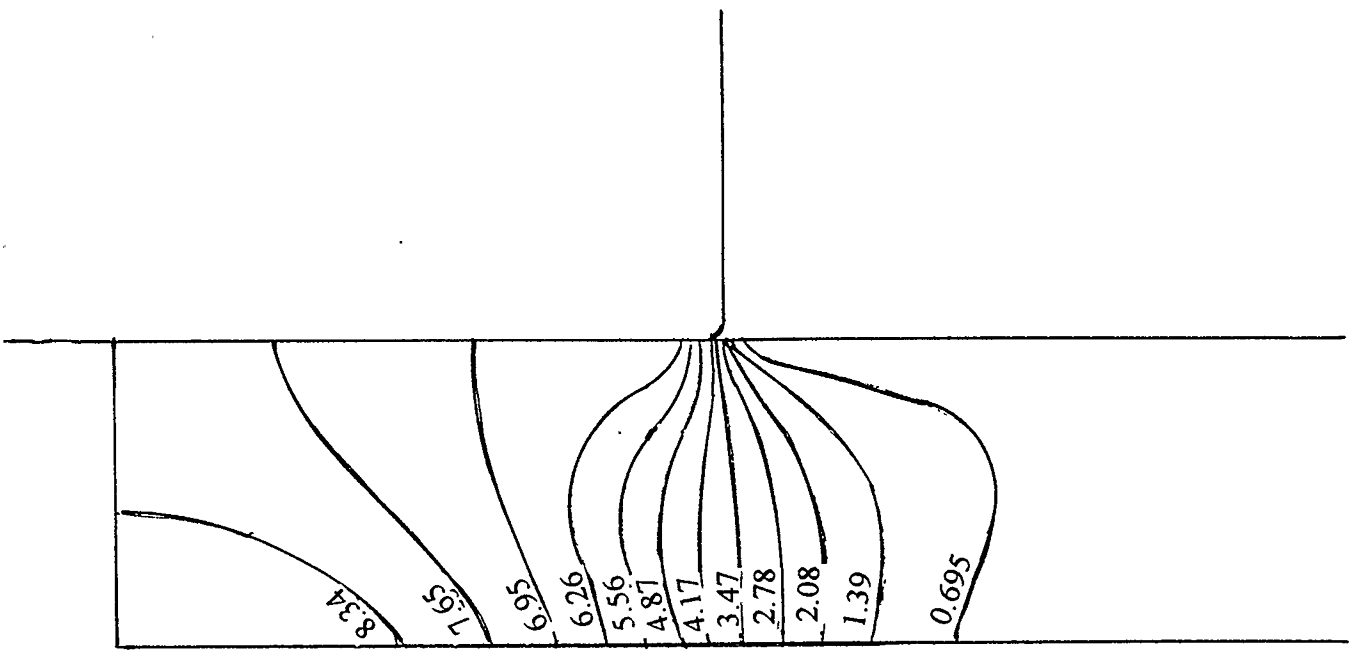

Figure D=3
t=5s
x 100 MPa
Model B - Pore Pressures @ t = 5s